UNIVERSITÀ DEGLI STUDI DI TRIESTE

XXIX CICLO DEL DOTTORATO DI RICERCA IN CHIMICA

HIERARCHICAL MATERIALS FOR ENERGY AND ENVIRONMENTAL APPLICATIONS

Settore scientifico-disciplinare: CHIM/06

COORDINATORE

CHIAR. MO PROF. MAURO STENER

DOTTORANDO

ALESSANDRO BELTRAM

SUPERVISORE DI TESI

CHIAR.MO PROF. MAURIZIO PRATO

CO- SUPERVISORI DI TESI

CHIAR.MO PROF. PAOLO FORNASIERO

DR. MICHELE MELCHIONNA

DR. TIZIANO MONTINI

ANNO ACCADEMICO 2015/2016

TABLE OF CONTENTS

ABSTRACT

The research activity of the present thesis has focused on the development of carbon/inorganic hierarchical nanostructured hybrids to be employed as catalysts for two important energy processes: the water-gas shift reaction (WGSR) and the photocatalytic hydrogen production from renewable sources, such as biomass-derived oxygenated compounds (i.e. ethanol and glycerol). The design of the nanohybrids follows a specific hierarchy where a carbon component, consisting of properly functionalized multiwalled carbon nanotubes (MWCNTs) or carbon nanocones (CNCs), is used as scaffold for an inorganic phase that acts as the catalyst/cocatalyst. The inorganic phase in turns consist of noble metal nanoparticles (i.e. palladium) enclosed into a mesoporous metal oxide. The functionalization of the carbon components serves to equip the nanocarbon with anchor points for the metal phase and to enhance dispersion in liquid media. The as-prepared ternary hybrid is then subjected to specific thermal treatments, with the temperature chosen on the basis of thermogravimetric analysis, in order to crystallize the metal oxide phase and remove the organic ligands. The final catalyst package has shown remarkable catalytic features in both the investigated processes, confirming that the presence of the nanocarbon scaffold and the specific hierarchy result in a large improvement of the performance as compared to state-of-the art catalysts. Such improvement is related to the excellent electronic properties of the carbon nanostructures as well as to their ability to enhance robustness and stability of the inorganic phase. More specifically, CeO_2-based catalysts display an increased activity and stability in the WGSR, while the TiO_2-based photocatalysts were successfully used in the photocatalytic production of H_2 with very high productivity. Characterization of the materials has been carried out through several techniques including HR-TEM, EDX mapping, XRD, microRaman, physi- and chemi-sorption analysis and TGA, which confirmed the obtainment of the desired assembly.

Chapter 1

INTRODUCTION

Energy is a central theme for the 21st century world population, affecting everyday's life in many different circumstances. We use energy virtually for every action, from lighting our houses to operating computer or functioning industries. Our bodies themselves use energy to carry out the biological processes necessary to life.

The common description of energy is "the ability of a system to perform a work" and much of the energy we use comes, directly or indirectly, from the nuclear processes occurring in the Sun.

Energy cannot be created, but it can only be transferred from one body to another and transformed from one form to another. This happens continuously: the natural photosynthesis transforms solar energy into chemical energy stored in glucose molecules, which is just the first of many energy carriers that drive the living beings. The common perception of energy in everyday's talk is associated with the electricity reaching our houses or the fuel moving our cars, rather than related to the food we eat. However, they are profoundly linked since the actual standards of life have been achieved through the use of Sun energy stored by photosynthetic processes in wood at first and fossil fuels (coal, natural gas and oil) later.

Nowadays the main primary energy sources are still fossil fuels, exploited worldwide to supply the 81% of the world energy demand (oil 31%, coal 29% e natural gas 21%, see **Figure 1.1 A**).[1] Their intensive use in the last hundred years brought up many issues, from geopolitical conflicts (due to their non-uniform distribution on Earth) to environmental consequences.[2] The exploitation of the energy contained in fossil fuels is not exactly a reverse photosynthesis process, because many additional polluting by-products are produced concomitantly to the fossil fuel combustion, such as SO_x, NO_x, volatile organic compounds (VOCs), CO, CH_4, heavy metals and atmospheric particulates. Furthermore, the enormous amount (gigatonnes per year) of CO_2 deriving from the use of fossil fuels that has been released in the last century (**Figure 1.1 B**) cannot

be reabsorbed through photosynthetic processes in a comparable timescale, thus breaking the bio-geological equilibrium that took millions of years to be established. Therefore, CO_2 has become one of the most adverse pollutants due to the concentration it reaches in the atmosphere, causing climatic changes and increasing acidity of seas and oceans. In 2015, for the first time since a time series exists, the level of CO_2 in atmosphere overcame 400 ppm,[3] exacerbating concerns.

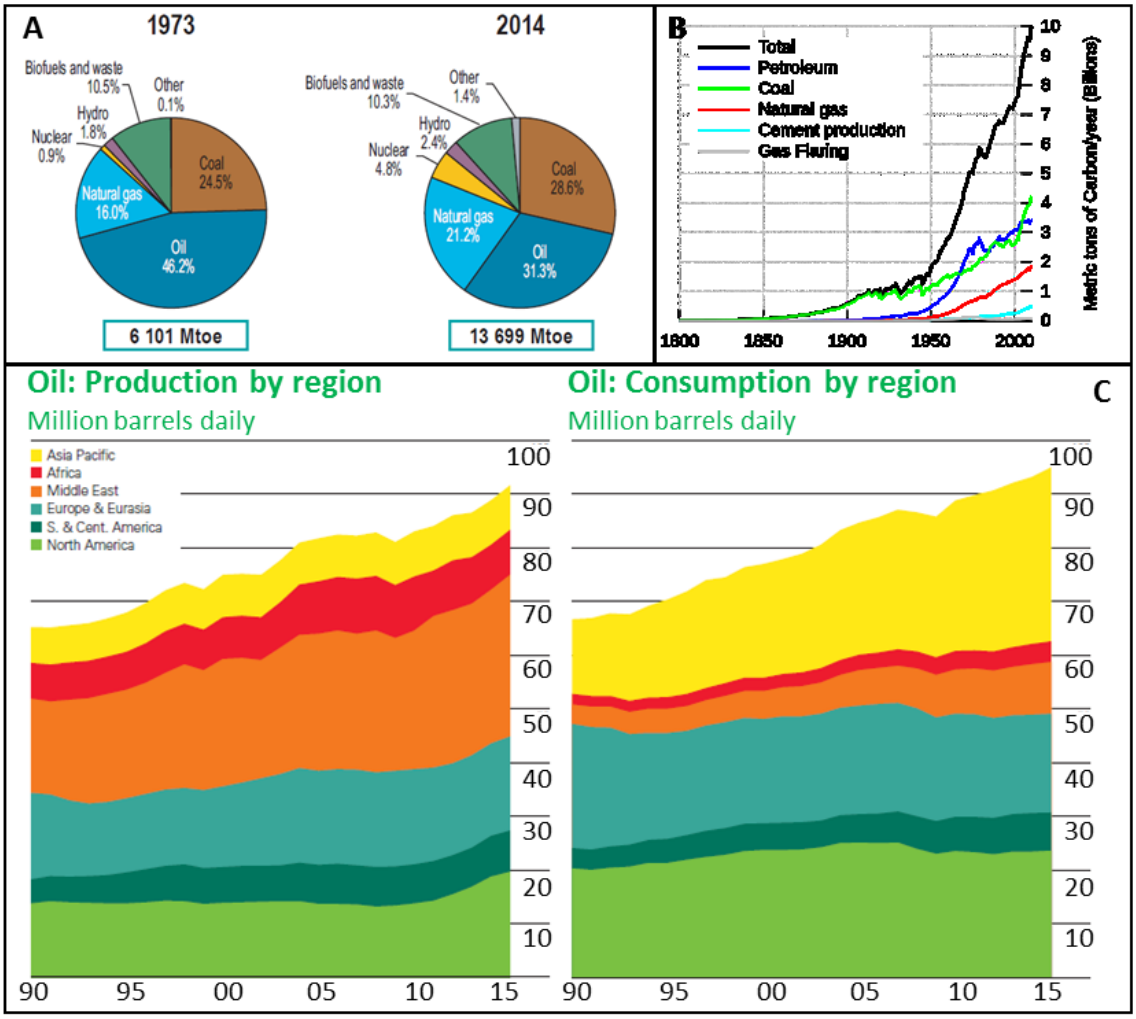

Figure 1.1: A) World's total energy supply by fuel;[1] B) Global fossil carbon emission by type of fuel and other sources; C) Annual oil production and consumption by region.[4]

Beside the major environmental issues, there is another aspect that deserves attention: fossil fuels are a non-renewable source since their formation takes millions of years while their consumption is much faster. Furthermore the increasing energy demand

by the growing population has outpaced fossil fuel extraction rates, causing major inconvenience in many countries[4] **(Figure 1.1 C**).

It is clear that, to overcome actual fossil fuels dependence, new energy schemes must be implemented. In this context, renewable sources, like photovoltaic, hydroelectric, wind, geothermal and biomasses, with no environmental impact, are emerging as a possible realistic alternative. Every day, new scientific discoveries are making the horizon brighter for a definite breakthrough of such renewable energy schemes. One of the main problems associated with these new technologies lies in the intermittence of most of these environmentally friendly energy sources. For this reason, a possible solution is that the excess energy available during the production peaks is stored in the form of chemical energy taking advantage of an appropriate energy carrier.[5] Among the options to achieve this purpose, electric batteries and the hydrogen molecule are most investigated and promising. Both options present advantages and disadvantages. At present, electric batteries cannot fulfill the accumulation of large amounts of electrical energy, as demanded by most of the devices. On the other hand, hydrogen Fuel Cells, whose energy efficiency are steadily growing,[6,7,8,9] are receiving more and more interest. Batteries can be used in small devices (e.g mobile applications) while the higher energy density per unit of volume and mass of pressurized hydrogen makes it more suitable for applications requiring higher amounts of energy (e.g. automotive industry).

1.1 HYDROGEN

Hydrogen is a key molecule for many industrial processes,[10] such as ammonia-fertilizer production (50% of the world production of hydrogen), oil refining (40%, hydrodesulphurization, hydrodenitrification and hydrocraking), methanol production (8%), hydrogenation reactions, etc.

Apart from these current extensive uses, hydrogen is today perceived as the energy carrier of the future, able to power our entire planet. The weight being equal, hydrogen contains a potential energy output almost three times higher than natural gas, and the only product of its combustion is water. It is therefore hard to imagine a cleaner energy source. However, projections underline that hydrogen-based energy economy able to replace fossil fuels will be feasible only in a medium to long term. This is due to several challenges that still need to be solved. One of the main difficulties regards the storage of

hydrogen in a safely way and the building of a production and distribution network.[11] Hydrogen is known to be flammable and explosive in a very wide range of concentrations in air (between 4% and 75% by volume)[12]; a notorious example is the destruction of Hindenburg airship, probably taking fire through spark ignition of hydrogen. A possible environmental concern regards the effect of H_2 leakages released in the atmosphere, because of its interaction with ozone.[13]

In order to be sustainable, the use of hydrogen as energy carrier needs to be associated to a clean production and a clean utilization. As regards the second aspect, besides industrial application as chemical reagent, there are two feasible ways to transform hydrogen into mechanical or electric energy (and then each one in the other one): burning it in internal combustion engines and producing electricity in Fuel Cells. Hydrogen is free of carbon, sulfur and metals (this means no smog, particulate, CO, SO_x, etc.) and gives H_2O as only product when burned, thus implying a zero toxic emission after direct combustion. However, it is noteworthy that nitrogen oxides (NO_x) can also form during high-temperature combustion in air. On the other hand, Fuel Cells have no contrasting effects with the environment, producing H_2O and electric energy from H_2 and air.

As far as hydrogen production is concerned, it must be first noted that hydrogen is the most abundant gas in the universe. However, its molecular form is very rare (0.5 ppm by volume)[14] in the Earth atmosphere. Some bacteria and algae naturally produce it but, because of its light weight, it easily escapes from Earth. Hence, there is a huge industrial business dedicated to the artificial production of H_2, estimated in $5 \cdot 10^{10}$ kg per year worldwide.[11] Its actual industrial production is based on conversion of fossil fuels (~ 95%) to syngas, a mixture of CO and H_2, mainly through methane steam reforming[15,16] that yields the higher H/C ratio (**Eq. 1.1**).

$$CH_4 + H_2O \rightarrow CO + 3\ H_2 \qquad \textbf{Eq. 1.1}$$

Among the employments of such produced H_2, most of the catalyzed reactions require the purification from CO since this can strongly adsorb on the metal catalyst causing its poisoning. The decrease of the CO percent can be obtained mainly by oxidation to CO_2, commonly through a reaction called Water Gas Shift Reaction (WGSR).[17] This process reduces the CO content (to 1-2 %) and at the same time increases the H_2 production. However, some applications require a very low percent of CO (e.g. CO content below 10

ppm for proton exchange membrane Fuel Cells),[18] therefore a second stage to further decrease the CO content is necessary. Such additional stage (**Figure 1.2**) may include: *i*) methanation,[19] the process which produces methane from CO and H_2, thus resulting in a loss of fuel efficiency; *ii*) selective H_2-diffusion through membranes,[20] which requires high-temperature and pressure gradients; *iii*) PReferential CO OXidation (PROX),[21] which consists in a selective oxidation of CO with oxygen.

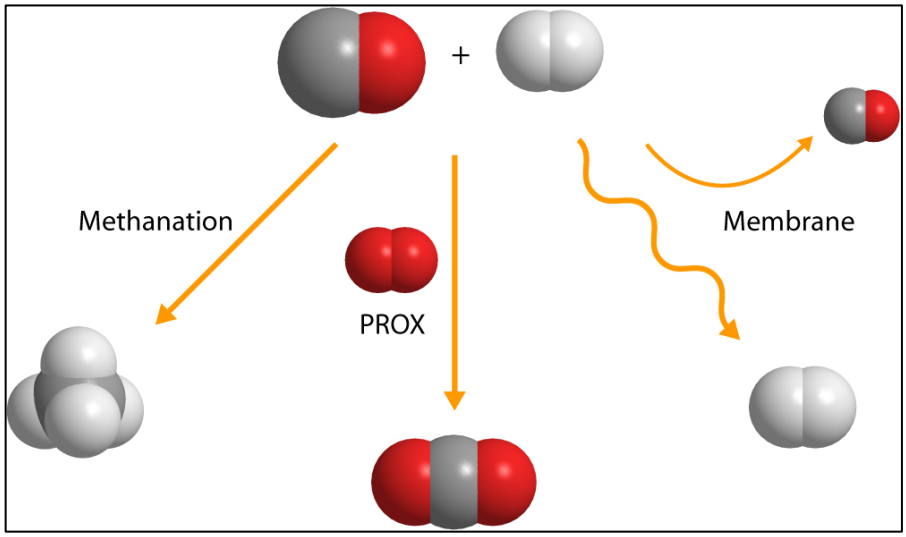

Figure 1.2: Schematic representation of the different methods for fine CO removal from H_2 streams after WGSR.

If production of hydrogen must depend on fossil fuels, the sustainability of a hydrogen economy would be severely compromised. Furthermore, these processes consume enormous amount of energy since require high temperatures, especially in the first stage of fuel reforming (700 – 1100 °C). Certainly, the transition from a fossil fuel-based economy to a renewable energy system, hopefully based on hydrogen acting as energy carrier, will be a progressive process that will require decades. A fundamental target to move the first step in this direction is to obtain the H_2 required by industries from renewable sources.

Many processes are nowadays available to produce H_2 in alternative to methane reforming, such as water splitting and reforming and partial oxidation of oxygenated compounds coming from biomasses. Among them, electrochemical water splitting, yielding H_2 and O_2 by applying electricity, is a particularly convenient avenue, and there is much focus on the development of cathodic materials for the hydrogen evolving reaction (HER).[22] It is nowadays employed to get the 5 % of H_2 not produced by

reforming of fossil fuels. The process has been improved working at high temperatures (High Temperature Electrolysis, HTE)[23] exploiting the IR component of the Sun light by solar concentrators.[24]

On the other hand, the processes involving reforming of oxygenates compounds (**Eq. 1.2**) should divert the employment of fossil fuel and require lower temperatures, which however causes formation of coke over the catalysts.

$$C_xH_yO_z + (2x - z)\ H_2O \rightarrow x\ CO_2 + (2x + y/2 - z)\ H_2 \qquad \textbf{Eq. 1.2}$$

Oxygenates compounds were also employed in electrochemical cells by replacing oxygen evolution with the oxidation of biomass-derived alcohols, leading to a more efficient process.[25]

An important aspect that needs to be considered is the origin of the biomasses. Many processes, such as sugar fermentation and transesterification of animal fats or vegetable oils, are used to obtain the so-called first generation biofuels. However, the massive exploitation of these sources can seriously compromise both food supplies and biodiversity. A key point is the employing of raw materials coming from residual non edible parts of the current human food chain or from industries wastes, such as glycerol coming from biodiesel production and sugars (then converted to ethanol by fermentation) obtained from complex molecules (e.g. steam explosion of lignin, hemicellulose or cellulose) coming from woods or fibrous non edible biomasses.[26,27,28] In a short to medium term, these products mainly deriving from agricultural residues could replace part of the fossil fuel in the thermal reforming processes to obtain H_2 or directly furnish a fuel such as bioethanol.

The artificial energy input required to produce H_2 from these feedstocks can be virtually cancelled out by employing photo-assisted processes: a suitable photocatalyst can channel the solar energy into the evolution of H_2 molecules. Again, the use of H_2O as hydrogen containing substrate is the ideal pathway due to sustainability issues, and it was demonstrated to be viable by Fujishima and Honda in the 1972,[29] by irradiating a TiO_2 electrode in a so-called photoelectrochemical cell (PEC). Even though this system was still ineffective from a solar-to-fuel efficiency point of view, great improvements have been done in this field.[30] A milestone example was given by Nocera,[31] which

developed an efficient PEC in both wired and wireless (the so-called artificial leaf) configurations (**Figure 1.3**).

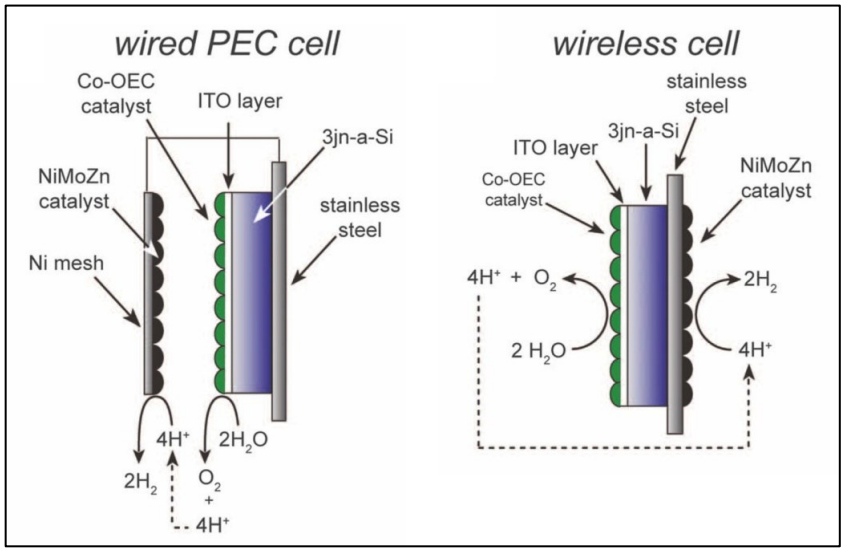

Figure 1.3: Schematic representation of the PEC developed by Nocera[31] in both wire (on the left) and wireless (on the right) configurations.

Concomitantly, the very relevant H_2 production from sunlight has sparked the interest of many research groups, who investigated the possibility of using new heterogeneous materials to drive the direct water photosplitting with no use of applied electric potential.[32]

The low efficiency of the pure water splitting mainly arises from the recombination of the products (i.e. H_2 and O_2), from the difficult to oxidize H_2O to O_2 (i.e. more energetically demanding 4 electrons process), and from other factors intrinsically related to photocatalysts themselves (see next paragraph). Great efforts have been done to overcome these issues.[32]

Among the various strategies, great attention has been paid to H_2 production via the photoreforming of raw materials (i.e. ethanol and glycerol) coming from second generation biomasses. Such process shall furnish H_2 from residual/waste biomasses employing as energy source the abundant and free Sun light.

1.2 PHOTOREFORMING

In the photoreforming of oxygenated compounds (such as alcohols), the efficiency of the process is strongly enhanced respect to the pure water splitting since the oxygenated compound acts as a sacrificial agent undergoing a faster oxidation as compared to H_2O (being the oxidation of water extremely challenging from a thermodynamic perspective), leading to slower recombination phenomena between the photogenerated holes and electrons (see next paragraph for an exhaustive explanation).

From the literature, it becomes clear the intensive employment of methanol, since it was first reported,[33] as sacrificial agent despite its environmentally unfriendliness. The reason for its use is related to the simple structure of this alcohol because of the absence of C-C bounds, generally resulting in high activities. Nevertheless, in view of a sustainable production of H_2, great attention has been paid to photoreforming processes involving alcohols produced from biomasses, considering that methanol production is mainly based on fossil fuels. Kondarides et *al.* performed various studies, mainly using Pt-TiO_2 materials, on hydrogen production via photoreforming of different biomass-derived sacrificial agents (e.g. carboxylic acids, aldehydes, and alcohols). Among the various alcohols (obtainable from fermentation of various biomass-derived feedstocks), ethanol was one of the easiest to be fully converted into CO_2 because of its simpler structure, leading to the limited formation of intermediate C-containing products.[34] Another interesting option relies on the use of glycerol whose overproduction, mainly from biodiesel production,[35] has a negative environmental fallout since the processes consuming glycerol[36,37] are largely outpaced by the enormous amount produced (around 100 kg per ton of biodiesel). Several studies[38,39,40] well describe the H_2 production from photoreforming of aqueous solution containing glycerol (and other biomass-derived compounds) using Pt-TiO_2 as catalyst.

An additional advantage of the H_2 production through photoreforming relates to the fact that these processes normally occur at room temperature and atmospheric pressure. Therefore, the sintering phenomena, which can lead to deactivation of heterogeneous catalysts, are negligible. When higher alcohols are considered as sacrificial donors, the H_2 production can be also associated to the production of high value products (e.g. acetaldehyde or 1,3-diidrossiacetone) coming from selective alcohol oxidation reactions.[41]

1.2.1 Photocatalyst

Generally, the photoassisted reaction is driven by a semiconducting material (photocatalyst) with a suitable band gap E_g which, upon irradiation with a wavelength having energy equal or higher than E_g, promotes an electron (e^-) from the valence band (VB) to the conduction band (CB), leaving a hole (h^+) in the VB. Photogenerated electrons and holes are respectively responsible for reduction and oxidation semireactions. In the specific case of alcohol photoreforming, the formation of hydrogen occurs via reduction of protons by the photogenerated electrons. A deactivation mechanism of the photocatalyst involves the recombination of the e^- and h^+ (both in the bulk of the material or at its surface), thus making ineffective the desired overall redox process (**Figure 1.4**).

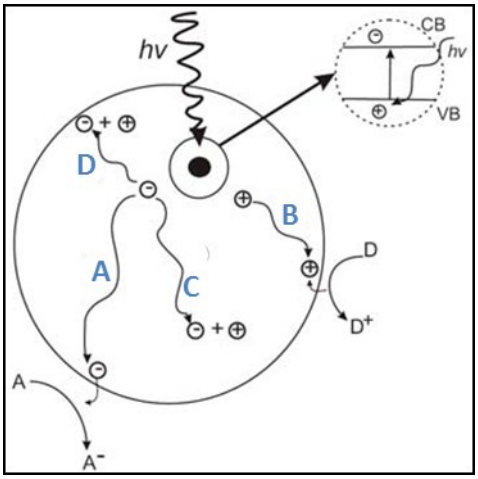

Figure 1.4: Photogenerated electrons and hole possible pathways: A) reduction; B) oxidation; C) bulk recombination; D) surface recombination.

The energy of the charge carriers is related to the electronic structure of the semiconducting material that determines the position of the conduction and valence bands. It turns out that not all the photocatalysts are suitable for a desirable reaction (i.e. proton reduction to hydrogen). **Figure 1.5** shows the redox semireactions that take place over the photocatalyst surface. Higher (i.e. less negative) standard reduction potentials (E° in V) correspond to lower energies (E in eV) following **Eq. 1.3**:

$$\Delta E = - nFE° \qquad \textbf{Eq. 1.3}$$

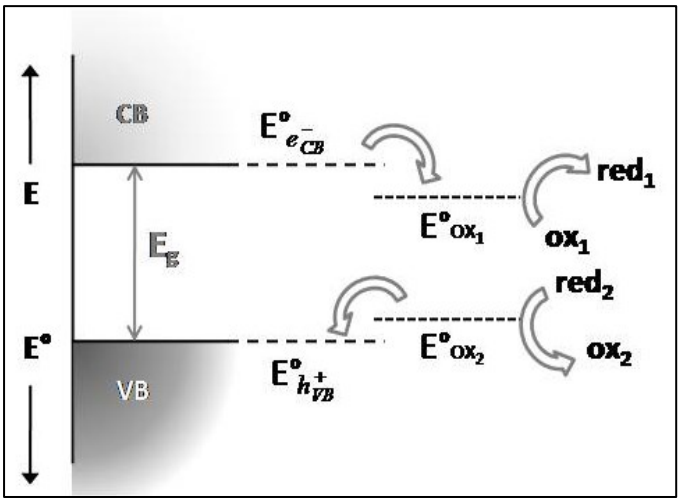

Figure 1.5: Redox reactions over photocatalyst surface.

The ability of the photogenerated electrons to carry out a reduction process depends on the lower limit of the CB; they are able to reduce redox pairs having a higher (more positive) standard reduction potentials, which for the H^+/H_2 couple is arbitrarily set at 0 V vs V_{RHE} . Analogously, the holes are able to oxidize redox pairs having a standard reduction potentials correlated to a lower energy (for example for the couple O_2/H_2O the associated potential is 1.23 V while for the couple H_2O_2/H_2O is 1.78 V, making the latter more difficult). Indeed, a photocatalytic process can be described in terms of a redox catalytic process that take place at the interface between a solid and a liquid and differ from classical heterogeneous catalysis by the activation mechanism of the catalyst, which is driven by photons rather than temperature, and for the extended processes of deactivation, which comprise also the annihilation of the photogenerated species.

Other important aspects that influence the performance of a photocatalyst are the crystallinity of the material and its surface area, respectively related to the structural defects, that can act as recombination centers for photogenerated electrons and holes decreasing the activity, and to the surface catalytic centers, where the redox reaction takes place. Thermal treatments affect both properties causing an enhancement of the crystallinity, which reduces the number of defects, and at the same time the sintering of the crystallites.[32] The latter is responsible for the reduction of the surface area of the material by either increasing the dimension of the crystallites (lower surface/volume ratio) than collapsing of the pores.

1.2.2 Titanium dioxide

The typical benchmark semiconducting material employed as photocatalyst for H_2 production is titanium dioxide (TiO_2), which is normally combined with other components to yield nanocomposite catalysts. In comparison with other semiconducting materials, TiO_2 presents a suitable bands position for the photoreforming of alcohols (**Figure 1.6**). Moreover, TiO_2 is widely available, cheap and chemically and physically stable.

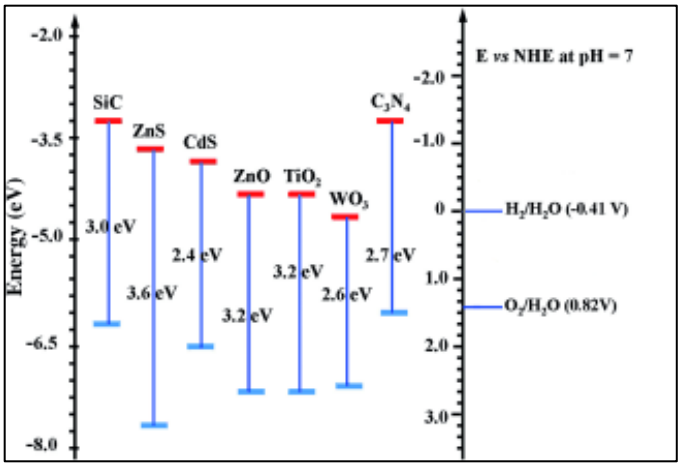

Figure 1.6: Band gap and bands energies of common semiconducting materials.

The main issue that this photocatalyst present is its wide band gap (~ 3.2 eV). To promote photogenerated charge carriers TiO_2 need to absorb UV wavelength. Since the UV component in Sun light result about 4 %, the bare TiO_2 present a weak activity if not opportunely modified.

The principal method to enhance the activity of photocatalysts is to couple it with metallic nanoparticles. In this way, a Schottky barrier is created at the interphase between the metal and the semiconductor allowing to the photogenerated electrons to be physically transferred and trapped in the metal nanoparticles because of the lower energy of their Fermi level (**Figure 1.7**).

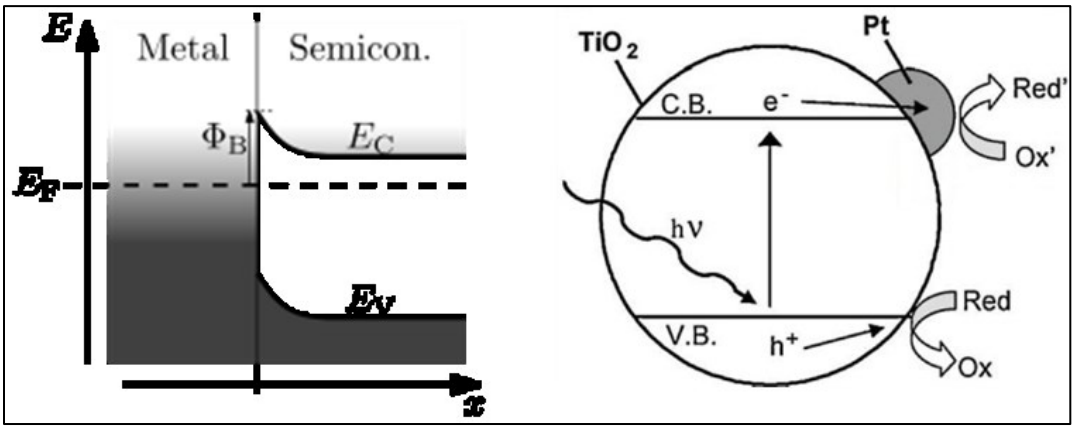

Figure 1.7: Schematic representation of the Schottky barrier at the meta/semiconductor interphase (on the left) and electrons and holes pathway in a metal/semiconductor system under irradiation (on the right).

Other different ways to improve the photocatalytic performance of TiO_2 can be found in the literature including doping with non-metal atoms such as nitrogen,[42] which is able to induce localized N 2p states within the band gap just above the valence band (VB) thus promoting absorbance in the visible light.[43] However, it has been demonstrated that the defects in the lattice structure created by N atoms can be detrimental as they act as charge recombination centers. Other non-metallic doping atoms, used to a less extent than N, include C, S, F, and B, which are also able to introduce intra band levels.[44] For example, Lambert et *al*.[45] studied the effect of B-doping and B,N-co-doping of TiO_2, finding a considerable red-shifting of the optical absorption associated to a significant photocatalytic activity in the visible light regime. A careful analysis of the nature of the doping must be done, such as whether the doping atom is a substitutional atom or an interstitial atom. This is important as the resulting band gaps can vary, with VB maximum lying above or below the original TiO_2 (VB), thus affecting the oxidation potential of the holes. Similarly, the doping can lead to formation of partially filled Ti^{3+} 3d states lying just below the conduction band (CB). The result is a variation of the reduction or oxidation potentials of the photogenerated charge carriers, which can have consequences on the effectiveness for the specific photocatalytic application (oxidative degradation reactions or H^+ reduction).[46]

The other most popular method relies on the deposition onto the TiO_2 surface of noble metal (Au, Pt, Pd, Ag) and base metal (Ni, Cu) nanoparticles, that are able to capture photoexcited electrons and retard the electron/holes recombination.[47,48,49] There have

been numerous reports on successful photoreforming of oxygenated compounds by TiO_2 loaded with metal nanoparticles.[50,51] Combination of non-metal doping and metal loading on TiO_2 has also been successfully achieved for catalyzing the photoreforming of alcohols. For example, several binary nitrogen/transition metal photocatalysts (M/N-TiO_2, M = Cr, Co, Ni, Cu) were successfully employed in the photoreforming of glycerol,[52] while gold-embedded boron-doped TiO_2 (Au/B-TiO_2) was investigated as hydrogen evolution photocatalyst from water/methanol mixtures.[53] However, the metal loading also requires adequate balance, as metal nanoparticles can also serve as recombination centers.

Finally, a reported strategy is to self-dope the TiO_2 with Ti^{3+} atoms after an appropriate reduction treatment. In particular, reduction with $NaBH_4$ and ensuing incorporation of Ti^{3+} atoms caused an enhancement of photocatalytic activity under visible light, while UV-light photoactivity remained substantially unaltered.[54] Similarly, hydrogenation of TiO_2 has led to the discovery of what was named "black titania", [55] whose enhanced solar absorption and photocatalytic activity could naturally be put in relation to formation of Ti^{3+} states.[56] However, some of the characteristic aspects of this material still remain obscure, and a recent report has shown that Ti^{3+} may actually be not responsible for the long wavelength absorption.[57]

Recently, many advances in the photocatalysis by TiO_2-based catalysts were reported by combination of TiO_2 with carbon nanotubes (CNTs) to form nanocarbon-inorganic hybrids with improved performances.[58]

1.3 WATER GAS SHIFT REACTION

Since H_2 is mainly produced as a mixture with CO (syngas), the equilibrium-controlled Water Gas Shift Reaction (WGSR) is a key step to produce extra H_2 (**Eq. 1.4**) and at the same time reduce the content of CO, thus fulfilling requirements of specific applications involving use of H_2.

$$CO + H_2O \rightleftharpoons CO_2 + H_2 \qquad \textbf{Eq. 1.4}$$

Considering that WGSR is moderately exothermic ($\Delta H°_{298\ K}$ = - 41.4 kJ mol^{-1}), the proper conditions to shift the equilibrium to increase concentration of H_2 are at low working temperatures (**Figure 1.8**). Nevertheless, the reaction is kinetically favored at

high temperatures. Therefore, the reaction is usually carried out in two steps, to take advantage of both thermodynamic and kinetic aspects.[59]

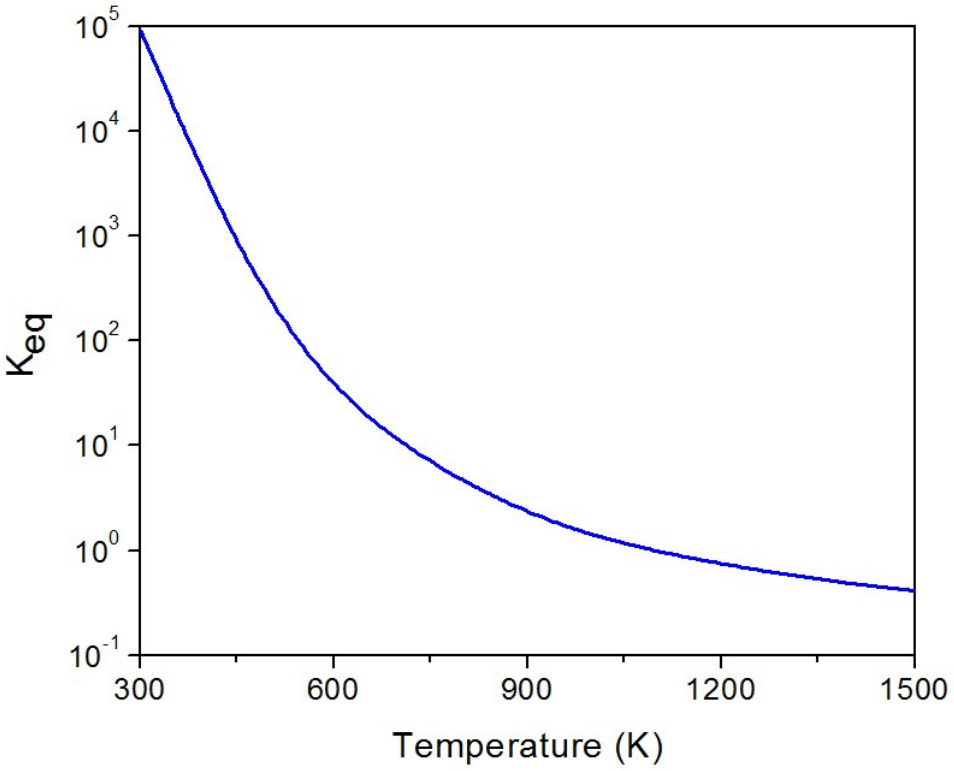

Figure 1.8: A plot of the temperature dependence of K_{eq} in the WGSR.

The first step at high temperature in the range 320 – 450 °C, named High Temperature Shift (HTS), takes advantage of the high kinetic rate but results in a CO final concentration of about 2 – 4 %, since it is limited by thermodynamic. Subsequently, a second step at low temperature in the range 200 – 250 °C, named Low Temperature Shift (LTS), removes CO under more thermodynamically favourable conditions, leading to a final CO content lower than 1 %. Different catalysts are employed at each step in order to maximize the activities. In the HTS stage, the commercial catalyst is composed by α-Fe_2O_3 (hematite) and Cr_2O_3 acting as stabiliser, retarding the sintering process of the iron oxide. Under reaction conditions the hematite is reduced at magnetite (Fe_3O_4), which is believed to be the active phase.[60] However, the loss in surface area of the active phase and environmental and safety problems regarding chromium emissions have sparked the development of new catalytic materials, that can be easily handled and discarded. On the other hand, in the LTS stage the commercial catalyst is a mixture of CuO and ZnO supported over Al_2O_3, where CuO is the active phase while ZnO provides structural

support and prevents the poisoning of copper by sulfur residues coming from the syngas production (i.e. reforming processes).[61]

When designing a catalytic system, particular attention must be also given to the support employed. Transition metals supported over CeO_2 are extensively studied for the WGSR due to their improved catalytic activities as compared to catalytic systems with other supports.[62,63] There is a distinct promotional effect caused by the ceria,[64,65,66] which is mainly related to its exceptional redox properties and the ability to act as oxygen buffer.[67] As far as the catalytically active metals are concerned, the most investigated metals are Pt, Cu and, in the last years, Au. Pd is less studied because of its low thermal stability.[66] The fast deactivation that all these catalysts show under working conditions is one of their main drawbacks.[68] Efforts are therefore being made to improve both activity and stability, both at low and high temperature operating conditions.

1.4 NANOSTRUCTURED HIERARCHICAL CATALYSTS

Nanotechnology can be defined as the ability to work at the atomic, molecular and supramolecular levels (on a scale of ~1-100 nm) in order to understand, create and use material structures, devices and systems with fundamentally new properties and functions resulting from their small structure. When materials are at the nanoscale (~1-100 nm) acquire peculiar physical and chemical properties, different from the related bulk materials. A decrease in the dimension implies a higher percent of superficial atoms with unsaturated valences,[69] which have different properties with respect to the bulk atoms.

The interest in nanoparticles (NPs) arises from the fact that when a metal particle with bulk properties is reduced to a size of a few dozens or few hundred atoms, the density of states in both the VB and in the CB decreases, changing the electronic properties of the material (e.g. band gap). The quasi-continuous density of states is replaced by discrete energy levels with a size-dependent spacing (quantum-size effect). The possibility of tuning particle sizes and their relative properties becomes of primary importance in the field of heterogeneous catalysis. On the other hand, the reduction of dimensions of the particles itself gives a beneficial effect to the catalyst by enhancing the active surface area exposed. The surface atoms of a metal nanoparticle are not fully coordinated and they possess free sites in which molecules can adsorb and react.

The properties of different materials can be combined in hybrids or composites. One of the simplest cases is the deposition of metal nanoparticles over an inert material presenting a high surface area (e.g. amorphous carbon or a metal oxide such as Al_2O_3 or SiO_2), an expedient well-known in the heterogeneous catalysis, with the purpose of maximize the surface of contact between the metal and the substrate and stabilize the active phase. The naturally second step is to interface materials interacting electronically, where the support also has an active role in the catalytic process. This is the case of metal nanoparticles deposited over semiconductor metal oxides which act as the true photocatalyst (whereas the metal nanoparticles are considered as co-catalysts). In this case, the properties of the two components are synergistically combined with the purpose of enhancing the catalytic properties of the hybrid. The catalytic properties of the hybrid material are not merely associated with the sum of the individual components' properties, but there may be additional catalytic features, as long as the interfacing has been correctly performed. Carbon/inorganic hybrids are deeply studied in the field of heterogeneous catalysis and many recent studies[58,70,71] corroborate the idea that carbon nanostructures, in particular due to their electronic properties, act as active support in several catalytic processes. In the case of photoreforming processes, several hypotheses have been advanced to explain the promoting role of the carbon nanotubes (CNTs), of which the most accredited involve: 1) an electron sink effect of the carbon scaffold (which retard recombination of the photogenerated charge carriers;[72,73] 2) a photosensitizing effect, with the CNTs undergoing the light-induced charge separation and then inject the photoexcited electrons into the TiO_2 CB;[74,75] 3) formation of intermediate states following Ti-O-C bonds resembling carbon-doping of TiO_2.[76,77]

Moreover, many other nanocarbon scaffold, such as graphene, carbon nanohorns and carbon quantum dots, presented intriguing interactions with inorganic components in the field of heterogeneous catalysis.[70] Among them, carbon nanocones have not been explored as catalyst supports in heterogeneous catalysis, despite their intriguing structural properties. Nevertheless few theoretical studies[78,79] modelled their physical properties, predicting their great potential for exploitation in several applicative fields.

1.4.1 Carbon nanotubes

CNTs have emerged as intriguing active supports in a range of catalytic applications due to their fascinating mechanical, electronic, optical and thermal properties. In 1976 for the first time Oberlin et *al.*[80] reported the existence of CNTs. Then in 1991 with Iijima's report[81] we assisted to a great deal of interest in the use of CNTs for nanotechnological applications. Basically, this material is a form (allotrope) of carbon like graphite, diamond and fullerenes, but with unique physicochemical properties due to their electronic structure. We can image CNTs like a single layer of graphene rolled on itself. In particular it is usual to divide carbon nanotubes into two categories, single walled nanotubes (SWNTs) that are composed by a single rolled layer of graphene and multi walled nanotubes (MWCNTs) formed by several coaxial single walled nanotubes (**Figure 1.9**).

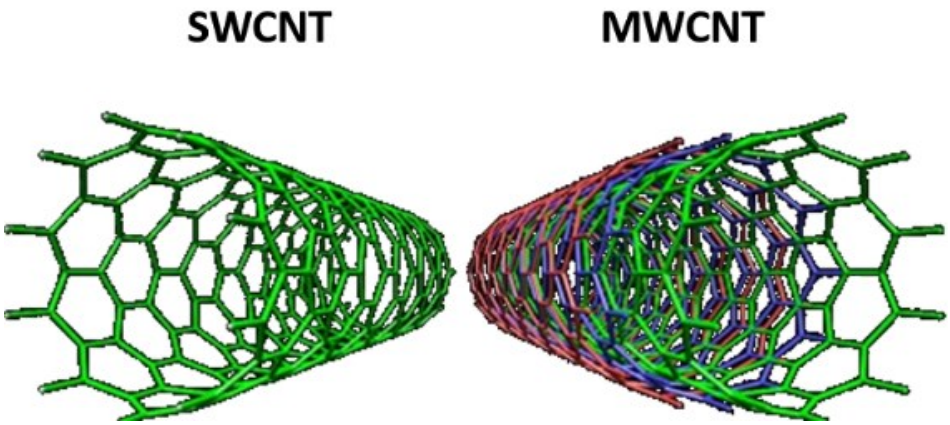

Figure 1.9: SWCNT and MWCNT schematic representation.

MWCNTs structure can be defined by its circumferential periodicity ($\vec{C}$), as described using the chiral vector $\vec{a}$ (**Figure 1.10**), which connects two crystallographically equivalent sites on a graphene sheet. In this way, the CNTs geometry is specified by the pair of integers (n, m), denoting the relative position of the pair of atoms on a graphene strip, which, when rolled onto each other, form a tube.

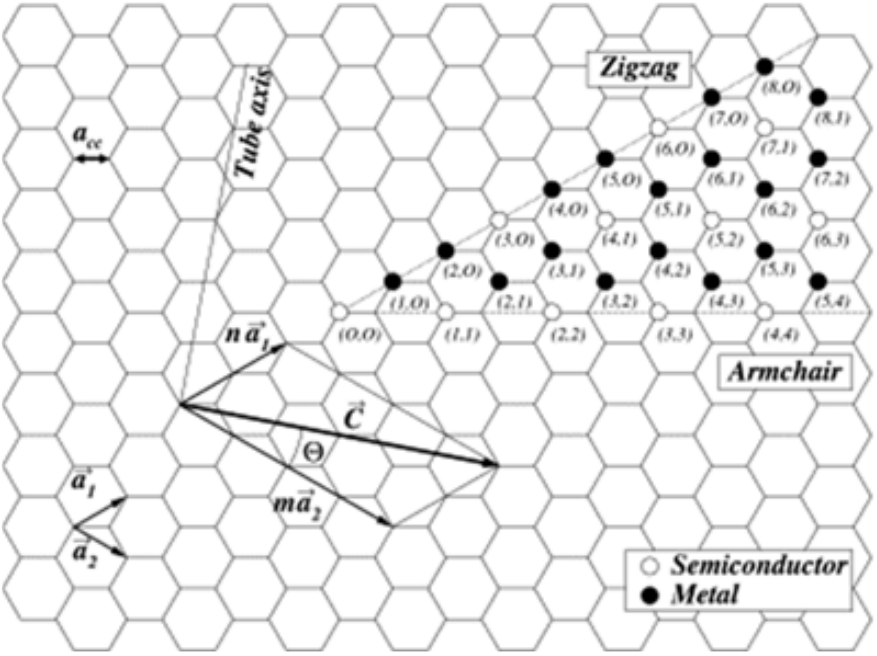

Figure 1.10: Schematic diagram showing the possible wrapping of the two-dimensional graphene sheet into tubular form.

Theoretical calculations demonstrated that the geometry of carbon nanotubes could influence and change the electronic properties of the nanomaterial.[82,83]

Although graphene is a zero-gap semiconductor, theoretical calculations predicted that carbon nanotubes can be metals or semiconductors, with different sizes energy gaps, depending very sensitively on the diameter and helicity of the tubes.[84]

Three types of structures are found: armchair, chiral, and zig-zag (**Figure 1.10**), which exhibit different electronic properties as a consequence of the different band gaps given by different wrapping of the graphene sheet. Hence, armchair tubes are always metallic, whereas zig-zag and chiral tubes can be either metallic or semiconductors.

In the case of MWCNTs, they always turn out to be metallic.

1.4.2 Carbon nanocones

Carbon nanocones (CNCs) represent a very peculiar class of carbon nanostructures; they have been known since almost two decades.[85] Most of the studies involving CNCs regards their structural[86] and electronic properties.[79] In particular, it was highlighted that their cone-like morphology results in very interesting features, such as an uncommon graphene sheet stacking depending on the apex (cone) angle.[87] An

interesting example of their employment in an applicative field regards the hydrogen storage properties of Ti-CNCs hybrids.[88]CNCs are a mixture of structures with different apex angle which cause variation of morphology ranging from disks to cones. Electron diffraction measurements reveal that the structures consist of a graphitic core surrounded by amorphous carbon (approximately 10 – 30 %) which is supposed to crystallize when the material is heat-treated (2700 ◦C).[86]

Up to the present investigation, no studies have been reported on the utilization of CNCs as support for metal catalysts, making this field worth exploring.

1.5 AIM OF THE THESIS

The main aim of this research project is the development of hybrid materials to improve the performance of two important environmental and energy-related processes: the WGSR and the photocatalytic production of solar fuels such as hydrogen via photoreforming of renewable oxygenate compounds obtained from biomasses (i.e. alcohols). In particular, ternary hybrid materials comprising nanocarbon scaffolds, metal oxide and metal nanoparticles was carefully designed to achieve these purposes. A hierarchical synthetic approach was chosen to better integrate the properties of each component in the hybrid material. A carbon/inorganic hybrid with new properties as compared to single components is pursued. The nanohybrids are further structurally modified in such a way as to preserve or improve the catalytic properties of the specific phases.

Multi-walled carbon nanotubes are the first scaffolds tested in this study. A new synthetic protocol is developed with optimized post-synthetic treatments. Regarding the WGSR experiments, CeO_2 is chosen as the main component of the inorganic matrix. Its role is to act as co-catalyst of the active phase which consists of Pd nanoparticles. On the other hand, the production of hydrogen is carried out employing TiO_2 as photocatalyst deposited over the carbonaceous scaffold while Pd nanoparticles act as co-catalyst. Once optimized both the synthetic and the post-synthesis treatment protocols, interest is shifted toward the use of a less investigated carbon nanostructures which present additional benefits, such as carbon nanocones. Catalytic activities of all synthesized nanohybrids is carefully evaluated for WGSR or photocatalytic H_2 production.

Chapter 2

EXPERIMENTAL TECHNIQUES

In this chapter, the main experimental techniques employed in this work of thesis are summarized. The catalytic activity of the synthesized (photo)catalysts have been evaluated with respect to reactions relevant for H_2 production and the results have been correlated with the information from structural, textural and morphological characterizations.

2.1 CATALYTIC ACTIVITY MEASUREMENT

2.1.1 WGSR catalytic activity measurement

The tests to assess the catalytic activity of the prepared materials (CeO_2-based materials) with respect to the Water Gas Shift Reaction (WGSR) have been performed in a homemade apparatus, built and optimized in our research laboratory. The experimental apparatus is basically composed by a reagent mixing system, a furnace-controlled reactor and an analyzing system, as schematized in **Figure 2.1**.

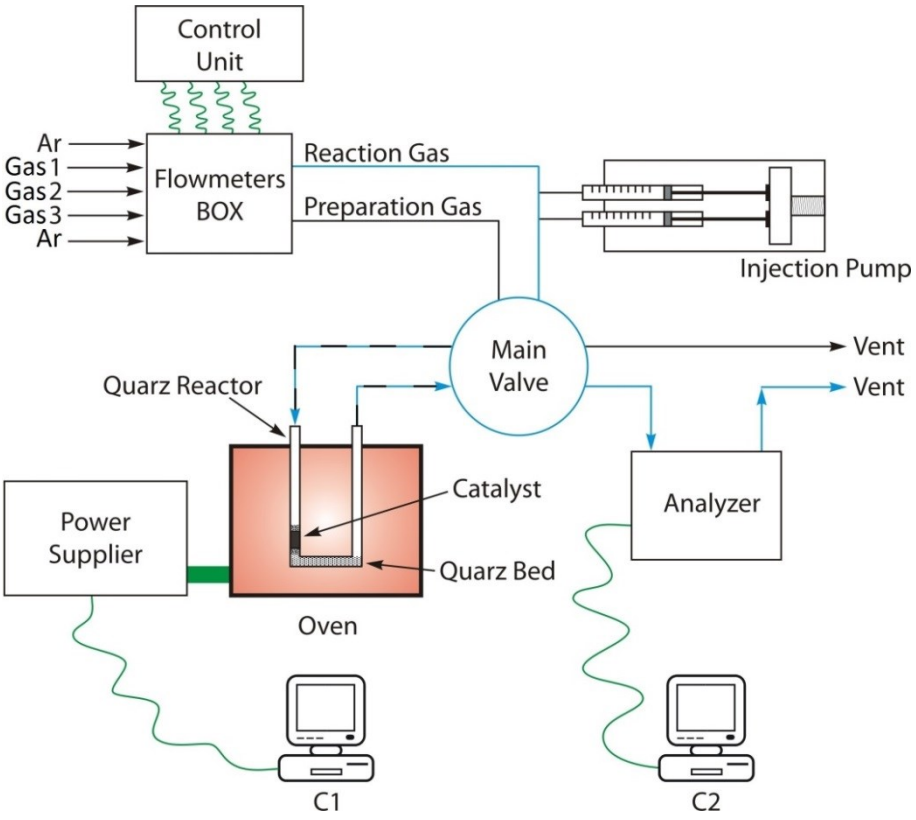

Figure 2.1: Experimental apparatus used for testing the activity of the catalysts in the WGSR.

The reagents mixing system is composed by a series of mass-flow controllers connected to a central control unit (Brooks Instruments). A valve system before the flowmeters allows the selection of the gas to be controlled on each: Ar (as inert gas) or other calibrated gas mixtures used as reagents (CO/Ar or CH_4/Ar) or for the pre-treatments of the materials (O_2/Ar and H_2/Ar). Two septa are located on the reaction line for the introduction of liquid reagents using a GASTIGHT syringe moved by an infusion pump (KD Scientific model KDS-101-CE). All the pipelines are heated in order to vaporise the liquid reagents before being introduced into the reactor. After the flowmeters, a 6-way valve allows to select which line passes through the reactor. In any case, the reaction line goes to the detector. In this configuration, it is possible to pre-treat the catalyst while it is possible to acquire the information on the composition of the reaction mixture bypassing the reactor.

The reactor is a U-shaped quartz microreactor with internal diameter of 4.0 mm. The catalyst is located between two layers of granular quartz, the typical inert material used for sustaining the catalyst powder. The reactor is heated by an electric

oven (Micromeritics) controlled by a digital regulator (Eurotherm 847). The actual temperature of the catalyst is measured with a K-type thermocouple inserted within the catalytic bed.

The reaction line is connected to a gaschromatograph (Agilent 7890) as online analyser. The GC is equipped with two columns and two detectors (Thermal Conductivity Detector, TCD and Flame Ionization Detector, FID). A Molsieve 5 Å column (50 m x ID 0.53 mm) followed by a TCD detector was used for the quantification of H_2, O_2, N_2, and CO. Ar was used as carrier in order to obtain high sensibility toward H_2. A Select Permanent Gases/CO_2 Plot Column (parallel PoraPLOT 50 m x 0.55 mm ID and Molsieve 5 Å 10 m x 0.32 mm ID columns) is instead used with a methanator and a FID detector for precisely quantifying CO, CO_2 (both transformed into CH_4 into the methanator) and CH_4. He was used as carrier in this case.

All catalytic tests were conducted at atmospheric pressure. The catalysts were pre-treated under Ar at 450 °C (40 mL min^{-1}, 10 °C min^{-1}) for 30 minutes. The aim of this cleaning under inert atmosphere procedure is the removal of possible residues of the synthesis that have stood the calcination treatment or adsorbed species (carbonates and moisture from air exposure) onto the catalyst surface. No other activation procedures (e.g. reduction) were applied.

Typically, ~ 40 mg of sample were used and a total gas flow rate were 48.5 mL min^{-1} to ensure a Gas Hourly Space Velocity (GHSV) value of 75000 mL g^{-1} h^{-1}. The WGSR reaction mixture was composed of 3.0 vol. % CO and 3.0 vol. % H_2O diluted in Ar. The gaseous mixture was introduced in the reactor at 200°C and the catalytic activity was measured for 4 hours. Then, the reactor temperature was increased stepwise up to 350°C (step each 25°C, heating rate of 2 °C min^{-1}), maintaining each temperature for 6 hours.

CO conversions (X_{CO}), CO_2 yield (Y_{CO2}) and H_2 selectivity (Y_{H2}) were calculated as follows:

$$X_{CO} = \frac{n_{CO,i} - n_{CO,f}}{n_{CO,i}} \qquad \textbf{Eq. 2.1}$$

$$Y_{CO\,2} = \frac{n_{CO2,f}}{n_{CO,i}} \qquad \textbf{Eq. 2.2}$$

$$Y_{H\,2} = \frac{n_{H2,f}}{n_{CO,i}} \qquad \textbf{Eq. 2.3}$$

where $n_{A,B}$ is the number of moles of gas A in the position B (i = before the reactor; f = after the reactor).

2.1.2 Photocatalytic activity measurement

The photocatalytic properties of the prepared photocatalysts (TiO_2-based materials) presented in this work were evaluated in terms of hydrogen production by photoreforming of ethanol and glycerol aqueous solution, respectively 50% v/v and 1 M. These are solutions representative of the purified aqueous solution produced from biomass processing, such as sugar fermentation (leading to ethanol/water solutions) or as bio-diesel production (leading to glycerol/water solutions). Experiments using aqueous methanol solution (50% v/v) or pure water were used in selected tests, mainly as benchmark sacrificial agent and to further investigate the reaction mechanism.

In a photoreforming experiment, 10 mg of photocatalyst were dispersed into 60 mL of aqueous solution containing the sacrificial agent by sonication in an ultrasonic bath for 30 minutes. Subsequently, the reactor was closed and an Ar flow (15 mL min^{-1}) was used to purge the system from the air. After purging for 40 minutes, the lamp was switched on and the gaseous products were transported to the analyzing system by the same Ar flow. During purging and catalytic runs, the photocatalyst was suspended by magnetic stirring and the reactor was thermostated at 20 °C. The online detection of gaseous and volatile products was carried out using a gaschromatograph equipped with two analytical lines. A 10 way-two loops injection valve was employed to inject the a portion of the gas effluent from the reactor into both the analytical lines. After the photocatalytic tests, the photocatalyst were recovered by filtration on a Millipore PVDF membrane (0.45 μm) and the collected solutions were subsequently analyzed by GC/MS to detect the non-volatile by-products accumulated in the liquid phase.

A typical experimental apparatus is composed by a light source, a reactor (in which the photocatalyst is suspended into the aqueous solution containing the sacrificial agent) and an analyzing system. In this work, two experimental setups with different geometry were employed, depending on the light source.

Immersion lamp photoreactor

This photoreactor setup was used essentially for two purposes: the evaluation of the activity of the materials under intensive UV-vis irradiation (mainly for comparison with literature data) and the determination of the quantum efficiency, under low power, monochromatic irradiation.

In the first case, the light source employed is a 125 W medium pressure Hg lamp (Helios Italquartz model UV13F) with a cylindrical irradiation geometry surrounded by a Pyrex reactor (**Figure 2.2**). The power density reaching the photocatalyst, measured on the external surface of the cooling jacket with a DeltaOHM radiometer HD2302.0, was 33 mW cm^{-2} in the UV range (300 – 400 nm) and 135 mW cm^{-2} in the vis-NIR range (400 – 1050 nm). In this case, 10 mg of the photocatalyst and 80 mL of aqueous solution of the sacrificial agent were used.

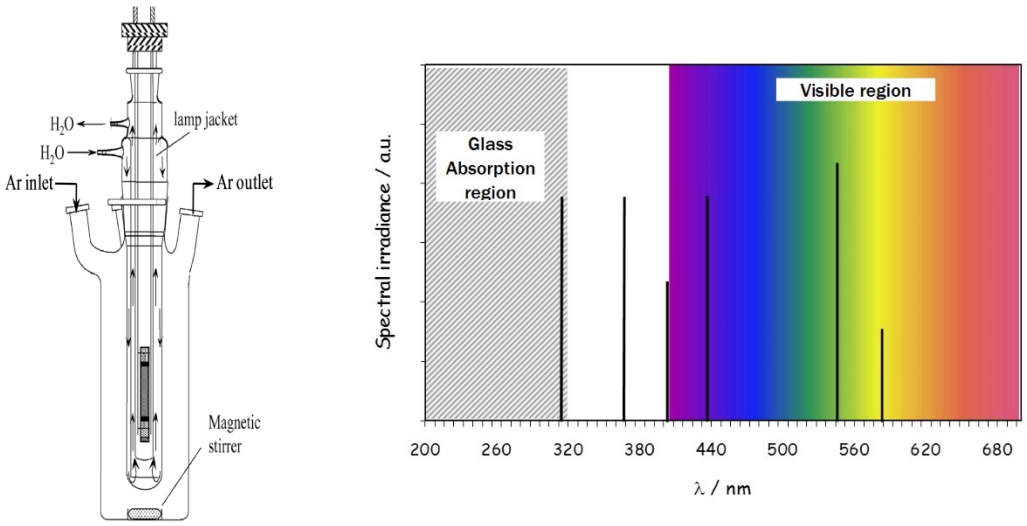

Figure 2.2: UV-vis light source and its Pyrex reactor (on the left) and medium pressure Hg lamp spectral emission (on the right).

A smaller version of this photoreactor was used for quantum efficiency determination. In this case, a PenRay 8 W Hg medium pressure lamp was used as monochromatic light source, emitting at 365 nm and reaching a power density of 1.10 mW cm^{-2}. The corresponding emitted photons ($5.62 \cdot 10^{16}$ photons/s) where calculated following **Equation 2.4**:

$$\text{Number of emitted photons} = \frac{P \cdot S \cdot \lambda}{h/C} \qquad \textbf{Eq. 2.4}$$

where P is the power density, S the irradiated surface, λ is the emission wavelength, h is the Plank constant ($6.626 \cdot 10^{-34}$ J·s) and C is the speed of light (approximately 3.00×10^{8} m s^{-1}).

In both the cases, the analyzing system was a gaschromatograph Agilent 6890N. It is equipped with two columns and two detectors (Thermal Conductivity Detector, TCD and Flame Ionization Detector, FID). A Molsieve 5Å column (Restek, 30 m x 0.53 mm ID) coupled with the TCD detector was used for the quantification of H_2, O_2, N_2, and CO. Ar was used as carrier in order to increase the sensibility toward H_2. A PoraPLOT Q column (Agilent, 30 m x 0.53 mm ID, 40 μm film) is instead used with a methanator and a FID detector for detection of volatile organic compounds (transformed into CH_4 into the methanator). He was used as carrier in this case.

Solar Simulator photoreactor

This setup was used to evaluate the activity of the materials under realistic solar irradiation condition, as expected in Sunlight-driven devices. The light source employed was a 150 W Xenon lamp (Lot-Oriel Solar Simulator) using an Atmospheric Edge Filter with a cut-off at 300 nm. This results in a surface power density of ~25 mW cm^{-2} in the UV range (300-400 nm) and ~180 mW cm^{-2} in the vis-NIR range (400-1050 nm) , approaching the conditions used in a solar concentrator. A Teflon-lined stainless steel photoreactor was irradiated from the top by the Solar Simulator (**Figure 2.3**).

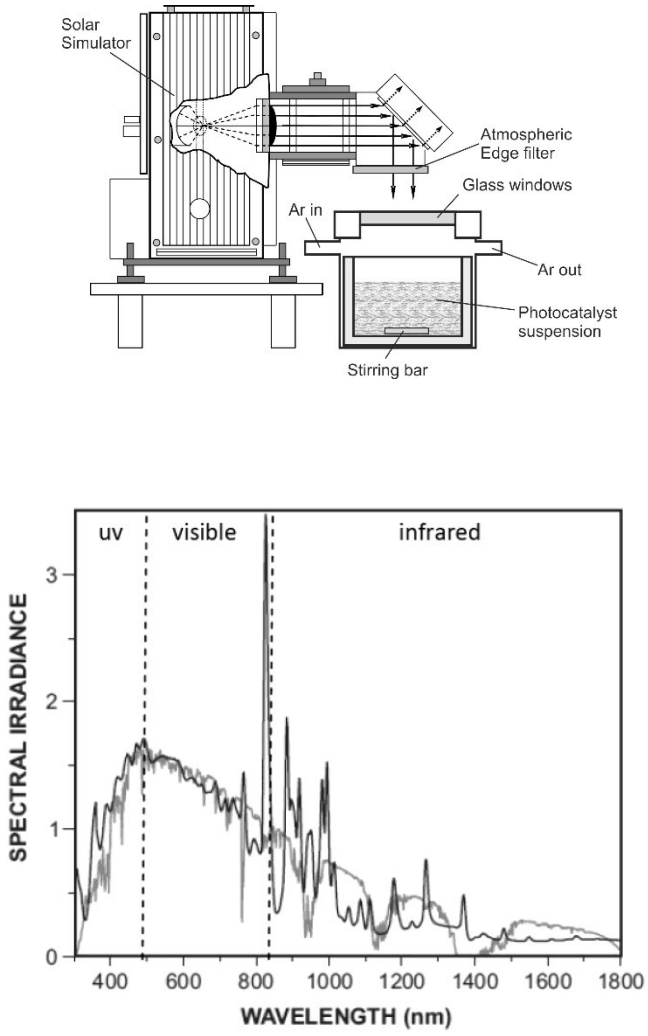

Figure 2.3: Solar Simulator and its Teflon-lined reactor (on the top) and Solar Simulator emission (black line on the bottom) compared to Sun emission (grey line on the bottom).

The analyzing system of this experimental apparatus was a gaschromatograph Agilent 7890A. It is equipped with two columns and two detectors (Thermal Conductivity Detector, TCD and mass spectrometer, MS). A Carboxen 1010 Plot column (Supelco, 30 m x 0.53 mm ID, 30 µm film) coupled with the TCD detector was used for the quantification of gaseous products. Ar was used as carrier in order to increase the sensibility toward H_2. A DB-225ms column (J&W, 60 m x 0.32 mm ID, 20 µm film) followed by MS (Agilent 5975C) is instead used for detection of volatile organic compounds. This column uses He as carrier.

Liquid phase analysis

The liquid phases were collected by filtration on 0.45 µm PVDF Millipore membrane after the catalytic runs and analyzed GC/MS (directly injecting the liquid in the DB-225ms column of the Solar Simulator apparatus) to detect the by-products accumulated. Internal standards, 1-butanol and 1-hexanol respectively for liquids from photoreforming of ethanol and glycerol, were used for a semi-quantitative analysis.

Quantum Efficiency measurements:

Quantum Efficiency (QE) was calculated as follows:

$$QE = \frac{2 \times mol_{H_2}}{\text{number of absorbed photons}} \qquad \textbf{Eq. 2.5}$$

the number of absorbed photons was calculate as the difference between the transmitted photons in the blank (aqueous solution of the sacrificial agent) and the transmitted photons in dispersed catalyst.

2.2 POWDER X-RAY DIFFRACTION (XRD)

X-ray crystallography is a well-established technique to explore the structure of a material. The method is based on the diffraction phenomena occurring when X-ray photons are scattered by the crystallographic planes of a lattice, and revolves in particular on the interference patterns given by the diffracted photons.

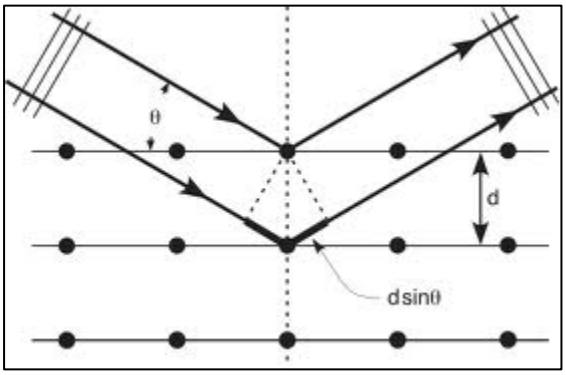

Figure 2.4: Schematic representation of X-ray diffraction principle.

The intensity of the diffracted beam is maximal when all the diffracted rays give constructive interference. This condition takes place when the Bragg's law is satisfied:

$$n\lambda = 2d\text{sen}\theta \qquad \textbf{Eq. 2.6}$$

where n is the order of diffraction, λ is the wavelength of the incident X-ray, d is the interplanar spacing and θ is the angle of incidence of the beam.

X-ray diffractograms reveal several important properties of a material, namely the crystallinity of the sample or of a particular component of it, an estimate of the size of the microcrystallites that may be present, the atomic constituents of the unit cell and so on.[89] Powder XRD was used in the current study to identify the composition of the phases and to estimate the average dimension of the crystallites. The powder XRD patterns were recorded with a computer-controlled Philips X'Pert diffractometer using Cu K_α radiation. The data were collected at 0.02 ° in the 2θ range from 10 ° to 100 °.

The experimental broadening of the XRD reflections is composed of many contributions, but it can be related to the size of the crystallites of the studied material, according to the Scherrer's equation:

$$\tau = \frac{K\lambda}{\beta cos\theta} \qquad \textbf{Eq. 2. 7}$$

where τ is the crystallites mean size, K is a constant which to some degree depends on the shape of the peak (in this work, K = 0.9), λ is the X-ray wavelength (in this work, λ = 0.154 nm correspondent to the Cu $K_{\alpha 1}$), β is the corrected Full Width at Half Maximum (FWHM) of the reflections and θ is the Bragg angle. The value of β is determined from the experimental broadening of the reflections β_{obs}, after subtraction of the instrumental broadening (β_{inst}, determined acquiring the XRD pattern of a sample with crystallites larger than 300 – 400 nm):

$$\beta^2 = B_{obs}^2 - B_{inst}^2 \qquad \textbf{Eq. 2. 8}$$

According to the Scherrer's equation, reflections having larger FWHM coincide with lower dimension of the crystallites. For the same principle, non-crystalline materials show no sharp diffraction reflections, but only broad features, because of the absence of a long-range order.[89] However, it should be noticed that the Scherrer's equation only provides a lower bound on the particle size, because the reflections may be broadened by a variety of factors besides crystallite size. Some examples of reflection broadening sources may be dislocations, stacking faults, residual stresses, grain boundaries, impurities, *etc.* If all of these contributions were zero, then the peak width would be

determined solely by the crystallite size and the Scherrer formula would apply. However, if the other contributions to the peak width are non-zero, then the actual crystallite size is larger than that predicted by the Scherrer formula.

X-ray Diffraction (XRD) patterns were collected on a Philips X'Pert diffractometer using a monochromatized Cu Kα ($\lambda = 0.154$ nm) X-ray source in the range $20° < 2\theta < 100°$. The mean crystallite sizes of the TiO_2 and CeO_2 were calculated by applying the Scherrer equation to the anatase (101) reflection and to the CeO_2 (111) reflection. The phase composition of the samples has been determined by Rietveld analysis, using the PowderCell 2.3 program. The experimental XRD patterns were compared with the theoretical XRD profiles built on the basis of the known cell parameters of the crystallographic phases required (mainly CeO_2 and anatase TiO_2).

2.3 RAMAN SPECTROSCOPY

Raman scattering, based on the inelastic scattering of monochromatic light, is a valuable technique to study vibrational and rotational excitations of molecular systems or crystalline materials. This technique is based on the scattering by a monochromatic beam by the atoms of the sample. Usually, a laser beam in the visible or NIR range is used, although instruments working with UV lasers could be used for specific applications.

Raman spectroscopy is a technique complementary to IR spectroscopy, since Raman and IR bands could lie at different wavenumbers because of the different selection rules between the two techniques. In fact, only transitions that induce a change in polarizability of the molecules are active in Raman spectroscopy.

When a photon beam passes through a material, a fraction of the incident beam is diffused. This fraction can be divided into two parts. The first derives from the elastic interaction with the material (without energy variation), giving the so-called Rayleigh radiation.

On the other hand, the phenomenon that allows to investigate the structural feature of a material is the inelastic scattering that the beam suffers by interaction with the material, the so-called Raman scattering. Raman signals are very weak with respect to the Rayleigh scattering considering that only a very small fraction of the photons (about 1 over 10^7) is subjected to inelastic scattering. Raman signal can have a higher or lower

energy with respect to the incident beam (**Figure 2.5**), arising to anti-Stokes and Stokes signals, respectively. The energy difference between Rayleigh and Raman signals corresponds to the energy difference between the vibrational levels of the normal mode involved in the transition.[90]

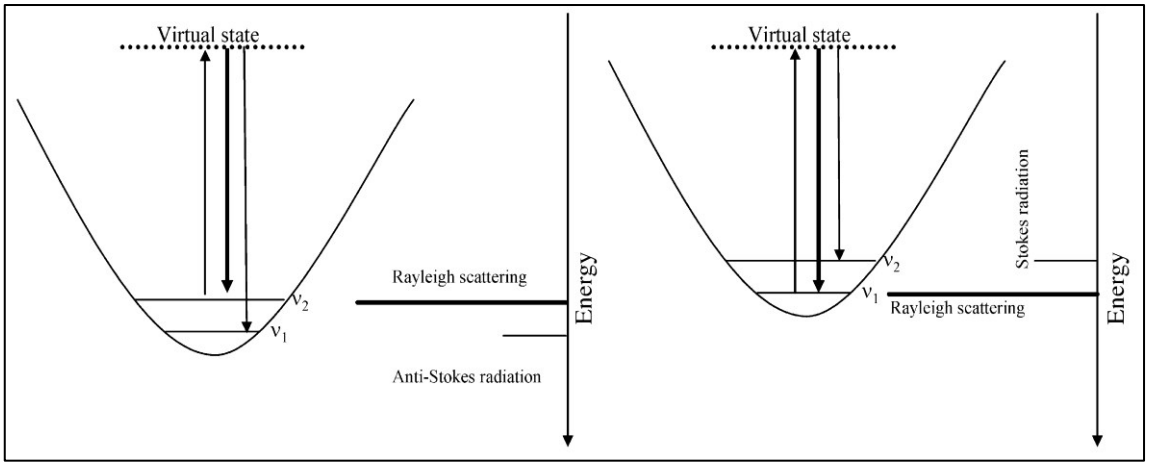

Figure 2.5: Schematic representation of Rayleigh and Raman signals (anti-Stokes on the left and Stokes on the right).[90]

Stokes signals are originated by an energy transfer from the photon to the material, resulting in diffusion of photons with lower energy. On the other hand, the energy transfer involved in emission of anti-Stokes signals takes place from the material to the photons, that are diffused at higher energies.

The intensities of Raman signals depend on the populations of the respective initial energy levels, that are given by the Boltzmann equation:

$$\frac{I_{anti-Stokes}}{I_{Stokes}} = \frac{N_{v=1}}{N_{v=0}} = e^{-\frac{hc\nu}{kT}} \qquad \textbf{Eq. 2. 9}$$

where I are the signals intensities, N the populations of the levels, ν the frequency related to the transition energy, *h* Planck constant, *c* the light speed in the vacuum, *k* Boltzmann constant and *T* the absolute temperature. From this equation, it is possible to deduce that the intensity of anti-Stokes signals is lower than that of Stokes ones, because of the scarce population of the ν_1 level at room temperature. As a consequence, a high number of spectra must be accumulated to evidence anti-Stokes signals from the noise background. For this reason, the Stokes part of the vibrational spectrum is usually acquired by Raman spectrometers.

The Raman spectra of the samples presented in this work of thesis was recorded using a inVia Raman Microscope by Renishaw equipped with a Nd:YAG laser using an excitation wavelength of 532 nm. This is a microRaman instrument that, coupling the Raman spectrometer to an optical microscope, allows the acquisition of Raman spectra of different zones of the samples. The Raman spectra have been collected at a magnification of 50x in the range $100 < cm^{-1} < 3200$, with a laser power of 1 mW.

2.4 TRANSMISSION ELECTRON MICROSCOPY TECHNIQUES

In the field of heterogeneous catalysis and photocatalysis, the design of more active and selective catalysts often relies on the precise identification of active sites. Sophisticated imaging methods that enable detailed characterization of a sample at the nanometer and atomic level are of pivotal importance.[91] Among many characterization techniques, advanced electron microscopy techniques are the most powerful to get information on the individual components of a heterogeneous material. These techniques are essential to understand the properties of heterogeneous catalysts and to provide useful information for the development of nanostructured materials. Using modern electron microscopes it is possible to directly observe small particles, clusters or even single atoms of a sample, while all other techniques (*e.g.* X-ray techniques, IR spectroscopy, NMR spectroscopy) provide information averaged over millions to trillions of components, or they require stringent conditions on the samples to be examined (*e.g.* Scanning Probe Microscopy techniques).[91]

Transmission Electron Microscopy (TEM) techniques overcome the limitation of light microscopes for imaging very small objects, thanks to their higher resolution. The resolution of a microscope is the minimum distance between distinguishable objects in an image and two different and unrelated aspects limit it: aberration and diffraction. Aberration can be explained by geometrical optics and can (in principle) be solved by increasing the optical quality of the system. Diffraction is instead strictly related to the nature of the wave used for the observation.

The maximum theoretical resolution of a microscope, limited by diffraction alone, is related to the wavelength of the radiation used according to the Rayleigh criterion, that leads to the simplified statement that the limit of resolution of any imaging process is on the order of the wavelength of the wave used to image it. It follows that the maximum

theoretical resolution of a good light microscope (hundreds of nm) is not useful to characterize the typical nanocomponents of a heterogeneous catalyst. On the other hand, the maximum resolution for an electron microscope is adequate to get nanoscopic resolution, and can be calculated referring to de Broglie's wavelength of the particle:

$$\lambda = \frac{h}{p} \qquad \textbf{Eq. 2.10}$$

where p is the particle momentum, λ is the particle wavelength and h is the Planck's constant.

In the TEM apparatus the electrons are accelerated by a potential drop, V, acquiring a potential energy eV that is converted to kinetic energy of the electrons at the end of the accelerating section of the instrument. Equaling the two energies, an expression of momentum as a function of the potential is derived:

$$eV = \frac{1}{2} m_0 v^2 \qquad \textbf{Eq. 2.11}$$

$$p = \sqrt{2 m_0 eV} \qquad \textbf{Eq. 2.12}$$

The value of λ can be obtained substituting **Equation 2.12** in **Equation 2.10**. For example, an electron accelerated to 100 keV has a wavelength (which more or less corresponds to the maximum theoretical resolution of a microscope) of about 0.004 nm, which is 100 times smaller than the diameter of an atom. Moreover, by increasing the accelerating voltage the wavelength of the electrons would decrease. However, it must be pointed out that **Equations 2.1**0 - **2.12** do not take into account relativistic effects, that cannot be ignored for energies above 100 keV. In addition to this intrinsic limitation, considerable practical limitations involved in the microscope construction must be taken into account, such as aberration limits and non-homogeneity of the magnetic fields used as lenses. Nonetheless, atomic scale resolution is attainable using modern instruments. Using aberration correctors (usually referred to as C_s-TEM), it is possible to dramatically improve the spatial and spectral resolution of the electron microscope even when using lower accelerating voltages (**Figure 2.6**).[91] This is particularly advantageous since a lower accelerating voltage generally leads to less sample damage from the electron beam.

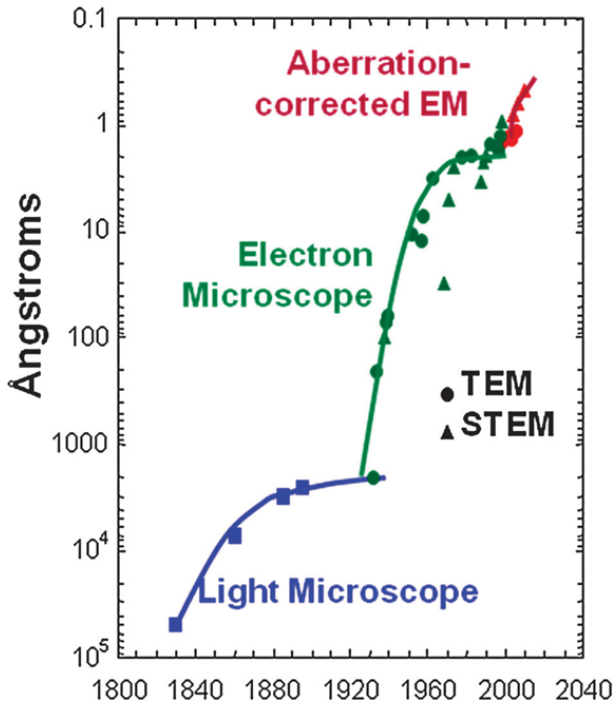

Figure 2.6: Spatial resolution versus year for optical microscopes and electron microscopes. Currently, best point-to-point spatial resolution is 0.5 Å.[91]

A typical Transmission Electron Microscope (TEM) consists of a vertical column in which the electron beam passes from an electron source at the top, through the specimen and down to the bottom of the column where the image is formed and revealed (**Figure 2.7**). The column is held under ultra-high vacuum (UHV) conditions by a system of high performance pumps in order to reduce the scattering of the electron beam by gas atoms. Electromagnetic coils that function as lenses are positioned around the column along its length and work in an analogous way the optical lenses do in a light microscope. Apertures of different diameters can be inserted into the electron beam at several positions along the column. This is done to select part of the beam and exclude the contribution of the rest. There are two common types of electron sources, which are characterized by the way in which the electron beam is generated (thermionic emission source or field emission gun).

After electrons are produced, they are focused and accelerated by an electrostatic field and they enter into the TEM column. The strength of this field determines the kinetic energy of the electron beam (**Eq. 2.11** and **2.12**). In practice, an applied potential of at least 100 kV is advisable for HRTEM.

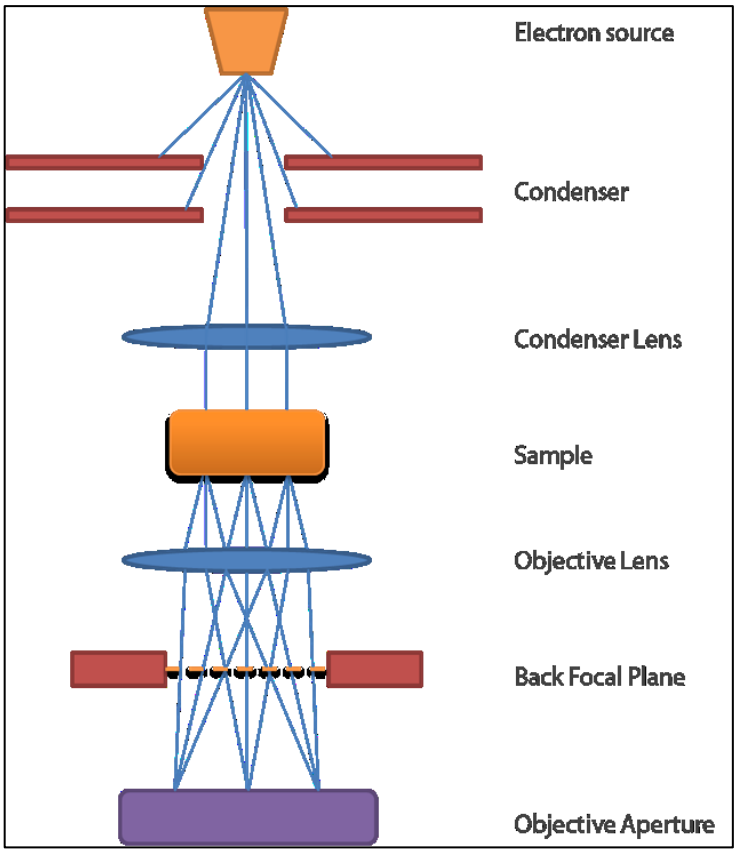

Figure 2.7: Schematic representation of the TEM column. Blue lines represent the electron beams.

The condenser apertures and lens system select the electrons and focus them in a parallel beam, setting the beam diameter to a desired value. Then, the electron beam passes through the specimen, which is mounted on the specimen holder. The incident beam interact with the internal crystal structure of the sample and emerges as a set of diffracted and non-diffracted (transmitted) beams. These beams are again focused by the objective lens on the Back Focal Plane (BFP). In this plane, the diffraction pattern is formed.

Considering the rules for diffraction (similarly to single crystal X-ray diffraction) each spot is related to one family of crystal planes at one particular orientation. The objective lens performs a Fourier Transform on the exit wave to form the diffraction pattern, that is processed via inverse Fourier Transform to construct an image closely related to the internal structure of the sample. Images and diffraction patterns are visualized on a fluorescent screen and may be digitally recorded using a camera positioned below the fluorescent screen.[92]

The diffraction pattern contains electrons from the whole area of the specimen illuminated by the beam and is not very useful because the specimen will often be buckled and because the direct beam is often so intense that it will damage the camera. Therefore, there are basic TEM operations that allow both to select a specific area of the specimen to contribute to the diffraction pattern and to reduce the intensity of the diffraction pattern reaching the screen. There are two ways to perform this operation: either the beam is made smaller, or an aperture is inserted above the specimen so that only electrons passing through it may hit the specimen. Usually the second way is applied: this operation is called Selected-Area Diffraction (SAD).

After the diffraction pattern area is selected, it is possible to perform the two most basic imaging operations in the TEM. It is possible to form the image in the TEM by using the central spot or some of the scattered electrons. If the direct beam is selected, the resultant image is called bright field (BF) image, while if scattered electrons of any form are selected, the resultant image is called dark-field (DF) image. The BF detector is aligned to the transmitted beam in the TEM column while the DF detector is usually annular and surrounds the BF detector. An image obtained with the annular detector is called Annular Dark-Field (ADF) image. The DF detector will collect not just scattered electrons but also some Bragg electrons. To get an image formed only by scattered electrons another detector can be used, placed at very high angles, called High-Angle ADF (HAADF) detector. The images collected with this detector are sometimes called Z-contrast images because the signal strength of the high-angle scattered electrons is proportional to approximately Z^2 (in the limit of electron single scattering). This technique is particularly advantageous for detecting supported heavy-metal particles. The complete HAADF detector set-up for Z-contrast imaging in a scanning TEM (STEM) is depicted in **Figure 2.8**.

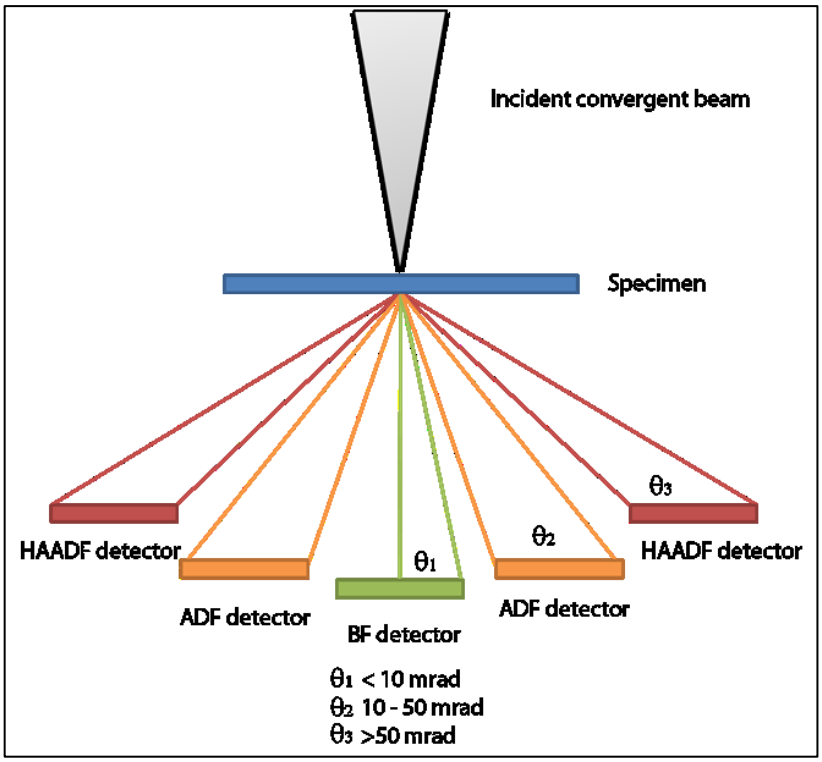

Figure 2.8: Schematic representation of the HAADF detector set-up for Z-contrast imaging in a STEM. The conventional range of electron scattering angles gathered by each detector is also reported.

HRTEM is a very powerful technique for the characterization of crystallinity, defect structure, symmetry, morphology and facets of individual nanoparticles. However, it presents some limitations which must be remembered. Since it is a transmission technique, the samples must be electron transparent and, in addition, must be thin enough to minimize multiple diffraction of the electrons. Generally, the specimens must have a thickness below 100 nm, or in some cases below 50 nm. Moreover, the high energy electron beam may alter and damage the specimen by heating it or by reducing susceptible materials such as some oxides. Nonetheless, it must be taken into account that HRTEM images are 2-D representation of a 3-D set of objects viewed by transmission rather than reflection, and sometimes the third dimension cannot be neglected. Recent developments in electron tomography (ET) and quantitative STEM have further expanded the abilities of TEM by allowing 3-dimensional (3D) reconstructions of nanomaterials instead of only 2-dimensional (2D) projections.[93]

STEM operation mode is another way to perform the analysis of the specimen, consisting in scanning a focused convergent beam over the sample using a system of

additional lenses, usually incorporated in the instrument. This operation mode has the advantage that the sample does not have to be moved to get more than one image. Moreover, less noisy images than TEM DF can be obtained via the combination of the STEM mode with the ADF detector. The ability to quantify the size of individual nanostructures in the STEM is primarily determined by the size of the electron beam and the stability of the nanoclusters under the intense electron irradiation of the beam. The recent development of aberration correctors for STEM has largely improved the spatial resolution allowed by these instruments, taking the resolution to less than 0.1 nm. However, this advance does not automatically improve sensitivity/accuracy when the size measurement is limited by electron irradiation effects such as chemical changes and the movement of the nanoclusters on the support surface.

Inelastic interactions of the beam electrons with the specimen, in which energy is transferred, also provide useful complimentary information and several analytical techniques have grown up around the TEM to exploit this. Energy transfer from an incoming high energy electron to one of the core electrons of an atom may result in ionization of the atom, forming a hole in the core. An electron in a higher energy level of the atom may then recombine with this hole, releasing its excess energy as an X-ray photon. The frequency of these photons is determined by the difference between the two electron energy levels and will therefore be characteristic of the nature of the atom from which it was emitted. In X-ray Energy Dispersive Spectroscopy (XEDS or EDX), these X-ray photons are collected and number of counts plotted against their energy to give a spectrum. This technique allows quantitative measurement of the elemental composition of the area of the sample illuminated by the beam and provides information which is not available from High resolution TEM (HRTEM) itself. For this reason, XEDS spectrometer is commonly fitted to the modern TEM.

TEM measurements were performed on a TEM Philips EM208, using an acceleration voltage of 100 kV. Samples were prepared by drop casting the dispersed particles onto a TEM grid (200 mesh, copper, carbon only). HRTEM were acquired on a JEOL 2200FS microscope operating at 200 kV, equipped with an Energy Dispersive Spectrometer (EDS), in-column energy (Omega) filter, and High-Angle Annular Dark-Field (HAADF) detector.

2.5 N_2 PHYSISORPTION

The activity of heterogeneous catalysts is strictly related to the morphology and the extension of their surface area. Indeed, gas reactions catalyzed by solid materials take place on those active sites of the catalyst that are in contact with the reactants phase, *i.e.* that are located on the catalyst interior or exterior surfaces accessible to the reactants. If the pores are wide enough to permit the diffusion of reactants and products to and from the active sites, the activity is directly proportional to the number of active sites. This principle is valid for all heterogeneous catalytic reactions, allowing to study the reactions under kinetic control.[89] Otherwise, if pores are too narrow, the reaction is limited by the mass transport of reactants from the gas phase to the active site, and it is said to be under diffusional control. In this case the activity could be independent of the surface area or proportional to its square root, depending on the mode of diffusion. It is deduced that the catalytic activity of a solid material is not only influenced by its surface area, but also by its pore structure (texture and dimensions of the pores). For example, a particular pore structure may induce a shape selectivity to a reaction, limiting the diffusion of one particular reactant or product.[89]

Even in the same material, pores can vary in shape and dimension in a wide range. Pores can be divided into three groups on the basis of their dimensions:

- micropores are pores having diameters smaller than 2 nm;
- mesopores have diameters in the range 2 – 50 nm and are typical of non-crystalline materials;
- macropores have diameters larger than 50 nm.

The ability to measure the surface area of a catalyst and the dimension and distribution of its pores is therefore essential to any catalytic study.

In the present work, N_2 physisorption experiments were carried out on a Micromeritics ASAP 2020C. The samples were first degassed in vacuum at 120 °C for 12 hours prior to N_2 adsorption at liquid nitrogen temperature.

2.5.1 Estimating Surface Area

Among the well-established methods that are used to determine the surface area of a porous solid, the most commonly employed is the volumetric method. This method is widely used for determining the surface area and pore size distribution of a variety of different solid materials, such as ceramic, industrial adsorbents and catalysts.[94,95] The volumetric method consists in measuring the adsorption of an inert gas on the solid at a given constant temperature as a function of the partial pressure of the adsorbent. Notably, a fundamental requisite to apply this technique is that the interaction between the adsorbent molecules and the material surface has to be weak. Therefore, only a physical interaction must take place. This process allows to obtain a physisorption isotherm. On the basis of the isotherm shape, it is possible to determine the surface area and pore distribution of the sample, according to empirical equations and adsorption models.[89]

Since physisorbed molecules are not restricted to specific sites but are free to completely cover the surface of the solid, the method allows to estimate the total surface area of the sample. Furthermore, since the interactions that lead to the adsorption are reversible and weak, the process does not modify the surface of the sample, so is not invasive. The process is also reversible, so both adsorption and desorption processes can be studied. Moreover, because many molecular layers of adsorbate can be formed, the pore volume may be measured if the amount of adsorbate needed to completely fill the pores can be extrapolated. According to the International Union of Pure and Applied Chemistry (IUPAC) recommendations,[94] the majority of physisorption isotherms can be classified into six types, that are displayed in summarized in **Figure 2.9**.

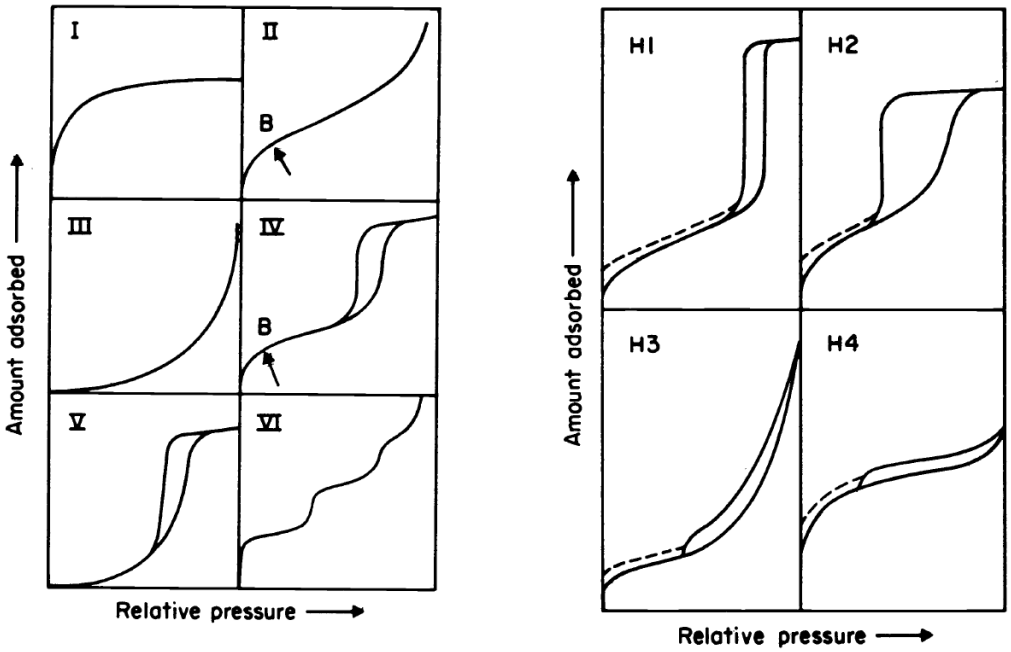

Figure 2.9: Physisorption isotherm types and hysteresis classification according to the IUPAC recommendations (Adapted from Sing et *al.*).[94]

The standard physisorption isotherms can be described as follow:

- Type I isotherms are given by microporous solids having relatively small external surfaces, such as activated carbons and zeolitic molecular sieves.
- Type II isotherms are typical of non-porous or macroporous solids, on the surface of which unrestricted monolayer-multilayer adsorption takes place.
- Type III isotherms are not common. They are convex to the relative pressure axis over their entire range and, as we shall discuss later, are not useful to extrapolate the surface area of the solid. The adsorbate species may be replaced by another one in order to get another type of isotherm.
- Type IV isotherms are given by many industrial adsorbents. They present a hysteresis loop, which is associated with capillary condensation taking place in mesopores and can vary to a great extent depending on pores geometry. The hysteresis loop is also very important for determining the pore distribution of the material. According to the IUPAC recommendations, these are grouped in four types (H1-H4 in Figure 2.1), basing on their shape. H1 type is observed for compact agglomerates of spherical particles with rather uniform dimensions and disposition, while H4 type is observed for adsorbents made of agglomerates of bi-dimensional particles. H2 and H3 hysteresis types are observed for intermediate situations. Hysteresis are often not

easily classified, as most of the materials show heterogeneous distributions in shapes and dimensions of pores.

- Type V isotherms are uncommon and related to type III isotherms: the adsorbent-adsorbate interaction is weak.
- Type VI isotherms represent stepwise multilayer adsorption on a uniform non-porous surface.

In order to estimate the total surface area of a material using the volumetric method, the completion of an adsorbed monolayer has to be detected from the isotherm shape by some means. This is possible only for isotherm types I, II and IV. For isotherm type I, the adsorption is usually described adequately by the Langmuir equation.

$$\frac{V}{V_m} = \frac{\mathrm{bp}}{1 + \mathrm{bp}} \qquad \textbf{Eq. 2.13}$$

where p is the pressure of gas, b is a constant derived from kinetic principles that depends on temperature and adsorption heat, V is the volume of adsorbed gas and V_m is the volume of adsorbed gas forming a theoretical monolayer on the surface of the material. In order to determine the monolayer volume from empirical data, the Langmuir equation can be rearranged into:

$$\frac{\mathrm{p}}{\mathrm{V}} = \frac{\mathrm{p}}{\mathrm{V_m}} + \frac{1}{\mathrm{bV_m}} \qquad \textbf{Eq. 2.14}$$

Therefore, a plot of p/V *vs* p will give a straight line, the slope of which is $1/V_m$, the inverse of the monolayer volume.

For isotherm types II and IV instead, the Langmuir equation does not hold through because multilayer coverage takes place. The monolayer coverage may be extrapolated roughly by referring to the ordinate value of the inflection of the isotherms, known as the point B (**Figure 2.9**). The point B method may be used only if the beginning of the almost linear section of the isotherm is well defined, that is, if a sharp change of curvature is noted. Otherwise, a more sophisticated analysis of the isotherm is required and the surface area can be calculated by extrapolation of the monolayer volume applying the Brunauer-Emmett-Teller (BET) theory. The BET model starts from the assumption that adsorption is a reversible process consisting in the formation of a series of layers, where the most

external one is formed by adsorbate molecule directly in equilibrium with the vapor phase. Based on these principles, the BET equation is derived:

$$\frac{p}{V(p^0 - p)} = \frac{1}{V_m C} + \frac{C - 1}{V_m C} \cdot \frac{p}{p^0} \qquad \textbf{Eq. 2.15}$$

where p is the gas pressure, p^0 the saturated vapor pressure of the liquid at the operating temperature, V is the volume of adsorbed gas, V_m is the volume of monolayer coverage and C is the BET constant (that depends on temperature and interactions between adsorbent and adsorbed species). Plotting $p/V(p^0\text{-}p)$ *vs* p/p^0 usually gives a straight line in the range of $0.05 < p/p^0 < 0.35$, and from the slope and intercept the monolayer coverage volume is determined.

Once the monolayer coverage volume V_m is known, the available surface area is calculated from the equation:

$$S = \frac{V_m}{V_{mol}} N_A a_m \qquad \textbf{Eq. 2.16}$$

where V_{mol} is the molar volume of the adsorbate (at the same temperature and pressure of V_m), N_A is the Avogadro's number and a_m is the cross-sectional area of an adsorbed molecule ($a_m = 0.162$ nm^2 for N_2 at the liquid nitrogen temperature).

2.5.2 Estimating Pore Volume and Diameter

Many methods have been developed to estimate pores distribution of solid materials. In this study, the gas adsorption method will be employed. This method is based on the physisorption process, just like the volumetric method used to assess the surface area of solid materials.[89] In this case, however, one wants to observe just one particular phenomenon of the physisorption process, that is the capillary condensation of the gas used as adsorbate. The capillary condensation takes place in narrow pores at pressure less than the saturation pressure of the adsorbate. The capillary condensation in cylindrical pores is described by the Kelvin equation:

$$\ln \frac{p^0}{p} = \frac{2V\gamma \cos \alpha}{rRT} \qquad \textbf{Eq. 2.17}$$

which is obtained by equating the work spent in enlarging a spherical drop of liquid to that done in adding molecules to the interior of the drop. In this case, p^0 is the vapor pressure at the operation temperature, p is the pressure of the gas, V is the molar volume of the gas, α is the contact angle of the liquid on the pore surface, γ is the surface tension of the liquid, r is the radius of the pore, R is the gas constant and T is the absolute temperature of operation. Basing on this equation, a pore size distribution curve can be constructed, plotting the volume of adsorbed gas *vs* the diameter of the pores calculated for each p/p^0.

From this simple equation, it is also possible to understand that the formation of the hysteresis loop in the physisorption isotherm is related to particular shapes of the pores. In fact, in the case of cylindrical pores, the capillary condensation takes place at the same partial pressure during both the adsorption and desorption processes. The hysteresis loop is originated by the fact that, during desorption, evaporation of the gas takes place at a lower p/p^0 with respect to the condensation during adsorption. Therefore, evaporation takes place on pores with a diameter smaller than that of pores where capillary condensation occurs. This situation can be rationalized only assuming the formation of neck-bottle pores, in which the apertures have diameters smaller than the cavities.[89]

The Kelvin equation is a powerful method for investigating the pore distribution of a sample, but is insufficient in order to interpret correctly the experimental results obtained via the gas adsorption method. A model of the porous structure of the material is needed. Many different pore models have been developed, some qualitative and some much more complicated based on mathematical simulations. One of the differences among them arises from the pores dimension range in which they can be applied. In the present work, particular attention is given to mesopores. The method commonly used to describe mesopores (and small macropores) distribution is that developed by Barret, Joyner and Halenda (BJH method).[96] Analyzing the physisorption isotherm in the $0.40 < p/p^0 < 0.98$ range (region comprised between the formation of the monolayer and the saturation of the system, equivalent to a complete filling of pores), it is possible to obtain the mesopore volume and pore distribution.

2.5.3 Assessment of microporosity

It is generally accepted that the mechanism of physisorption is modified in very fine pores (i.e. micropores) since the close proximity of the pore walls gives rise to an increase in the strength of the adsorbent-adsorbate interaction. As a result of the enhanced adsorption energy, the pores are filled with physisorbed molecules al low p/p^0.

The most common method employed to assess the contribution of micropores in the physisorption isotherm of a sample is *t*-plot analysis proposed by Lippens and De Boer.[97] It is based on the plotting of the standard isotherm with *t*, the statistical thickness of the film of the physisorbed molecules calculated as:

$$t = \frac{n}{n_m}\,\sigma \qquad \textbf{Eq. 2.18}$$

where n are the mol of physisorbed molecules at a certain p/p^0, n_m are the mol of physisorbed molecules corresponding the formation of the statistical monolayer and σ is the thickness of a single molecular layer (0.354 nm for N_2 at the liquid nitrogen temperature). From a practical point-of-view, the statistical thickness *t* (in nm) is calculated from p/p^0 by the formula:

$$t = 0.1 * \left(\frac{13.99}{0.034 - \log(p/p^0)}\right)^{1/2} \qquad \textbf{Eq. 2.19}$$

Following this approach, the physisorption isotherm is converted into the t-plot, as represented in **Figure 2.10**.

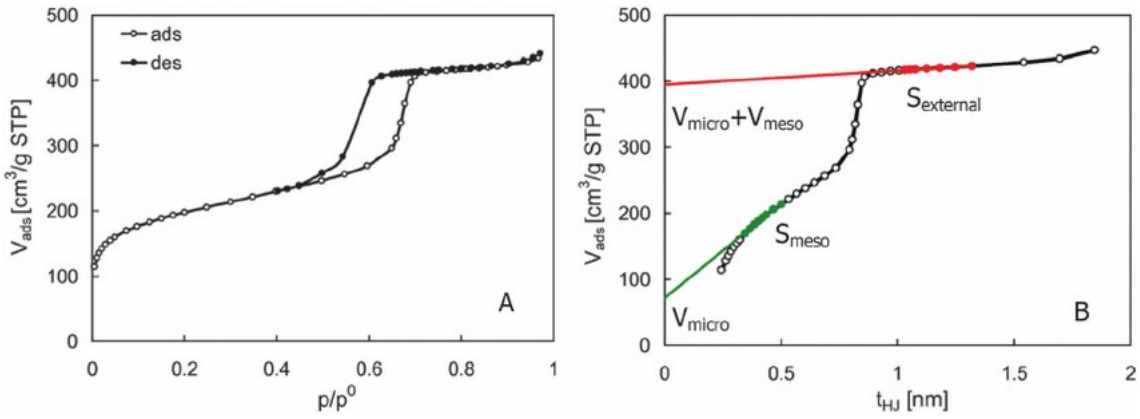

Figure 2.10: Example of a N_2 physisorption isotherm and its correspondent *t*-plot.

The *t*-plot is characterized by essentially two linear sections, with a stepwise increment between them due to capillary condensation within mesopores. The linear part at lower *t* values (usually between 0.5 and 1 nm) can be fitted as:

$$V_{ads} = V_{micro} + k * S_{meso} * t \qquad \textbf{Eq. 2.20}$$

where V_{ads} is the adsorbed volume, V_{micro} is the volume adsorbed within the micropores, S_{meso} is the surface related to mesopores and k is a constant ($= 1/4.3532\ n_m$ where 4.3532 is a coefficient for calculation of occupied area in $m^2\ g^{-1}$ from adsorbed amount $cm^3\ g^{-1}$ STP for N_2 adsorption at the liquid nitrogen temperature).

The second linear section of the *t*-plot can be fitted in a similar way:

$$V_{ads} = (V_{micro} + V_{meso}) + k * S_{external} * t \qquad \textbf{Eq. 2.21}$$

where V_{meso} is the volume adsorbed within the mesopores and $S_{external}$ is the surface outside the pores of the material. Obviously, the volume of mesopores (V_{meso}) ic calculated as difference between the two intercepts.

Finally, the real volume of micro- and mesopores are calculated converting the volume adsorbed at STP conditions into the correspondent liquid volume by the formula:

$$V_{real} = V_{ads} \cdot C \qquad \textbf{Eq. 2.22}$$

where C (= 0.0015468) is the conversion factor between the volume adsorbed at STP conditions into the correspondent liquid volume.

2.6 CHEMISORPTION

Chemisorption is based on a specific interaction between a probe molecule and the metal surface that constitute the active phase of a catalyst.[89] The probe molecule is able to chemically react with the metal, producing a single layer of chemisorbed molecules. The measure of the volume of gas consumed for the formation of the monolayer allows the calculation of the area of the active phase and consequently its dispersion. A typical chemisorption isotherm is shown in **Figure 2.11**.

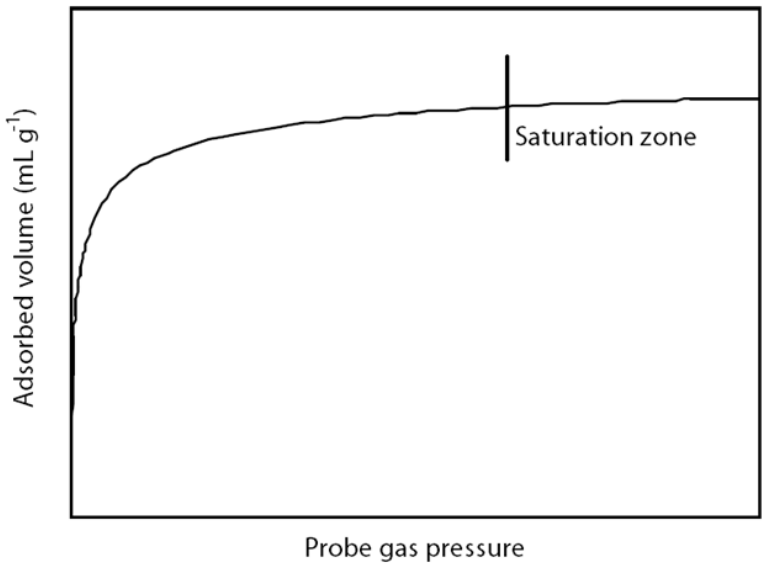

Figure 2.11: Typical chemisorption isotherm.

The number of surface metal atoms $N(s)_M$ and the active metal surface S_M can be obtained from the following equations:

$$N_{(S)M} = n\frac{V}{V_m}N_A \qquad \textbf{Eq. 2.23}$$

$$S_M = N_{(S)M}a_M \qquad \textbf{Eq. 2.24}$$

where V is the volume of adsorbed gas, V_m is the gas molar volume, N_A is the Avogadro's number and n is the chemisorption reaction stoichiometry (the number of metallic atoms that are needed to bind a single molecule of adsorbate) and a_M is the cross-sectional area of the metal atoms.

The most common gases used for chemisorption studies are hydrogen and carbon monoxide. Notably, many other gases can be used as probe for chemisorption. The best choice of the gas depends on the nature of the metal and of the support included in the formulation of the catalyst under analysis.

Generally, the chemisorption stoichiometry with hydrogen is assumed to be 2, because H_2 can be activated by the metal surface and subsequently dissociated, each hydrogen atom forming a bond with one metal atom. On the other hand, the stoichiometry of adsorption CO on metals (such as Pd and Pt) is assumed to be 1. These assumptions are not always true: actually, for very small nanoparticles the stoichiometric coefficient

of CO may vary, because of the formation of geminal di-carbonylic species on edge and vertex atoms.[98] Similarly, in the case of H_2 the stoichiometric coefficient may vary for extremely dispersed particles (lower than 1nm), but also the formation of metals hydrides and spillover effects (especially in reducible oxides) can alter the measurement.[99] These phenomena must be taken into account during planning of the measurements and evaluating the experimental results.

In the case of non-dissociative adsorption (as is the case of CO) the Langmuir isotherm equation can be applied, assuming a constant chemisorption energy:

$$n_{ads} = \frac{n^{m}_{ads} bp}{1 + bp} \qquad \textbf{Eq. 2.25}$$

where n_{ads} is the quantity of gas adsorbed at pressure p, n^{m}_{ads} is the quantity of gas needed for the formation of the monolayer and b is a constant. The saturation limit should correspond to a horizontal section of the isotherm in the high pressure region. However, as shown in **Figure 2.11** this is not usual because, in most of the experiments, this region shows a straight positive trend due to the formation of subsequent layers due to the physical adsorption of the probe gas. The monolayer volume may be calculated by extrapolating the linear part of the isotherm to zero pressure, but a more elegant method exists. This is based on the subtraction of the physisorption contribute from the chemisorption isotherm: the total isotherm is measured, then the system is evacuated at the temperature of analysis for a short time, leading to desorption of the physisorbed gas, and finally another isotherm is measured. The difference between the two gives the irreversible adsorption, which is due solely to the contribution of chemisorbed species. The monolayer adsorption is then calculated extrapolating to zero the linear section of the subtracted isotherm.

From the chemisorbed volume, it is possible to obtain the metal dispersion D_M and the average metal particle diameter d_M. To obtain these values, the geometry of the metal particles has to be assumed. Assuming a geometrical shape of the particles:

$$D_M = \frac{N_{(S)M}}{N_{(tot)M}} \qquad \textbf{Eq. 2.26}$$

$$\bar{d}_M = 6\frac{V_M}{a_M}\frac{N_{(tot)M}}{N_{(S)M}} = 6\frac{V_M}{a_M}\frac{1}{D_M} \qquad \textbf{Eq. 2.27}$$

where $N_{(s)M}$ is the number of surface metal atoms, $N_{(tot)M}$ is the total number of metal atoms, 6 is the geometrical factor for spherical particles and a_M is the area of a metal atom. V_M is the volume of a bulk metal atom. It can be calculated from the **Equation 2.28**:

$$V_M = \frac{MW}{\rho N_A} \qquad \textbf{Eq. 2.28}$$

where MW is the atomic weight of the metal and ρ is the density of the metal.

In the present thesis, chemisorption experiments were performed on a Micromeritics ASAP 2020C. The samples (~ 150 mg), placed in a U-shaped quartz reactor, were subjected to preliminary thermo-chemical treatments in order to clean and reduce the sample and finally to fully eliminate the adsorbed hydrogen from the surface of the catalysts. Depending on the sample composition, different chemisorption conditions have been adopted.

The Pd@CeO_2-based materials employed as catalysts for Water Gas Shift Reaction (Chapter 3) have been prepared by cleaning in a flow of O_2(5%)/Ar (40 mL/min) at 250°C for 30 minutes, followed by reduction under H_2(5%)/Ar (40 mL/min) at 100°C for 1 hour and finally evacuated at 250 °C for 8 hours. CO chemisorption experiments were conducted at 35 °C. Whereas on some metal, such as nickel, the adsorbed CO molecule may thermally dissociate on the surface, only molecular adsorption is observed on Pd surface, being completely reversible.[100] Moreover, CO chemisorption has been performed in the low pressure range (1 – 40 torr), to avoid the formation of carbonate species on CeO_2 surface, that would alter the measurement results.[101] The contribution from CO physisorption has been subtracted adopting the double isotherm method: after completing the first chemisorption isotherm, the sample has been rapidly degassed at the analysis temperature and a second isotherm has been recorded. The difference between the two isotherms is extrapolated to zero to obtain the amount of CO chemisorbed on Pd surface.

The Pd@TiO_2-based used as photocatalysts (Chapter 4) have been pre-reduced in a flow of H_2(5%)/Ar (40 mL/min) at 100°C for 30 minutes and subsequently evacuated at 250 °C for 5 hours. H_2 chemisorption experiments have been performed at low

temperature (solid/liquid acetone cooling bath, ~ 180 K) in the pressure range 1 – 400 torr. To obtain the chemisorption contribution of the metal phase alone, it is necessary to halt the spill-over phenomenon, that results in the transfer of activated H atoms to a reducible support (such as CeO_2 or TiO_2). Lowering the temperature, the kinetic of hydrogen diffusion on the oxide surface is very slow, while the adsorption kinetic is almost the same (since the activation energy is almost zero).[99] However, chemisorption at low temperature results in a much greater physisorption contribution. In this case, the chemisorbed hydrogen can be obtained via extrapolation at p = 0 of the linear part of the isotherm measured at 180 K, since the double isotherm method is difficult to be applied because of the difficulty in maintaining constant such low temperature for a long period. Another aspect to be considered is that the palladium is known for its ability in absorb hydrogen, leading to the formation of hydrides. The formation of PdH_X species results in a second stepwise increase in H_2 adsorption, as presented in **Figure 2.12**.

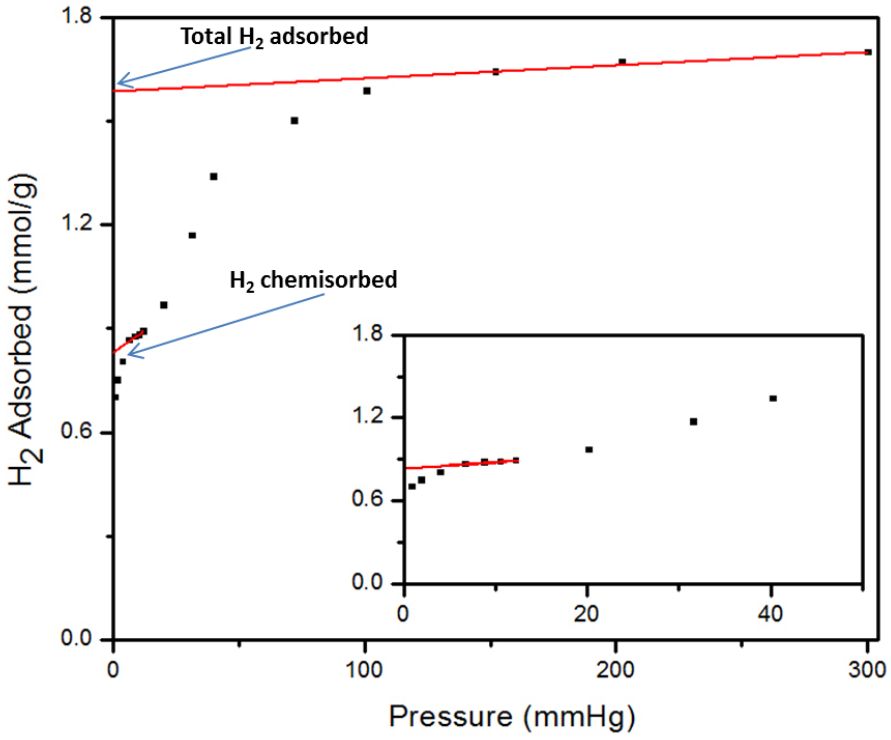

Figure 2.12: Typical chemisorption isotherm.

PdH_X formation depends mainly from temperature and H_2 pressure.[102] As indicated in **Figure 2.12**, the contribution of H chemisorption on the surface of Pd nanoparticles can be determined by extrapolation at p = 0 of the linear part observed in the low pressure range, before the second step due to PdH_X. The extrapolation at p = 0 of

the linear part of the isotherm at high pressure allows to determine the overall H_2 adsorption. Therefore, the amount of H_2 stored in the material as hydrides, as well as the stoichiometry of the PdH_X species, can be obtained from the difference between the two values.

2.7 THERMOGRAVIMETRIC ANALYSIS (TGA)

TGA is one of the most important analytical techniques used to determine important parameters in the samples investigated in this work, such as the amount of functional groups attached on functionalized CNTs surface and the effective content of CNTs within the hybrid nanocomposite materials employed as heterogeneous catalysts. The TGA analysis was particularly important in the determination of the maximum temperature at which the synthesized hybrid materials could be subjected during calcination in order to preserve the CNTs scaffold.

TGA is based on the thermal stability of materials: the change of weight of the substance is monitored as a function of the increasing temperature, with sensitivity in the nanogram range. It can be performed in different environments, optimized according to the experiment needs: an inert atmosphere (nitrogen or argon) is chosen for measuring the content of organic moieties bound to CNTs, which start decomposing at about 350°C; an oxygen atmosphere is instead chosen to evaluate the temperature at which CNTs are removed from the composite and the actual CNTs content. The system sensitivity is given by the precision of the weight balance and of the power supply which provides the temperature ramp of the furnace.

TGA experiments were performed using a TGA Q500 (TA Instruments), with the following procedure: isotherm at 100 °C for 20 minutes (to remove residual solvent), ramp from 100 to 830 °C at 10 °C min^{-1}, under air with a flow rate on the sample of 90 mL min^{-1}.

Chapter 3

CeO_2-BASED CATALYSTS FOR WATER-GAS SHIFT REACTION

The water-gas shift reaction ($CO + H_2O \rightleftharpoons CO_2 + H_2$)[17] is an industrially crucial reaction, used to reduce the levels of CO in the syngas obtained through steam reforming processes.[103] The reaction is particularly appealing as it removes CO while concomitantly producing additional H_2. The reaction is equilibrium-controlled and moderately exothermic, requiring a catalyst to achieve sufficient rates at low working temperatures, where the equilibrium concentration of CO is lower. While high-temperature WGSR (HTS) are favoured by the hot gases generated by the reformer which are exploited by the catalysts, a low-temperature process (LTS) is preferable from a thermodynamic point of view.[60]

3.1 WGSR MECHANISM AND DEACTIVATION

3.1.1 Reaction mechanism for CeO2-based catalysts:

Since neither the metal nor the support alone can achieve the activities of the supported catalyst, a synergistic effect should exist between them. There are two main hypothesis regarding the mechanism of the WGSR over CeO_2-based catalyst: a mechanism based on the formate intermediate and a redox process.

The former (**Figure 3.1**) was proposed by Shido and Iwasawa[104] that examined CeO_2-supported Rh catalysts by temperature-programmed desorption. They concluded that the intermediate for the reaction is a bidentate formate, produced by the reaction of CO with terminal hydroxyl groups on the CeO_2 surface. The rate determining step is the decomposition of the bidentate formate to H_2 and monodentate carbonate. On the other hand, a similar mechanism, based on formate intermediate, was proposed by Jacobs et *al.*[105] that studied Pt/CeO_2 catalysts. They concluded that

the rate determining step is the reduction of the CeO_2 surface for producing the active geminal OH groups.

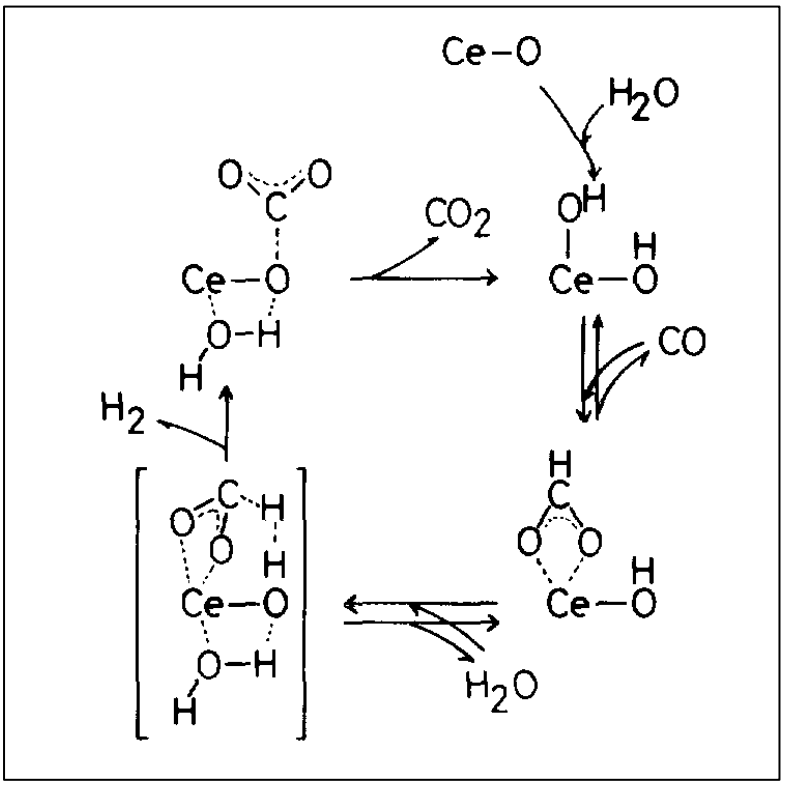

Figure 3.1: Mechanism for the WGSR on metal Rh/CeO_2 catalyst based on the formate intermediate (proposed by Shido et *al.*).[104]

A different mechanism involving a redox process has been proposed by several groups (**Figure 3.2**).[66,106] This mechanism consists on the adsorption of CO on metal sites and its subsequent oxidation by oxygen deriving from CeO_2, which in turn is re-oxidized by H_2O.

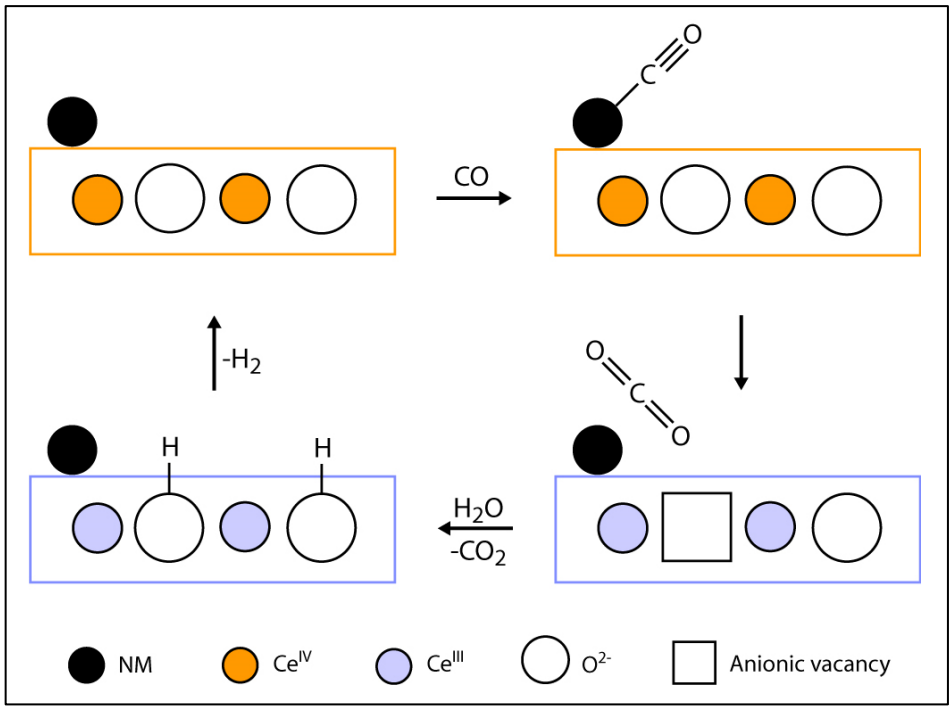

Figure 3.2: Proposed redox mechanism for the WGSR on metal NPs/CeO_2 catalyst.

The redox mechanism has been corroborated by TPR studies[107] demonstrating that CO adsorbed on metals can react with oxygen deriving from CeO_2 and by pulse-reactor studies[108] demonstrating that reduced CeO_2 can be reoxidized by CO_2 and H_2O. Moreover, formates are thermally unstable and therefore WGSR rates should present a maximum at low temperatures. On the contrary, a steady increase in the WGSR rates can be obtained by increasing the temperature. Finally, recent diffuse reflectance infrared Fourier transform spectroscopy (DRIFTS) studies[109] jointly with isotopic analysis studies[110] showed the minor importance of the surface formates in the reaction mechanism as their decomposition rates accounts for at most only 10% of the CO_2 formed.

3.1.2 Deactivation mechanism:

Significant research efforts have been dedicated to understand the deactivation processes affecting Cu-based industrial catalysts. On the contrary, less information is available for the more innovative CeO_2-supported noble metals.

Gorte and co-workers[62,68] associated the deactivation of Pd/CeO_2 catalyst to the decrease of metal dispersion since the they found that the conversion rate increases linearly with increasing the metal surface area. After accelerated aging conditions to investigate which component of the WGS mixture (CO, CO_2, H_2 or H_2O) affected the activity, they found the absence of modifications in the CeO_2, while a dramatic decrease in Pd surface area (measured by CO chemisorption) was observed.

Zalc at *al*.[64] proposed that the deactivation of Pt supported catalysts was due to an irreversible over-reduction of ceria under WGSR conditions interrupting role that it has as co-catalyst of the noble metal.

Many studies[111,99,112,113] associate the deactivation of metal/ceria catalyst to the adsorption suppression induced by electron-transfer effects, such as were originally used to explain strong metal support interaction (SMSI) effects with titania-supported catalysts.[114] SMSI associated with titania is now generally acknowledged to be due to migration of reduced titania over the metal particles.[115] HR-TEM experiments performed on metal/ceria materials[111,99,112,113] were unable to detect decoration or migration effects on ceria that was reduced at moderate temperatures even if this treatment was able to suppress CO or H_2 chemisorption, suggesting that adsorption suppression was associated with an electron-transfer effect. However, the presence of a very thin reduced layer of reduced ceria decorating metal nanoparticles cannot be fully excluded by HRTEM. Indeed, Pan and co-workers recently described HRTEM evidence for partial encapsulation of Pd particles by reduced ceria-zirconia.[116]

A particularly efficient catalyst was reported by Fornasiero et *al*,[117] featuring the Pd and the CeO_2 in a core-shell configuration, where the agglomeration of Pd nanoparticles is prevented by blocking them within the metal oxide shell. For this type of catalytic system, they proposed a mechanism of deactivation involving the reduction of CeO_2 that cause the occlusion of its mesoporous network making the Pd active phase inaccessible (**Figure 3.3**).

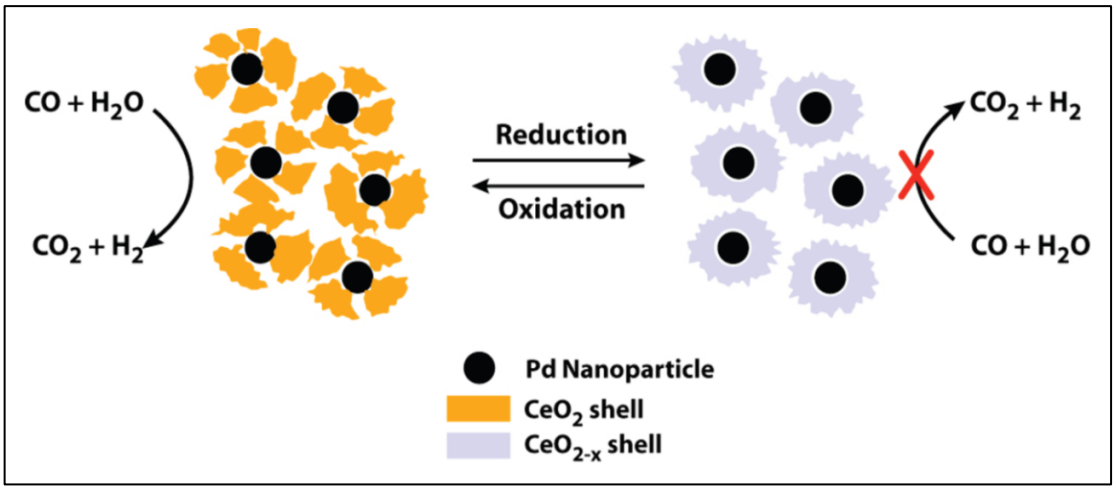

Figure 3.3: Schematic representation of changes in shell morphology for oxidized and reduced Pd@CeO_2 catalyst.

3.2 CATALYST DESIGN

Recently, our research group has designed a successful strategy to prepare hybrid nano-catalysts by covering MWCNTs with an inorganic matrix consisting of metal oxides embedding noble metal nanoparticles.[118] This expedient avoid the sinterization of the metal NPs at high temperatures. In particular, a ternary hybrid comprising MWCNTs, CeO_2 and Pd NPs has proved to be a promising catalyst for the WGSR. In the current thesis, the catalytic system has been revisited, in order to further enhance the activity of the carbon/metal oxide hierarchical nanohybrid catalysts (CNTs/Pd@CeO_2). This objective was pursued by means of a three-way strategy: *i*) preserving the electronic properties of the MWCNTs; *ii*) obtaining high homogeneous nanohybrids by optimizing the coverage of the MWCNTs; *iii*) increasing the inherent activity of the metal oxide/noble metal by performing an opportune crystallization of the inorganic matrix.

In the envisioned synthetic strategy, the nanocarbon building block must act as a scaffold for the layering of the inorganic matrix. Hence, in order to drive covering and secure a firm attachment of Pd@CeO_2 units, the MWCNTs must be adequately equipped with anchoring groups that can bind to the metal centers. We selected benzoic acid as the functional group to be covalently bound to the MWCNTs sidewalls in order to have a functional derivatization. The carboxylic groups on the benzoic acid could then link the metal centers through ligand displacement of the alkoxide ligands. The functionalized

MWCNTs (*f*-MWCNTs) and was obtained via radical addition of the in situ formed diazonium salt of the benzoic acid, adapting a procedure developed by Tour and co-workers.[119,120,121,122] In comparison, the oxidation treatments usually applied on carbon nanomaterials insert additional oxygenated groups, such as epoxides and ketones, that are unusable to anchor metal centers and only cause extra damage to the polyaromatic framework. Hence, the so-called Tour functionalization better preserves the electronic properties of the carbon scaffold and provides at the same time a more homogeneous coverage due to the lack of redundant functional groups. This is expected to drive a more homogeneous coverage with the metal component and result in enhancement of the catalytic performance of the final nanohybrid.

The third point of the improved synthetic protocol concerns crystallization of the metal oxide phase, which is achieved by means of an appropriate thermal treatment. A common step in metal oxide-based heterogeneous catalysts is a high temperature annealing to induce crystallization or to burn the organic ligands used during the preparative procedure. For carbon-based nanostructured catalysts, there is an intrinsic limitation regarding the calcination temperature, as the combustion of the carbon component must be avoided. In the realization of the present catalysts, the careful examination of the thermogravimetric analysis of the as-prepared materials was crucial to establish the maximum temperature tolerated by the MWCNTs. On the other hand the organic ligands, protecting the precursors of the inorganic matrix, are removed at significant lower temperatures. Hence, it is possible to thermally treat fresh CNTs/Pd@CeO_2 achieving the crystallization of the ligands-free inorganic matrix and at the same time preserving the nanotubes' structure.

3.3 CATALYST PREPARATION

The CeO_2-based materials employed as catalysts for the WGSR were assembled starting from three building blocks: *i*) benzoic acid-functionalized MWCNTs (*f*-MWCNTs); *ii*) palladium nanoparticles protected by mercapto-undecanoic acid (Pd-MUA); *iii*) cerium (IV) decyloxide ($Ce(ODe)_4$). The building blocks of the organic/inorganic nanohybrid catalysts were prepared separately and then assembled to obtain the final material. The overall process can be summarized in three steps. The first step consists in the covalent functionalization of MWCNTs (**Figure 3.4 A**). Subsequently

a monolayer of $Ce(ODe)_4$ is self-assembled around preformed Pd-MUA in a core-shell configuration (**Figure 3.4 B**).[123] The assembly of the organic/inorganic nanohybrid is obtained (**Figure 3.4 C**) by mixing *f*-MWCNTs and Pd-MUA@$Ce(ODe)_4$ under sonication regime: a ligand exchange occurs between the alkoxide and the benzoic acid groups providing initial layering of the inorganic matrix to the *f*-MWCNTs sidewalls. A slow hydrolysis is a crucial step to obtain the growth of the oxide layers around the nanocarbon scaffold, that acts as monodimensional templating agent. This results in the coating of the *f*-MWCNTs by a gel precursor of the inorganic matrix. The as-prepared fresh materials are finally calcined under air.

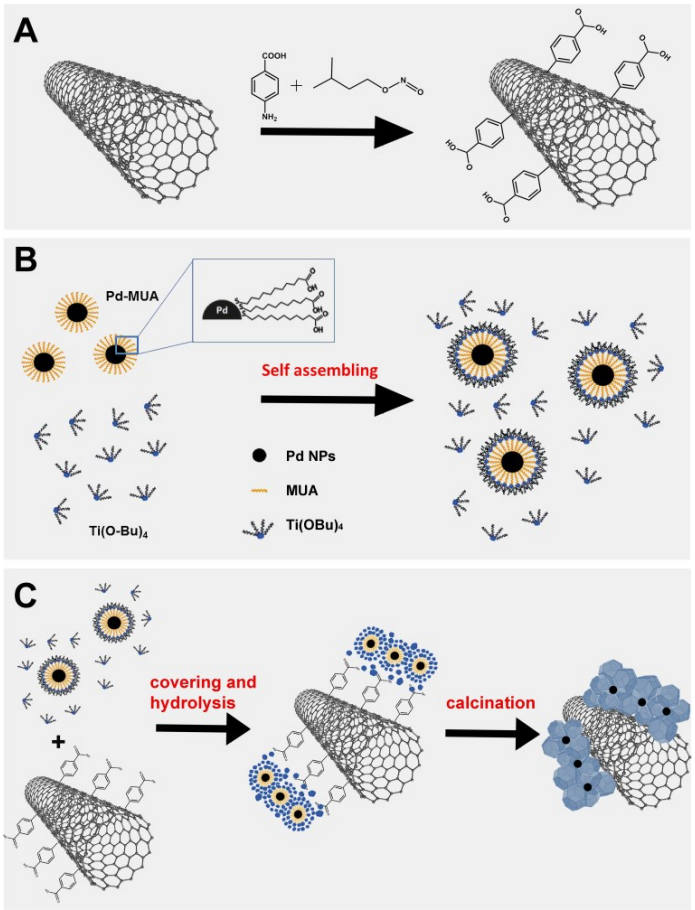

Figure 3.4: General synthetic scheme of hierarchical CNTs/Pd@CeO_2. A) Covalent functionalization of the MWCNTs with benzoic acid; B) Self-assembly of the Pd@CeO_2 precursor; C) hydrolysis to obtain the final hybrid, fresh and calcined.

The composition of the hybrid materials was varied by changing the relatives amounts of *f*-MWCNT and $Ce(ODe)_4$, while the nominal amount of Pd remains fixed at 1.5% wt. Materials with three different nominal compositions have been prepared and labelled as follows: **10-CNTs/Pd@CeO_2**, **20-CNTs/Pd@CeO_2** and **30-**

CNTs/Pd@CeO_2, respectively with 10, 20 and 30 nominal % wt of MWCNTs. An appropriate suffix indicates the thermal treatment (at 250 °C) undergone by the material (e.g. **20-CNTs/Pd@CeO_2-250**).

3.3.1 Covalent functionalization of MWCNTs with *p*-benzoic acid (*f*-MWCNTs)

Pristine multi-walled carbon nanotubes with 20-30 nm diameter and 0.5-2 μm length were supplied by Nanoamor. In a typical synthesis, 150 mg of Pristine MWCNTs were dispersed in 150 mL of H_2O by sonication in an ultrasonic bath for 20 minutes. Then 514 mg of *p*-amino-benzoic acid (0.3 equivalents relative to the carbon moles of the nanotube) were added and the mixture further sonicated for 10 minutes. The system was then transfer in an oil bath and kept under magnetic stirring while 2.25 mL of isopentyl nitrite were added. The reaction mixture was heated at 80 °C for 6 hours under stirring. After this time, the mixture was cooled to room temperature, filtered through 0.1 μm PTFE Millipore membrane and washed successively with DMF, MeOH, H_2O, EtOH and Et_2O (each washing was carried out with 5 min of sonication of the solid in the specific solvent). Finally, the solid was dried overnight at 80 °C.

3.3.2 Synthesis and functionalization of palladium nanoparticles with mecapto-undecanoic acid (Pd-MUA)

Pd-MUA were prepared adapting a procedure previously reported.[124] The Pd precursor is reduced in the presence of 11-mercaptoundecanoic acid (MUA), which binds to the growing metal nanoparticle (nominally 2 nm) forming a three dimensional SAM. In a typical synthesis, 23.40 mg of K_2PdCl_4 were dissolved in 2.4 mL of Milli-Q water and kept under magnetically stirring. Then, 12 mL of acetone, 0.248 mL of H_3PO_4 and 7.70 mg of mercapto-undecanoic acid (MUA) were added sequentially and the mixture stirred for 5 minutes. Afterward, a freshly prepared aqueous solution (1 mL) of $NaBH_4$ (30 mg/mL,) is rapidly added in one portion, causing the solution to turn immediately black, and the mixture stirred for 20 minutes. After that, the acetone was evaporated at 20 °C and 110 mbar and the remaining mother liquor eliminated by centrifugation. The particles were washed three times with H_2O by sonication and centrifugation after each washing cycle. Finally the Pd-MUA were recovered by dissolution in THF, obtaining a final concentration of 0.3 mg Pd/mL.

3.3.3 Synthesis of cerium (IV) tetrakis(decyloxide) ($Ce(ODe)_4$)

$Ce(ODe)_4$ were prepared adapting a procedure previous reported.[123] In a typical synthesis cerium ammonium nitrate (CAN) (5.00 g, 9.12 mmol) was dissolved in 50 mL of MeOH, after which 1-decanol (6.97 mL, 4 eq vs Ce) was added. Next, a 25 wt % solution of NaMeO in MeOH (12.51 mL, 6 eq vs Ce) was introduced dropwise, causing formation of gaseous NH_3 and precipitation of a bright yellow solid (cerium(IV) methoxide) and a white solid ($NaNO_3$). The mixture was stirred for 1 h, before removing the solvent by evaporation to yield an orange-colored oil with $NaNO_3$ powder mixed in. The oil was dissolved into 25 mL aliquots of dichloromethane, and the solvent was evaporated again. This procedure was repeated twice. Finally, the compound was dissolved in DCM, the $NaNO_3$ was filtered out, and the solvent was removed by evaporation. The orange-oil product (7.00 g, 99%) was dissolved in THF, resulting in a final concentration of 43.6 mg CeO_2/mL.

3.3.4 Hybrid assembly (CNTs/Pd@CeO_2)

100 mg of **10-CNTs/Pd@CeO_2-250**, **20-CNTs/Pd@CeO_2-250** or **30-CNTs/Pd@CeO_2-250** were prepared employing respectively 10, 20 and 30 mg of *f*-MWCNTs dispersed in absolute ethanol (EtOH mL/ *f*-MWCNTs mg ratio equal to 2) by sonication in an ultrasonic bath for 30 minutes. Meanwhile, a fresh Pd-MUA solution in THF (0.3 mg Pd/mL) containing 1.5 mg of Pd was slowly added under magnetically stirring respectively to 2.03, 1.80 and 1.57 mL of THF solution of $Ce(ODe)_4$ (43.6 mg CeO_2/mL). Then, the fresh Pd-MUA@$Ce(ODe)_4$ solution was slowly added under sonication to the *f*-MWCNTs dispersion and the mixture further sonicated for 30 minutes. Finally a 10% solution H_2O in EtOH ($Ce(ODe)_4/H_2O$ molar ratio equal to 1/120) was slowly dropped under sonication into the mixture that was then further sonicated for 30 minutes. The obtained materials were collected by filtration through a 0.45 μm PTFE Millipore membrane, washed with ethanol twice (5 min of sonication of the solid in the solvent) and subsequently dried overnight at 80 °C. The fresh materials were finally subjected to calcination at 250 °C for 5 hours (+3 °C/min; -4.5 °C/min).

A portion of the **30-CNTs/Pd@CeO_2** material was subjected to calcination at 350 °C for 5 h (+3 °C/min; -4.5 °C/min) with the purpose of fully remove the carbonaceous scaffold (see paragraph 3.4.1) and labelled **30-CNTs/Pd@CeO_2-350**.

3.4 RESULTS AND DISCUSSION

The materials presented in this chapter were characterized through a combination of several techniques to corroborate the correct assembly of the organic/inorganic nanohybrid. Composition, morphology, structure and textural properties were analyzed before catalytic tests

3.4.1 Thermogravimetric analysis

The prepared materials was firstly analyzed by thermogravimetric analysis (TGA) under air flow (**Figure 3.5**) to determine the more adequate calcination temperature. Hence, a weight loss of about 4.5% in the range 350-450 °C is observed for the functionalized CNTs, attributed to the combustion of benzoic acid groups introduced on the sidewall of the nanotubes, and that is not present in the pristine CNTs. On the other hand, TGA of the fresh carbon/inorganic hybrids present two weight losses, the first at 150 - 200 °C and the second at 300 - 400 °C. The former can be related to the combustion/removal of organic ligands residues of the sol-gel synthesis (i.e. MUA and decanol) and H_2O trapped in CeO_2. The weight loss at higher temperature is related to the full removal of the carbonaceous scaffold. It is noteworthy that the presence of a strong oxidizing agent (CeO_2) significantly decreases the combustion temperature of the MWCNTs at 300 - 450 °C, indicating an intimate contact between the nanocarbon structures and the inorganic matrix. Indeed the **Pristine-MWCNTs** starts to burn at 500 °C, according to the litterature.[125]

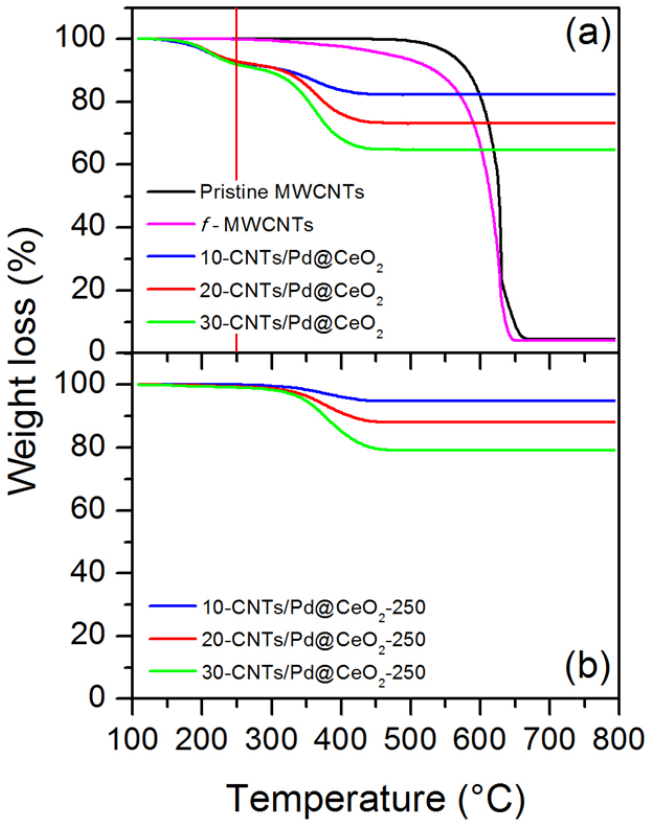

Figure 3.5: Thermogravimetric analysis of the samples after drying (a) and of the samples after calcination at 250 °C in air (b). The red vertical line indicates the calcination temperature (250 °C) of the fresh materials.

On the basis of these evidences, the calcination temperature of the fresh nanohybrids was set at 250 °C to preserve the carbon skeleton and removing, at the same time, the residual ligands. The composition of the final calcined hybrids can therefore be determined by the loss in weight at 300 - 400 °C, that matches with the complete removal of the MWCNTs. The actual MWCNTs % wt for **10-CNTs/Pd@CeO$_2$-250**, **20-CNTs/Pd@CeO$_2$-250** or **30-CNTs/Pd@CeO$_2$-250** are 6.0%, 11.7% and 21.0% respectively.

In contrast, by increasing the calcination temperature to 350 °C, no significant weight loss is observed at the TGA profiles, indicating that at this temperature the MWCNTs have been completely burned off. Such material, **30-CNTs/Pd@CeO$_2$-350**, was used as a term of comparison to evaluate the electronic role of the MWCNTs in the WGSR (see paragraph 3.4.6).

3.4.2 Structural analysis

Raman spectra were collected at each stage of the synthesis to analyze the structure of the prepared nanohybrids and to investigate the properties of the different phases. **Figure 3.6** displays the spectra at each step of the synthesis of **20-CNTs/Pd@CeO$_2$-250** as representative example. All the samples analyzed show the characteristic bands of the CNTs: the disorder-induced D band (~ 1300 cm^{-1}) with its first (~ 1600 cm^{-1}, D′ band) and second-order related harmonics (~ 2300 cm^{-1}, 2D band) and the graphitic G band (~ 1590 cm^{-1}), due to the in-plane vibrational mode of the sp^2 framework.[126,127]

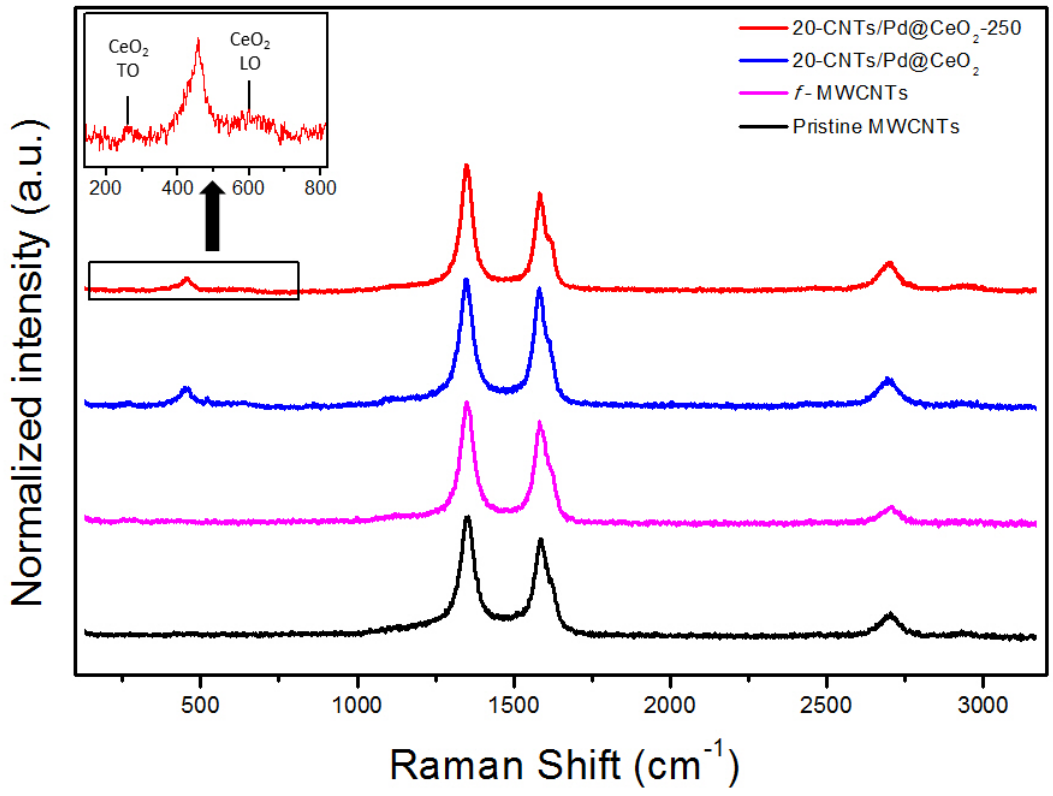

Figure 3.6: Raman spectra of **Pristine-MWCNTs**, ***f*-MWCNTs**, **20-CNTs/Pd@CeO$_2$** and **20-CNTs/Pd@CeO$_2$-250**. In the inset, the expansion of the Raman bands showing three characteristic peaks of the CeO$_2$.

To corroborate the TGA data, an evidence of the functionalization can be found in the fine comparison of the **Pristine-MWCNTs** and the ***f*-MWCNTs**: the ratio between the D band and the G band (I_D/I_G) slightly increases, from 1.25 to 1.27. As the intensity ratio of these two bands has been used as a semi-quantitative parameter to assess the degree of introduced defects, in the present case it indirectly indicates that a higher

disruption of the π-extended frameworks caused by the covalent functionalization has occurred.[128,129] Furthermore, the I_D/I_G ratio in the hybrids appear diminished at 1.12 in the fresh material and dramatically increased at 1.34 after the thermal treatment. The apparently heal of the π framework of the MWCNTs can be explained as a perturbation of the signal of the G band given by metal oxide layers, resulting in a decrease of the I_D/I_G ratio.[130] On the other hand the calcination introduce extra damage into the carbonaceous skeleton, resulting in an increase of the ratio.

After the coverage with the inorganic matrix, both the fresh and the calcined samples present a band at 455 cm^{-1} related to CeO_2. In the case of the calcined sample the breadth and the asymmetry of the band result more pronounced, indicating a higher degree of crystallization and suggesting a small size of the nanostructure CeO_2 particles. In agreement with the literature,[131] the nanoscale nature of the particles is corroborated by the band shift at lower energy than that found in a typical CeO_2 crystallite (464 cm^{-1}). A magnification in the 200-800 cm^{-1} range evidences other two broad and barely visible characteristic bands of the CeO_2 structure: the non-degenerative LO mode (595 cm^{-1}) and the doubly degenerate TO mode (272 cm^{-1}),[132] which results shifted to lower energy (265 cm^{-1}).

Powder XRD patterns of the calcined samples presented in **Figure 3.7** show the reflections related to the cubic structure of CeO_2 that clearly appear nanostructured because of the broadening of the reflections. The nanoscale behavior of the structure is confirmed by the mean crystallite size of CeO_2, calculated by applying the Scherrer's equation (**Eq. 2.7**) to the main reflection (111). The calculation results in an average crystallite size of 4.1, 4.0 and 3.8 nm for the **10-CNTs/Pd@CeO_2-250**, **20-CNTs/Pd@CeO_2-250** and **30-CNTs/Pd@CeO_2-250** samples respectively. Notably, no reflection can be related to Pd nanoparticles, reasonably because of the low loading and the small average size of the nanoparticles, as observed by HR-TEM (see paragraph 3.4.3). Moreover a shoulder, with maximum at 26 °, can be related to the graphitic main reflection (26.6 °)[133] of the MWCNTs; the shoulder is more evident in the sample containing the higher amount of MWCNTs.

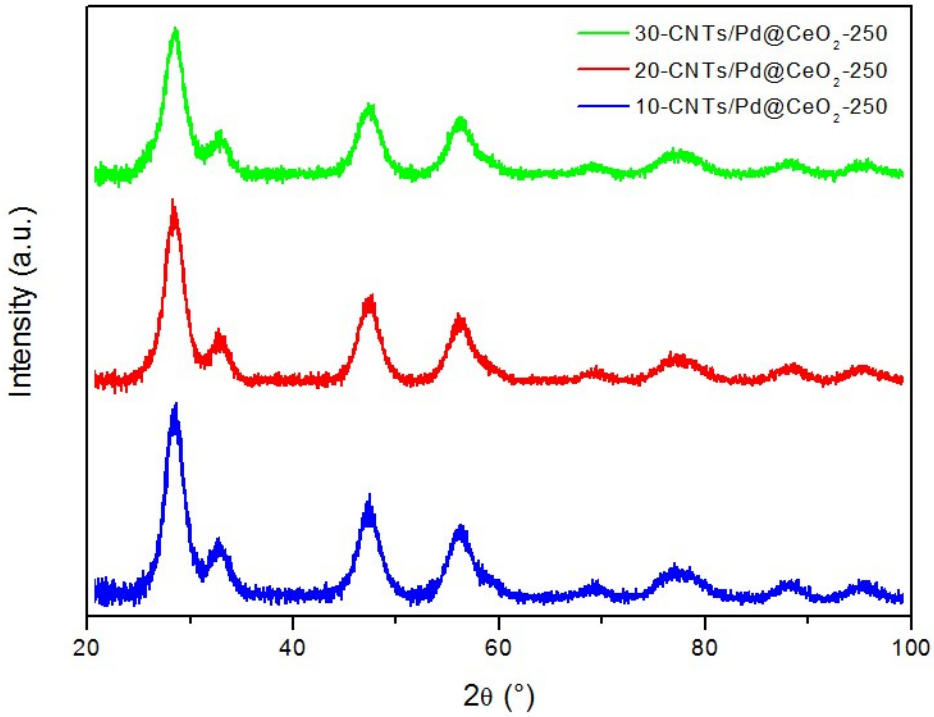

Figure 3.7: Powder XRD patterns of the samples calcined in air at 250 °C.

3.4.3 Morphological analysis

Transmission electron micrographs (TEM analysis) confirm the successful hierarchical assembly of the hybrid and the intimate contact between the components. A CeO_2 layer homogeneously wraps the MWCNTs in samples **10-CNTs/Pd@CeO₂-250** and **20-CNTs/Pd@CeO₂-250** while only partial coverage was observed in sample **30-CNTs/Pd@CeO₂-250**. A statistical investigation (50 structure per sample) reveals that there is no significantly difference among the three samples in terms of CeO_2 layer average thickness, which results equal to 6 nm (**Figure 3.8**). Therefore it is reasonable to hypothesize that the MWCNTs functionalized surface is saturated by a certain amount of Pd@CeO_2 and a further grow is hindered. The extra inorganic matrix can be observed in the TEM images as free standing material, particularly for **10-CNTs/Pd@CeO₂-250**, which has the lower carbon/inorganic ratio. It is important to note that in the case of the **30-CNTs/Pd@CeO₂-250** material, no free standing inorganic matrix was observed because the large excess of carbonaceous component, which is not saturated by the amount of used inorganic matrix. It is clear that an optimum carbon/inorganic ratio exists, given no free-standing elements.

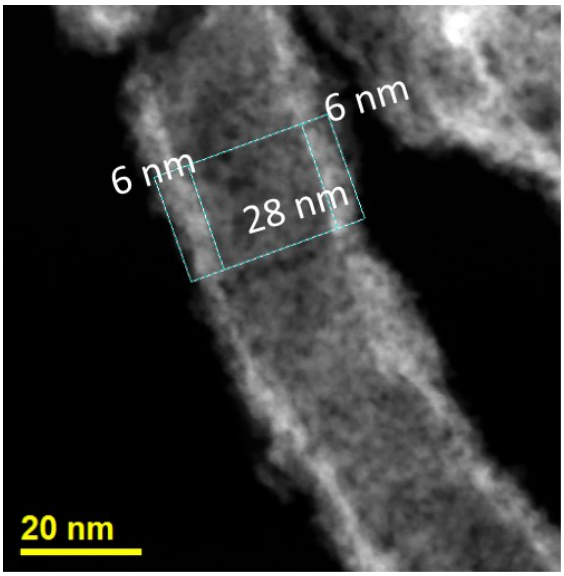

Figure 3.8: Representative HAADF-STEM of the **20-CNTs/Pd@CeO_2-250** sample showing the MWCNT and the CeO_2 layer thickness.

HR-TEM micrographs and Fast Fourier Transform (FFT) of a selected area (SAED) analysis reveal an amorphous CeO_2 layer covering the MWCNTs in the fresh materials while the calcined materials are visibly nanocrystalline (**Figure 3.9**). A careful analysis of the images indicate a mean crystallite size of 4 nm, in agreement with the XRD results.

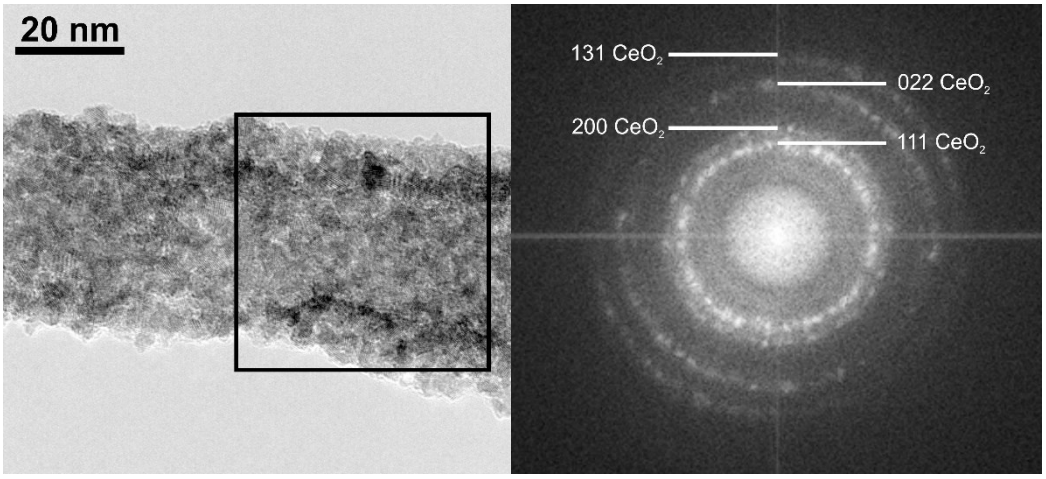

Figure 3.9: Representative HR-TEM (left) and FFT pattern (right) of the **10-CNTs/Pd@CeO_2-250** sample showing the crystalline CeO_2 shell around the MWCNT.

Elemental mapping by energy filtered transmission electron microscopy (EFTEM) further confirms that most of the inorganic matrix is located around the carbonaceous scaffold (**Figure 3.10**). Moreover, it can be appreciated how the MWCNTs

poor sample (**10-CNTs/Pd@CeO_2-250**) bears a significant amount of free-standing CeO_2, which becomes less present as the MWCNTs content increases (**20-CNTs/Pd@CeO_2-250**) and totally disappears in the **30-CNTs/Pd@CeO_2-250** material. Evidently the optimum carbon/inorganic ratio to guarantee homogeneous coating and avoid formation of stand-standing Pd@CeO_2 is close to 20 % wt of MWCNTs. Notably, the Pd nanoparticles incorporated inside the CeO_2 layer have been not detected in any TEM micrograph. The causes of this absence can be ascribed to three factors: *i*) the small size of the NPs (averagely 2 nm);[124] *ii*) the low loading (nominally 1.5 % wt); *iii*) the efficient shielding by the high electron density of the CeO_2 layer, as a consequence of the core-shell configuration.

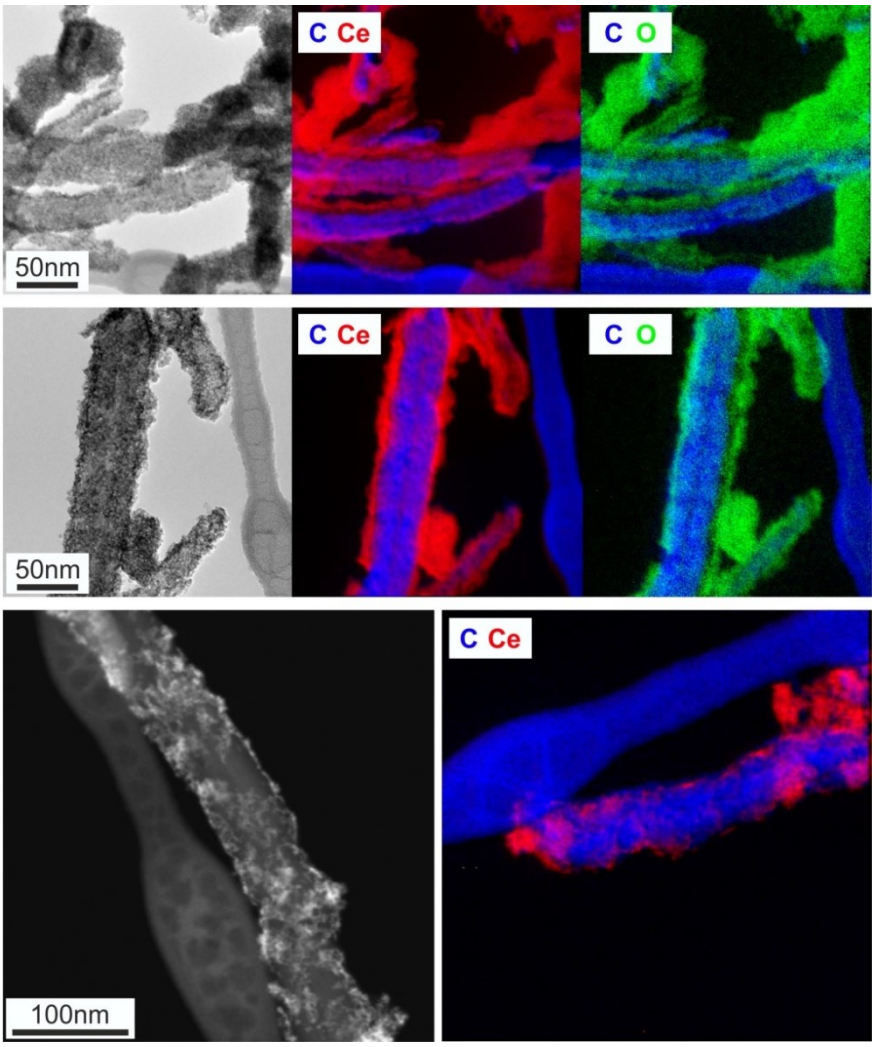

Figure 3.10: Representative HR-TEM, HAADF-STEM and EFTEM maps of the catalysts (from top to bottom **10-CNTs/Pd@CeO_2-250**, **20-CNTs/Pd@CeO_2-250** and **30-CNTs/Pd@CeO_2-250**). Note that in the EFTEM images, also the carbon grid is visible and should not be confused with the MWCNTs.

3.4.4 Textural analysis

N_2 physisorption at liquid nitrogen temperature has been used to explore the textural properties (**Figure 3.11** and **Table 3.1**) of the hybrids at each step of the synthesis. According to the IUPAC recommendations,[94] all the samples exhibit Type IV isotherm typical of mesoporous materials.

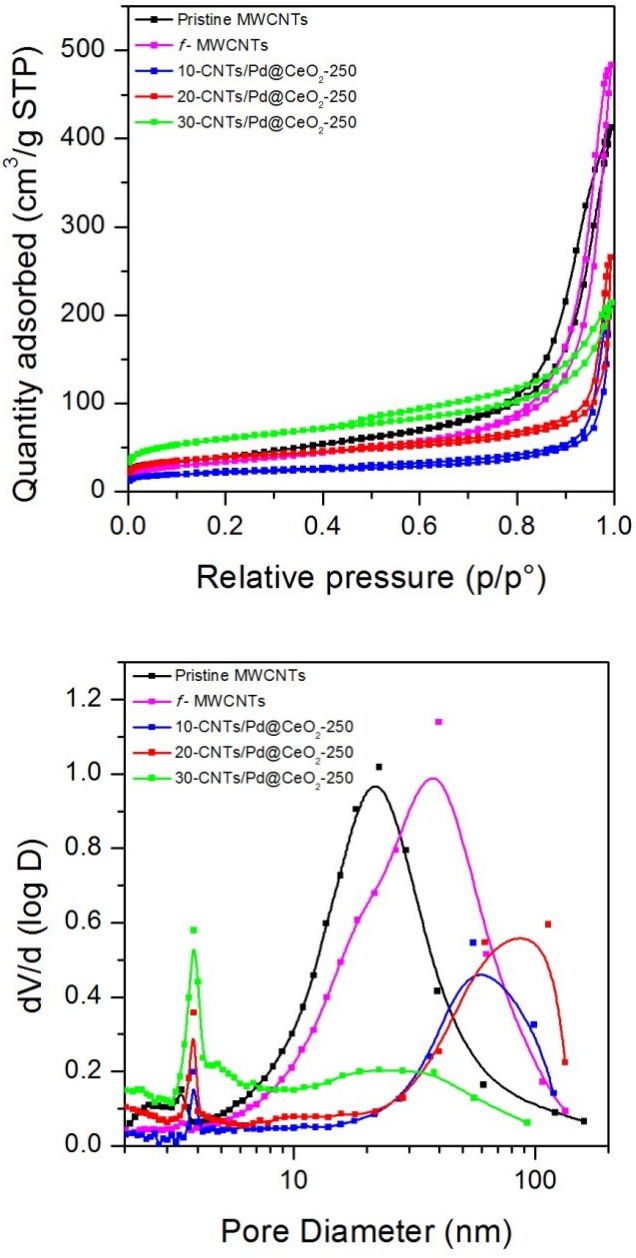

Figure 3.11: N_2 physisorption isotherms (top) and BJH pore size distribution (bottom) of the materials.

The **Pristine MWCNTs** have a high surface and cumulative pore volume while the pore size distribution shows a bimodal distribution. The two relative maxima at 22 and 3 nm are due respectively by interstitial spaces in bundles of MWCNTs (observed by TEM) and surface cavities caused by defective sites.[134] The covalent functionalization of the sidewalls of the MWCNTs slightly decreases the surface area and increases the pore volume and the maximum of the pore size distribution, as a consequence of the unbundling process caused by covalent functionalization.[135] The resulting material is less aggregated and presents larger interstitial spaces. On the other hand the contribution of mesopores smaller than 5 nm is strongly reduced, possibly by the occlusion of surface cavities due to reaction and oligomerization of Ph-COOH groups on the defects of the **Pristine MWCNTs**.[122]

Table 3.1: Summary of the textural properties and the result of the chemisorption measurements of the investigated materials.

Sample	Pristine-MWCNTs	*f*-MWCNTs	10%-CNTs	20%-CNTs	30%-CNTs
SSA[1] (m^2/g)	142	117	64	118	186
CPV[2] (mL/g)	0.634	0.741	0.306	0.382	0.305
MV[3] (mL/g)	0	0.002	0.014	0.032	0.043
ESA[4] (m^2/g)	143	115	41	65	117
D_{max}[5] (nm)	3.4 / 22	37	3.9 / 59	3.8 / 87	3.9 / 24
MSA[6] (m^2/g)	-	-	0.527	0.616	0.794

[1]Specific Surface Area calculated from the BET analysis of the isotherms;

[2]Cumulative Pore Volume calculated from the BJH analysis of the desorption branch of the isotherms;

[3]Micropore volume calculated from the t-plot analysis of the isotherms;

[4]External Surface Area calculated from the t-plot analysis of the isotherms;

[5]Relative maxima of the pore size distributions obtained by the BJH analysis of the desorption branch of the isotherms;

[6]Metal Surface Area determined by CO chemisorption.

The textural properties of the materials significantly change after the hybridization of the carbonaceous skeleton with the inorganic matrix and the subsequent calcination at 250 °C. The hybridized materials present an appreciable contribution of micropores that is clearly related with the inorganic Pd@CeO_2 matrix calcined at low temperature. By increasing the carbon/inorganic ratio, the surface area and the micropore volume increase. This trend could be due to the sintering ability of the free-standing Pd@CeO_2 fraction, that is higher in the carbon poorest sample. Regarding the cumulative pore volume trend, it well fits with the pore size distribution of the samples and is maximum for **20-CNTs/Pd@CeO_2-250**. The three calcined materials present a bimodal pore size distribution, with the first relative maximum around 4 nm and the second in the range 25 – 90 nm. The first contribution and the rest of the micropores should be related with the Pd@CeO_2, that is better organized as the MWCNTs content increases while the larger mesopores are due to the bundling of the hybridized MWCNTs. The **20-CNTs/Pd@CeO_2-250** material, presenting the optimal coverage, has the higher cumulative pore volume as result of larger interstitial spaces between the covered tubes. On the other hand, the uncovered portion of MWCNTs in the **30-CNTs/Pd@CeO_2-250** increases the bundling and results in smaller interstitial spaces and a lower cumulative pore volume.

3.4.5 Chemisorption measurements

The accessibility of the Pd nanoparticles surface in the calcined hybrids has been evaluated by CO chemisorption measurements and the result are summarized in **Table 3.1**. The exposed surface areas obtained are rather low and significantly lower than those reported in previous works for Pd@CeO_2 supported in silanized Al_2O_3.[136,137] This behavior is reasonably related with the higher CeO_2/Pd ratio employed in the present work, necessary to completely cover the MWCNTs. For the presented materials the metal surface area increase as the carbon/inorganic ratio increases, as result of a lower contribution of mesopores in the CeO_2 layer.

3.4.6 Catalytic results

The activity of the calcined hybrids for the WGSR has been evaluated in terms of rates of CO conversion normalized by Pd moles (considering the nominal amount of Pd, i.e. 1.5% wt) at different temperatures, increased step-wise from 200 to 350 °C (**Figure 3.12**). In order to assess the stability of the materials, each temperature was maintained for 6 h (for more details, see the paragraph 2.1.1). In all cases, the CO conversion agrees with the H_2 and CO_2 yields.

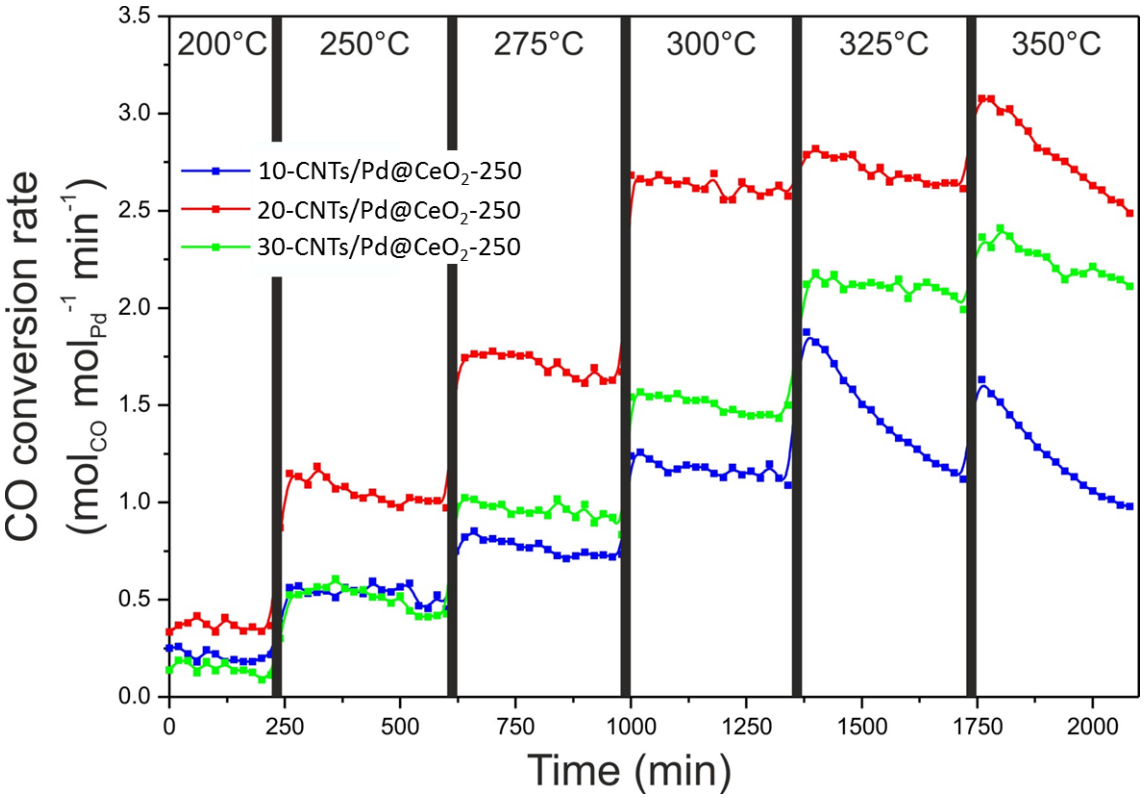

Figure 3.12: Rate of CO conversion at different temperatures for the catalyst calcined at 250 °C (total gas flow rate = 48.5 mL min^{-1}; GHSV = 75000 mL g^{-1} h^{-1}; WGSR reaction mixture: 3.0 vol. % CO and 3.0 vol. % H_2O diluted in Ar).

Notably, the activities of the presented materials are considerably higher than those previously reported for hybrid materials not subjected to thermal treatments.[118] Reasonably, this must be related to the crystallization of the metal oxide shell and the removal of organic ligands employed during the sol-gel synthesis, resulting in the formation of micro/mesopores and an increased accessibility of the metallic active phase (i.e. Pd NPs). The best catalytic performance, evaluated as a combination of CO conversion rates and stability of the catalyst under catalytic conditions, was found with

sample **20-CNTs/Pd@CeO_2-250**. The CO conversion for this sample is around 70% at 300°C. In comparison, both **10-CNTs/Pd@CeO_2-250** and **30-CNTs/Pd@CeO_2-250** samples present a lower but still decent activity. The turn-over frequency (TOF) values were calculated at 300 °C considering the exposed Pd surface area (calculated from CO chemisorption) and correspond to 1519, 2896 and 1300 min^{-1} for **10-CNTs/Pd@CeO_2-250**, **20-CNTs/Pd@CeO_2-250** and **30-CNTs/Pd@CeO_2-250** samples, respectively. These results are in agreement with the textural data and with the hypothesis that the optimum carbon/inorganic ratio corresponds to 20% wt of carbon component. Indeed, smaller amounts (10% wt) are not enough to support all the Pd@CeO_2, which in part forms free-standing aggregates. In such free-standing inorganic matrix, the accessibility of the Pd is limited because of an increased sintering of the microspores, as reflected by the chemisorption measurements of the Pd surface area and by N_2 physisorption pore distribution analysis. On the other hand, higher amounts of carbon component (30% wt) produce structures with MWCNTs not completely covered, resulting in a lower CO conversion.

Regarding the stability of the materials, all the catalysts exhibit in general good stability for at least 6 hours (the set time of each temperature for the experiments) up to 300°C. At higher temperatures, deactivation processes started to be observed and follow different trends for the different carbon/inorganic ratios. The most pronounced deactivation is observed in the poorest carbon sample **10-CNTs/Pd@CeO_2-250** while the **30-CNTs/Pd@CeO_2-250** exhibits the best performance in terms of stability. These results corroborate the fact that the MWCNTs play a key role in the catalytic stability of the hybrid material and strongly suggest that the deactivation pathway mainly occurs at free standing Pd@CeO_2, that are not in contact with the carbonaceous scaffold. Indeed, free standing Pd@CeO_2 is more abundant in sample **10-CNTs/Pd@CeO_2-250** and is not present at all in catalyst **30-CNTs/Pd@CeO_2-250**.

The morphological characterization reveals that MWCNTs can act as scaffold driving an optimal tri-dimensional arrangement of the Pd@CO_2 around the carbonaceous scaffold: this behavior is related to the activity of the materials because the stabilization of the Pd@CO_2 avoids their aggregation and keeps accessible the active phase. Beyond this, it can be hypothesized that there is an additional positive effect due to the metallic behavior in terms of conductivity of the MWCNTs, which disfavors possible electronic deactivation pathways caused by formation of over-reduced CeO_2 [64] (see paragraph 3.1).

The cause of the different stability behavior by changing the carbon/inorganic ratio was investigated by characterization of the materials recovered after the catalytic test presented in **Figure 3.12**. The textural and the structural properties, analyzed by N_2 physisorption and powder XRD, reveal only marginal modifications of the materials after the aging under WGSR conditions, with the CeO_2 crystallite mean size only slightly increasing from 3.8-4.1 to 4.2-4.6 nm. On the other hand, CO chemisorption measurements of the samples subjected to WGSR showed a decrease of the Pd metal surface area, resulting in a decrease of 70%, 53% and 5% for **10-CNTs/Pd@CeO_2-250**, **20-CNTs/Pd@CeO_2-250** and **30-CNTs/Pd@CeO_2-250** samples respectively. Considering that the core-shell arrangement of the inorganic matrix has been designed to avoid sintering of the metal phase at high temperatures,[136] the most reasonable hypothesis to explain the minor accessibility of the active phase is the reduction of CeO_2 which suppress the chemisorption of CO by electron-transfer effects. This effect is described in the literature as strong metal support interaction (SMSI) effect[111,99,112,113] (see paragraph 3.1.2). Furthermore the reduction of CeO_2 is reported to cause the occlusion of its mesoporous network making the Pd active phase inaccessible.[117]

As the diminution of the Pd metal accessibility decreases for major carbon/inorganic ratios, it is reasonable to attribute to the MWCNTs component a role of stabilizing agent (besides its established role as templating agent) of the inorganic matrix, by disfavoring the deactivation mechanism of the Pd@CeO_2, due to its electronic interaction with the inorganic components.

To further corroborate the role of the MWCNTs component in the stability of the hybrid catalyst, the **30-CNTs/Pd@CeO_2-350** material, namely the material subjected to higher calcination temperature that mostly remove the carbon scaffold, was tested in the WGSR at 250 °C (**Figure 3.13**).

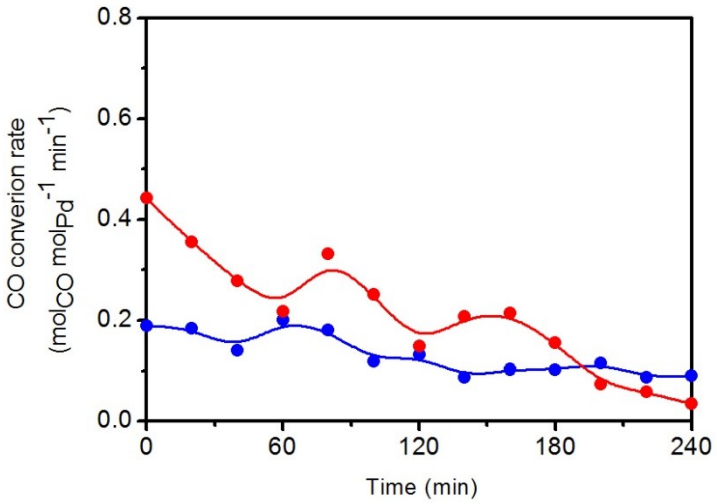

Figure 3.13: Rate of CO conversion at 250 °C for temperatures for **30-CNTs/Pd@CeO₂-250** (blue spots) and **30-CNTs/Pd@CeO₂-350** (red spots).

Its CO conversion results, at the beginning, higher than its analogous material **30-CNTs/Pd@CeO₂-250**. This behavior can be related to its higher nominal Pd loading (2.2 %), due to the completely removal of the carbon component (confirmed by TGA analysis **Figure 3.5**), and its higher degree of crystallization, due to calcination at 350 °C. However, the absence of the MWCNTs component cause a rapid deactivation despite the relatively low temperature, confirming the role of the MWCNTs as stabilizing support.

The HR-TEM micrographs (**Figure 3.14**) show that the structure of this material is recalling the form of the templating MWCNTs.

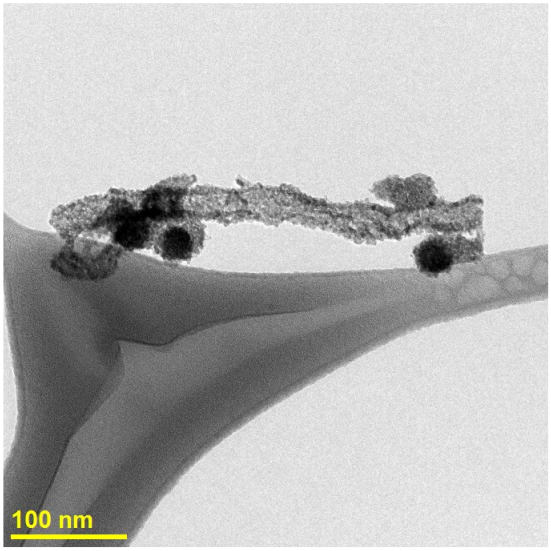

Figure 3.14: Representative HR-TEM of the 3**0-CNTs/Pd@CeO$_2$-350** sample showing the tubular form of the Pd@CeO$_2$ remained after completed removal of the MWCNTs

3.5 CONCLUSSIONS

In conclusion, the materials presented in this chapter have shown the designed hierarchical assembly: an intimate contact between the nanocarbon structure and the inorganic matrix evince from most of the analysis. The morphological characterization evinces that the MWCNTs are saturated by a certain amount of Pd@CeO$_2$ and the extra inorganic material stays as free-standing.

WGSR tests have shown that integration of MWCNTs into core-shell Pd@CeO$_2$ catalysts have a positive impact in terms of activity and stability. The MWCNTs component has an important role as stabilizing agent by disfavoring the electronic deactivation mechanism of the inorganic matrix. Indeed the hybrid catalyst with the optimum carbon/inorganic ratio, which present a homogeneous coverage and the absence of free-standing inorganic material, shows best performances in terms of activity and stability.

Post-synthetic removal of the MWCNTs results in a tubular arrangement of the Pd@CeO$_2$ systems, that to some extent retain the benefits introduced by the MWCNTs. However the catalytic stability of this material result dramatically decreased compared to its MWCNTs-containing analogue. This finding confirms the stabilizing role of the MWCNTs.

Chapter 4

TiO_2-BASED CATALYSTS FOR PHOTOCATALYTIC HYDROGEN EVOLUTION

4.1 MECHANISM AND DEACTIVATION OF THE HYDROGEN PRODUCTION VIA PHOTOREFORMING OF ALCOHOLS

The reaction producing H_2 through the process of alcohol photoreforming implies the reduction of H^+ by the photogenerated electrons on the surface of the photocatalyst following irradiation with light of an appropriate wavelength (**Eq. 4.1**), leaving a charged hole in the valence band (VB). The photoexcited electrons that have moved into the conduction band (CB) of the semiconducting photocatalysts (TiO_2 in this work) migrate to the surface of the semiconductor and have the required energy to perform reduction of protons to hydrogen.

$$2H_{(ads)}^{+} + 2e^{-} \rightarrow H_2 \qquad \textbf{Eq. 4.1}$$

Several strategies are adopted to extend the lifetime of the photogenerated charge carriers, which is otherwise limited by the generally fast electron/hole recombination. Among several strategies, combination of the semiconductors with (noble) metal nanoparticles has been particularly exploited, due to the ability of such nanoparticles to act as trapping sites for the photoexcited electrons.[138,47,48] Thus, the electrons are injected from the conduction band (CB) of the photocatalyst into the metal nanoparticles (Pd in this work), where they are accumulated and/or consumed for reactions:[139]

On the other hand, charge recombination can be avoided by consuming holes by an appropriate sacrificial agent. In titania-based catalysts, such quenching can occur directly over the TiO_2 surface, or indirectly in the solution mediated by highly oxidizing species,[140] such as ·OH radicals, O_2^- and H_2O_2. Among them, ·OH formed from the reaction $H_2O_{ads} + h^+ \rightarrow {\cdot}OH_{ads} + H^+_{ads.}$, are generally considered responsible for initiating oxidation processes.

Among the sacrificial electron donors, alcohols have drawn great attention since the hydroxyl group favor the photoreforming process occurring over the surface of the TiO_2, due to an effective binding of the organic molecule on the catalytic sites. Bowker et *al*.[141] concluded that alcohols undergo readily oxidation allowing the photoreforming process while corresponding alkanes and alkenes result inactive under the same conditions. The dehydrogenation mechanism of such alcohols was elucidated by Bahruji et *al*.[142] who found that, in general, H_2 production is improved by a high number of hydrogen atoms in the α-position with respect to the OH group. In the same work they proposed different mechanisms for H_2 production: α-hydrogen dissociation with formation of an aldehyde and β-hydride elimination to a ketone from primary and secondary alcohols respectively. In the case of tertiary alcohols, where no α-hydrogen are available, no activity in H_2 production was detected.

Photoreforming processes involving noble metal/TiO_2-based catalysts undergo deactivation phenomena mainly because of the accumulation of by-products in the reaction medium (the liquid phase). Such by-products, in the case of primary alcohols, have lower adsorption capabilities compared to ethanol due to the absence of OH groups. This implies a lower effectiveness of the oxidation processes occurring at the surface. On the other hand, the oxidized carbonyl and carboxyl groups are able to poison the metal nanoparticles reducing the surface area for H_2 evolution.

4.1.1 H_2 production through ethanol photoreforming

Based on mechanistic studies, the photodehydrogenation to acetaldehyde is the major process involved in H_2 evolution from ethanol photoreforming.[48,142] The stepwise oxidation of ethanol can proceed either through direct interaction with the photogenerated h^+ (over the TiO_2 surface) or indirectly by interaction with ·OH (in the liquid phase).[143] Most likely, the two oxidation pathways are simultaneously proceeding. A schematic representation of a theoretical complete oxidative process occurring over the TiO_2 surface is shown in **Figure 4.1**.

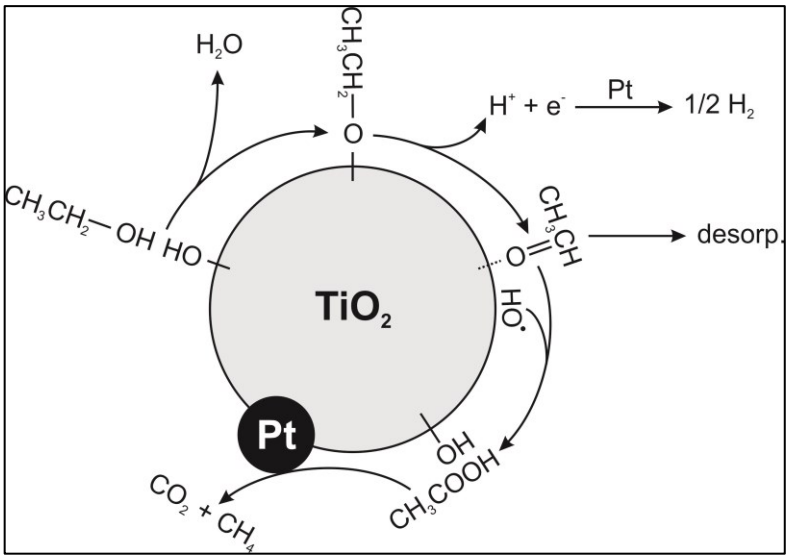

Figure 4.1: Schematic representation of the oxidative processes occurring over the TiO_2 surface during ethanol photoreforming.

The first step is the acetaldehyde production by oxidation of adsorbed ethoxide species resulting from dissociative adsorption of ethanol on TiO_2 surface.[144] Oxidation of acetaldehyde to acetic acid is considered to be the rate determining step with TiO_2 catalysts in ethanol photoreforming because of the low adsorption capability of the acetaldehyde onto the TiO_2. However, the formation of traces of acetic acid is expected to occur through oxidation in solution (**Figure 4.2**) by some radical species formed in situ (mainly ·OH). For this reason the acetaldehyde uses to accumulated in the liquid phase and it can easily reacts with ethanol in the presence of acidic sites in the TiO_2 forming the acetal 1,1-diethoxyethane. The same acidic sites expectedly promote the formation of both ethylene by dehydration of ethanol and ethane by hydrogenation of ethylene. The latter can be obtained also through radical coupling of $\cdot CH_3$. Moreover, the detection of CH_4 and CO_2 in equimolar amounts can be ascribed to either direct decomposition of acetic acid[145] or by decomposition of acetaldehyde to CH_4 and CO, followed by oxidation of CO to CO_2 through a "photocatalytic Water Gas Shift Reaction".[146]

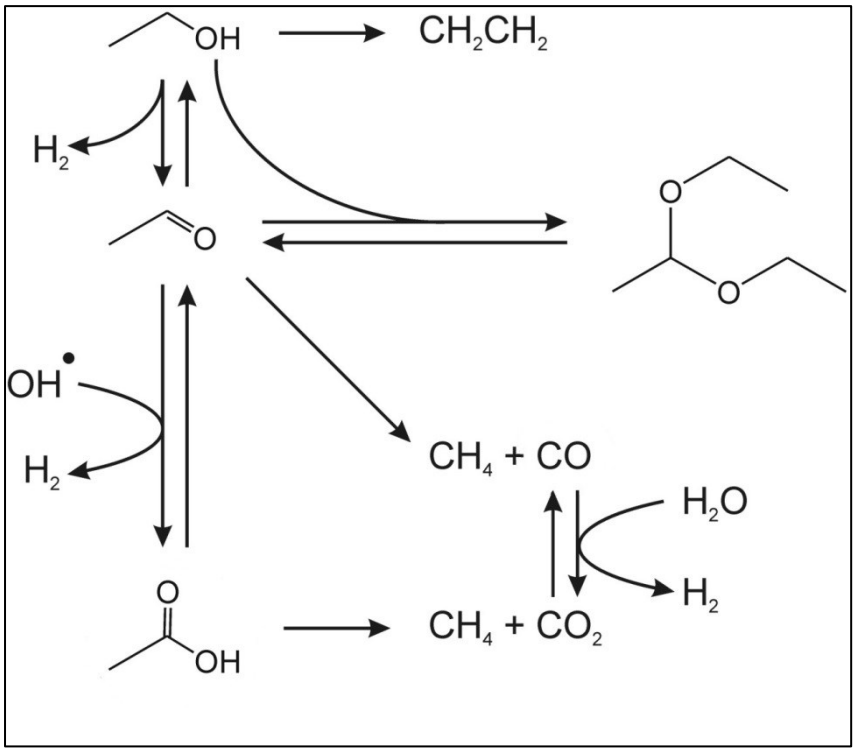

Figure 4.2: Schematic photoreforming pathway of ethanol.

4.1.2 H_2 production through glycerol photoreforming

Differently from the case of ethanol, the glycerol can be dehydrogenated through two different pathways (**Figure 4.3**), forming 2,3-dihydroxy-propanal and 1,3-dihydroxy-2-propanone respectively according to whether an external OH group or an internal one are involved. These carbonylic compounds formed by the first dehydrogenation still contain OH groups, that allow their adsorption on the TiO_2 surface and the competition with glycerol to be oxidized by the holes. CO and CO_2 formation are usually related to the photocatalytic degradation of carbonylic and carboxylic intermediate compounds, formed by progressive dehydrogenation of the glycerol molecule, mainly through 2,3-dihydroxy-propanal and leading to intermediate smaller compounds (hydroxyl acetaldehyde, formic acid and acetic acid).[48] On the other hand, 1-hydroxy-2-propanone is presumably formed on the surface of the TiO_2 via dehydration/hydrogenation from 1,3-dihydroxy-2-propanone, hardly oxidized/decomposed on TiO_2 surface by holes, or directly by dehydration of glycerol.

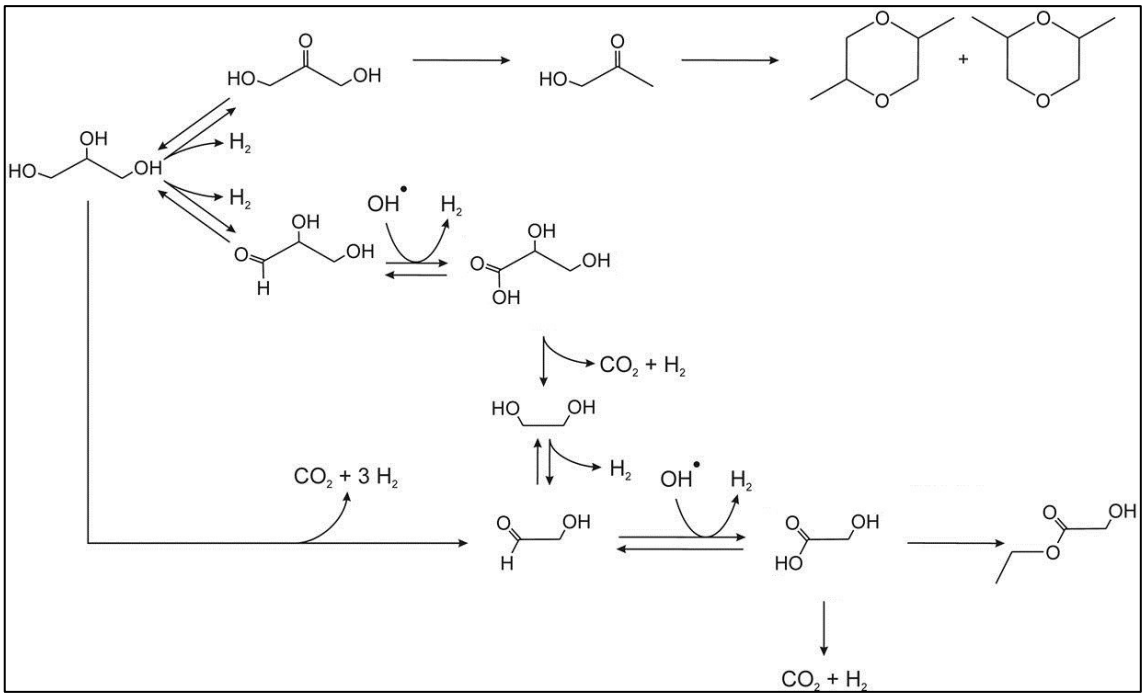

Figure 4.3: Schematic photoreforming pathway of glycerol.

PART 1: CNTs-based materials

4.2 CATALYST DESIGN

A ternary hierarchical hybrid comprising MWCNTs, TiO_2 and Pd NPs was prepared to be employed as catalyst for the photoreforming of alcohols. An exhaustive description of the catalyst design is presented in paragraph 3.2. The same features of the final hybrid as those described for MWCNTs/Pd@CeO_2 were pursued in order to enhance the activity of the carbon/inorganic nanohybrid: *i*) improving the preservation of the electronic properties of the MWCNTs; *ii*) obtaining highly homogeneous structures by optimizing the coating of the MWCNTs; *iii*) increasing the inherent activity of the metal oxide/noble metal by performing an opportune crystallization of the inorganic matrix. As explained above, an important factor to enhance the activity of a photocatalyst is to reduce the recombination rate of the photogenerated electrons and holes. In the present scenario, a rationale for the employment of MWCNTs in the design of the catalyst is based on the ability of MWCNTs to act as electron scavengers, thus retarding the charge recombination rates.[72] Moreover, the thermal treatments enhance the crystallinity of the inorganic matrix reducing the number of structural defects, that act as recombination centers.

Other possible roles for the MWCNTs are however plausible, as explained in paragraph 1.4.

4.3 CATALYST PREPARATION

The MWCNTs-based materials employed as catalysts for the photoreforming of alcohols were assembled starting from three building blocks: *i*) benzoic acid-functionalized MWCNTs (*f*-MWCNTs); *ii*) palladium nanoparticles protected by mercapto-undecanoic acid (Pd-MUA); *iii*) titanium (IV) *n*-butyl alkoxide (Ti(O-*n*-Bu)$_4$). The building blocks of the carbon/inorganic nanohybrid catalysts were prepared separately and then assembled to obtain the final material. The overall process is exhaustively described in the paragraph 3.3.

For the synthesis of the *f*-MWCNTs and the Pd-MUA see respectively paragraphs 3.3.1 and 3.3.2. The Ti(O-*n*-Bu)$_4$ was purchased from Sigma-Aldrich.

Materials with three different nominal compositions have been prepared and labelled as follows: **10-CNTs/Pd@TiO_2**, **20-CNTs/Pd@TiO_2** and **Pd@TiO_2**, respectively with 10, 20 and 0 nominal % wt of MWCNTs. The nominal amount of Pd was set at 1.5 % wt for all the samples. The materials were subjected to a thermal treatment (at 350 °C), indicated by an appropriate suffix (e.g. **20-CNTs/Pd@TiO_2-350**).

Hybrid assembly (CNTs/Pd@TiO_2)

100 mg of **10-CNTs/Pd@TiO_2-350** or **20-CNTs/Pd@$TieO_2$-350** were prepared employing respectively 10 and 20 mg of *f*-MWCNTs dispersed in absolute ethanol (EtOH mL/ *f*-MWCNTs mg ratio equal to 2.5) by sonication in an ultrasonic bath for 30 minutes. Meanwhile a fresh Pd-MUA THF solution (0.3 mg Pd/mL) containing 1.5 mg of Pd was slowly added under magnetical stirring respectively to 1.48 and 1.31 mL of THF solution of Ti(O-*n*-Bu)$_4$ (60 mg TiO_2/mL). The fresh Pd-MUA@Ti(O-*n*-Bu)$_4$ solution was then slowly added under sonication to the *f*-MWCNTs dispersion and the mixture further sonicated for 30 minutes. Finally a 10% solution H_2O in EtOH (Ti(O-*n*-Bu)$_4$/H_2O molar ratio equal to 1/120) was slowly added dropwise under sonication into the mixture, that was then further sonicated for 30 minutes. The obtained materials were collected by filtration through a 0.45 μm PTFE Millipore membrane, washed with ethanol twice (5 min of sonication of the solid in the solvent) and subsequently dried overnight at 80 °C. The fresh materials were finally subjected to calcination at 350 °C for 5 hours (heating at 3 °C/min; cooling at 4.5 °C/min).

Pd@TiO_2-350 (containing 1.5 % wt of Pd) was prepared following the same procedure but in absence of MWCNTs.

4.4 CHARACTERIZATION AND RESULTS

The composition, the morphology, the structure and the textural properties of the materials presented in this chapter were characterized through a combination of several techniques in order to confirm the correct assembly of the carbon/inorganic nanohybrid.

4.4.1 Thermogravimetric analysis

The composition of the prepared hybrid materials was evaluated through thermogravimetric analysis (TGA) under air (**Figure 4.4**). In the first instance, the successful functionalization of the sidewalls of the **Pristine MWCNTs** was evidenced by a weight loss (about 4.5 %) at 350-450 °C. This weight loss corresponds to the decomposition of the benzoic acid groups, since this range of temperatures is tolerated by the MWCNTs. TGA analysis were then run for the hybrid materials. It qualitatively confirmed the presence of functional groups in the ***f*-MWCNTs** and gave information about the thermal tolerance of the fresh carbon/inorganic hybrid materials. The fresh hybrid materials present two different weight losses. The first one at 150-350 °C corresponds to the removal of the organic ligands of the metal precursors (i.e. MUA and butanol) and of residual H_2O into the inorganic matrix. The second weight loss is due to the complete combustion of the nanostructured carbon skeleton, which occurs at 450-650 °C. Notably, in contrast to what observed for materials based on CeO_2 (see paragraph 3.4.1), the TiO_2 shell does not dramatically promote the oxidation of the MWCNTs. This allows to select 350 °C as the temperature for the thermal treatments of the fresh hybrid materials. After calcination, TGA under air flow shows that the carbon content in the final composite materials is around 9 and 14 wt% for **10-CNTs/Pd@TiO_2-350** and **20-CNTs/Pd@TiO_2-350**, respectively.

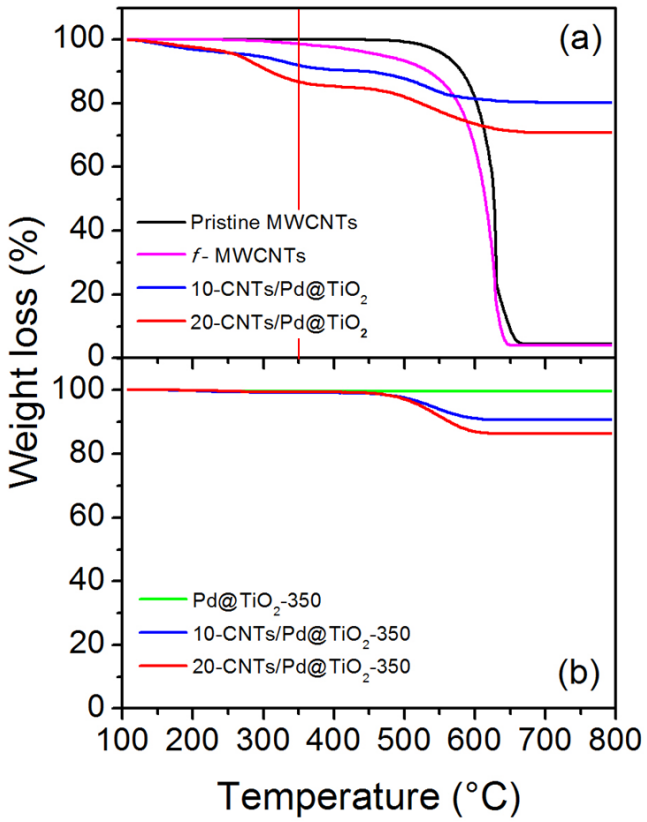

Figure 4.4: Thermogravimetric analysis of the samples after drying (a) and of the samples after calcination at 350 °C in air (b). The red vertical line indicates the calcination temperature (350 °C) of the fresh materials.

As expected, the carbon-free calcined material **Pd@TiO₂-350** presents no significant weight loss (**Figure 4.4**) because of the absence of the carbonaceous scaffold and the complete removal of the organic residual ligands during the thermal treatment.

4.4.2 Structural analysis

Raman spectra were collected at each stage of the synthesis to verify the effective assembly of the various components of the hybrid materials. The functionalization of the **Pristine MWCNTs** was exhaustively explained in paragraph 3.4.2 by comparison with the ***f*-MWCNTs**: the ratio between the D band and the G band (I_D/I_G) is a semi-quantitative parameter to assess the degree of introduced defects, caused by the covalent functionalization.[128,129]

As a representative example, **Figure 4.5** compares, the Raman spectra of the various materials at different stages of the synthesis of **20-CNTs/Pd@TiO₂-350**. After the hybridization with Pd@TiO_2, the Raman spectra of the fresh sample suggests that TiO_2 is predominantly present as an amorphous phase, as no peaks associated to any crystal phase of TiO_2 are found. The thermal treatment induces the crystallization of the TiO_2 shell, with appearance of an intense band at 146 cm^{-1} and minor bands at 198 cm^{-1}, 395 cm^{-1}, 513 cm^{-1} and 639 cm^{-1} is observed the typical Raman fingerprint of TiO_2 anatase.[147,148] In agreement with the synthetic protocol and with TGA, the sample **Pd@TiO₂-350** prepared without MWCNTs showed only the bands related to the anatase phase.

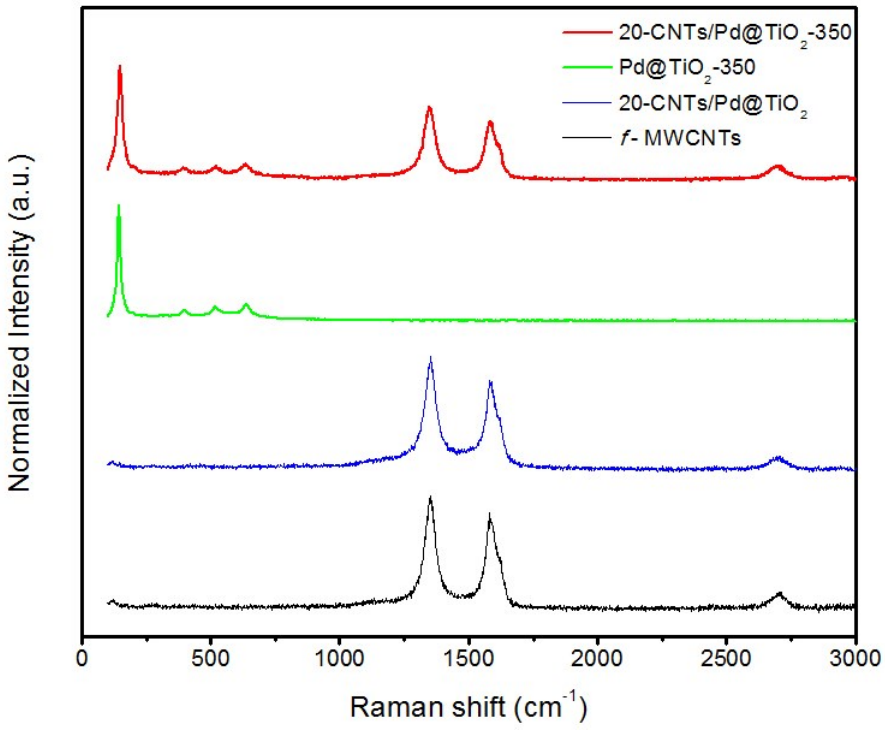

Figure 4.5: Raman spectra of ***f*-MWCNTs**, **20-CNTs/Pd@TiO₂**, **20-CNTs/Pd@TiO₂-350** and **Pd@TiO₂-350**.

XRD patterns of the samples calcined at 350 °C confirm the crystallinity of the materials and the presence of only anatase phase (**Figure 4.6**). The mean crystallite size of TiO_2 was calculated by applying the Scherrer's equation (**Eq. 2.7**) to the main

reflection (101) and results equal to 11, 13 and 12 nm for the **Pd@TiO₂-350**, **10-CNTs/Pd@TiO₂-350** and **20-CNTs/Pd@TiO₂-350** samples respectively. It is reasonable to conclude that the formation of the carbon/inorganic hybrid is not significantly affecting the nanocrystalline behavior of the materials because the growth of anatase crystallites appears to be mainly directed by the self-assembling around Pd nanoparticle. Notably, no reflections can clearly be related with Pd nanoparticles, reasonably because of the low metal loading and the small average size of Pd nanoparticles, as also observed by HR-TEM (see paragraph 4.4.3).

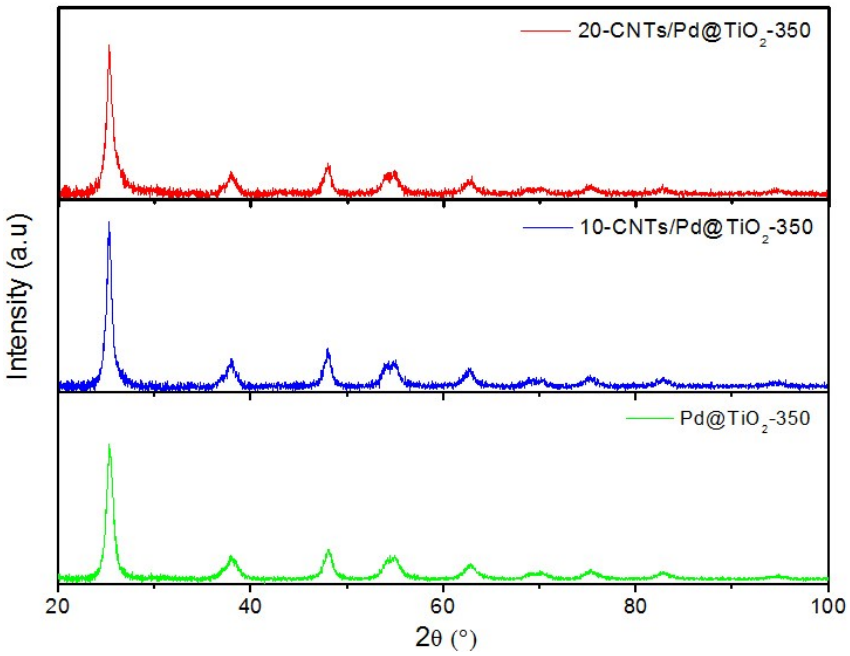

Figure 4.6: Powder XRD patterns of the samples calcined in air at 350 °C.

4.4.3 Morphological analysis

Transmission electron micrographs (TEM analysis) confirm the correct assembly of the hybrids, displaying an intimate contact between the carbon and the inorganic matrix. The morphologies of **10-CNTs/Pd@TiO₂** and **20-CNTs/Pd@TiO₂**, both fresh and calcined, appear similar. The MWCNTs are homogeneously covered with an amorphous TiO_2 shell (**Figure 4.7** A and C) in the fresh materials. It is worth noting that a few bare CNTs regions are also present. The thermal treatment clearly modifies the texture of the inorganic matrix, that becomes rougher as a consequence of the crystallization of the oxide shell (**Figure 4.7** B and D). This was better shown by a high

resolution magnification of the TiO_2 layer and by Fast Fourier Transform (FFT) of a selected area, which confirm that the calcined samples present a polycrystalline anatase phase for the TiO_2 shell, whose particle size averages 10 nm (**Figure 4.8**), in good agreement with XRD analysis. A statistical investigation (50 structures per sample) reveals a significant difference in terms of TiO_2 layer average thickness between samples **10-CNTs/Pd@TiO₂-350** and the **20-CNTs/Pd@TiO₂-350**, with values of 40 and 35 nm respectively. This difference must be obviously related to the different C/TiO_2 relative ratios. It must be noted that in **10-CNTs/Pd@TiO₂** and **20-CNTs/Pd@TiO₂** samples the amounts of the inorganic matrix are comparable while the while the carbon component differ by a 100 wt %, corroborating the important role of the carbon component.

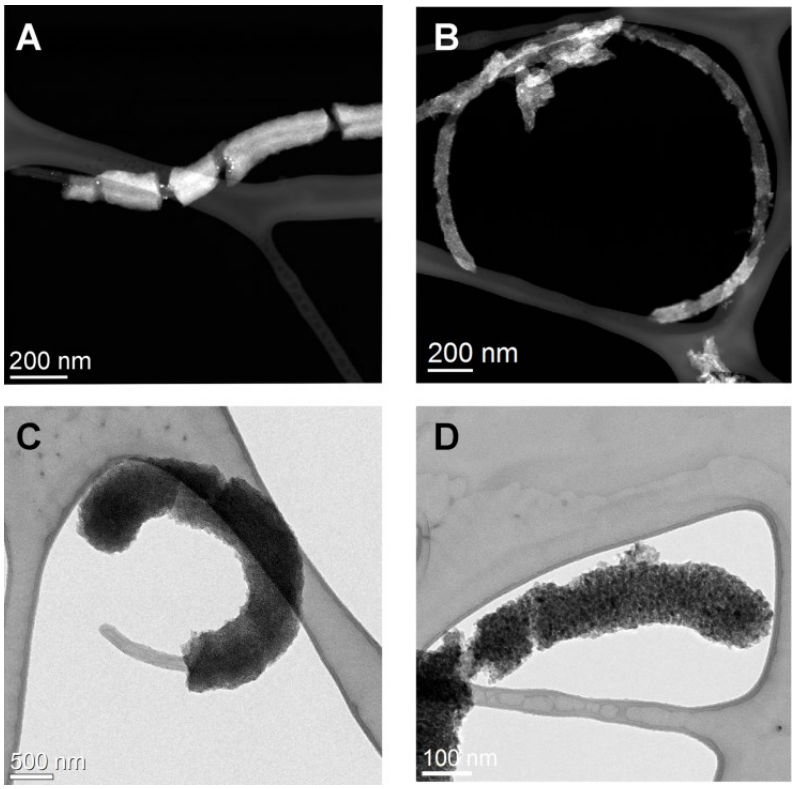

Figure 4.7: Representative HAADF-STEM of **20-CNTs/Pd@TiO₂** (A) and **20-CNTs/Pd@TiO₂-350** (B). Representative HR-TEM of **20-CNTs/Pd@TiO₂** (C) and **20-CNTs/Pd@TiO₂-350** (D). The morphology of catalysts **10-CNTs/Pd@TiO₂-** and **10-CNTs/Pd@TiO₂-350** are similar.

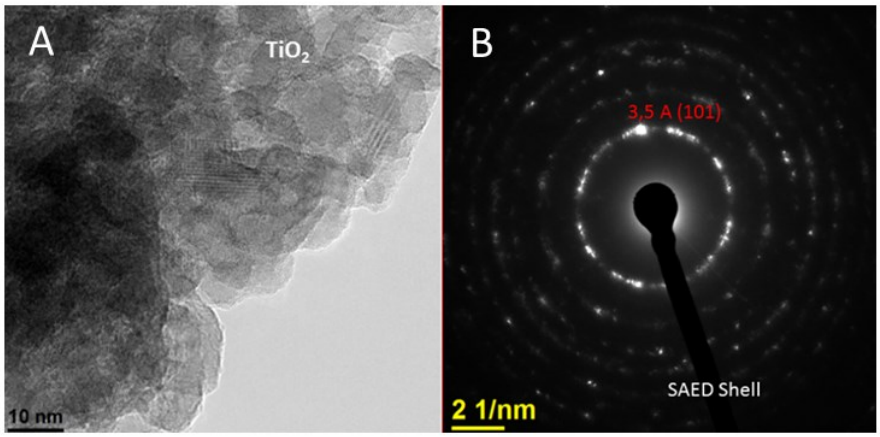

Figure 4.8: HR-TEM of the titania shell in **20-CNTs/Pd@TiO2** (on the left); FFT of a selected area showing the reflections of TiO_2 anatase phase (on the right).

The incorporation of the three components (MWCNTs, TiO_2 and Pd NPs) within the hybrid materials and their co-location are corroborated by a combined HAADF-STEM and EDX mapping analysis (**Figure 4.9**). The MWCNTs appear homogeneously covered by an inorganic shell. The presence and the optimum distribution of the Pd nanoparticle inside the TiO_2 shell confirm the hierarchical assembly of the materials.

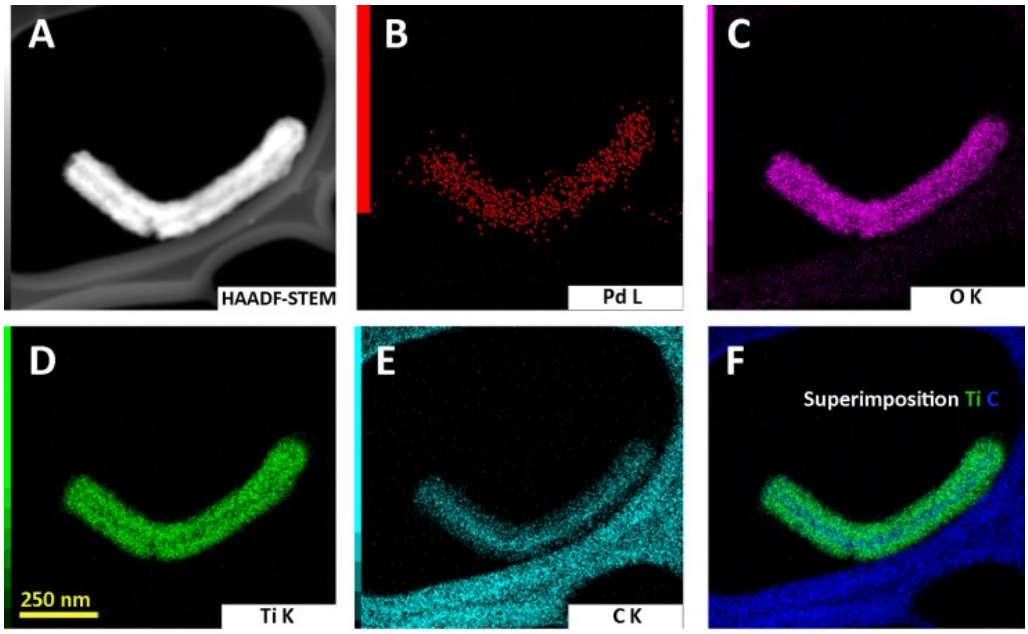

Figure 4.9: A) Representative HAADF-STEM of a CNTs/Pd@TiO_2-350; B-E) EDX mapping showing the intimate contact between the three components: in respectively palladium, oxygen, titanium and carbon; F) superimposition of the EDX signal of carbon and titanium. Note that also the carbon grid is visible and should not be confused with the MWCNTs.

4.4.4 Textural analysis

The textural properties of the hybrid materials at each step of the synthesis have been investigated by N_2 physisorption at the liquid nitrogen temperature (**Figure 4.10** and **Table 4.1**). According to the IUPAC classification,[94] all the samples present type IV physisorption isotherms, typical of mesoporous materials.

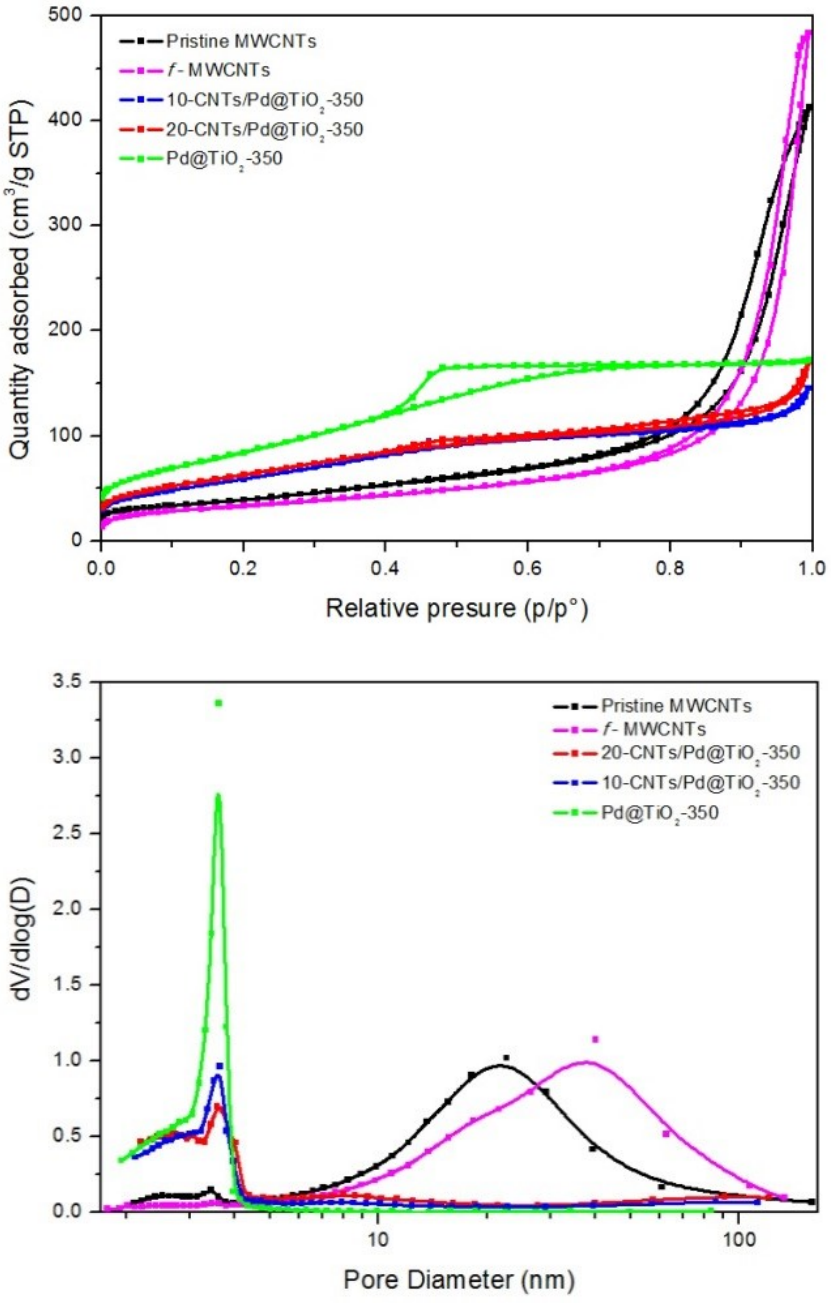

Figure 4.10: N_2 physisorption isotherms (on the top) and BJH pore size distribution (on the bottom) of the materials.

As exhaustively explained in paragraph 3.4.4, the covalent functionalization of the **Pristine MWCNTs** causes a slight decrease of the surface area (from 142 to 117 m^2/g) and an increase of the cumulative pore volume and the maximum of the pore size distribution (from 22 to 37 nm), as a consequence of the unbundling process. Furthermore, the contribution of mesopores smaller than 5 nm appears largely reduced.

On the other hand, the textural properties of the materials dramatically change after the hybridization with the TiO_2 shell and the subsequent calcination at 350 °C. The pore size distribution completely shifts to the range 2 – 4 nm and, as a consequence, the cumulative pore volumes are reduced while specific surface areas significantly increased (**Table 4.1**).

Pd@TiO₂-350 presents textural properties comparable with the hybrid materials, confirming that the changes in the textural properties are mainly related to the inorganic matrix.

The contribution of micropores is negligible in all the investigated samples.

Table 4.1: Summary of the textural properties of the investigated materials from N_2 physisorption measurements.

Sample	Specific Surface Area[1] (m^2/g)	CPV[2] (mL/g)	D_{max}[3] (nm)
Pristine MWCNT	142	0.634	3.4/22
***f*- MWCNT**	117	0.741	37
Pd@TiO₂-350	323	0.290	3.6
10-CNTs/Pd@TiO₂-350	222	0.236	3.6
20-CNTs/Pd@TiO₂-350	228	0.274	3.6

[1] Specific Surface Area calculated from the BET analysis of the isotherms;

[2] Cumulative Pore Volume calculated from the BJH analysis of the desorption branch of the isotherms;

[3] Relative maxima of the pore size distributions obtained by the BJH analysis of the desorption branch of the isotherms.

4.4.5 Chemisorption measurements

The accessibility of the Pd nanoparticles in the calcined carbon/inorganic hybrids has been evaluated by H_2 chemisorption measurements and the result are summarized in **Table 4.2**. Samples were reduced at moderate temperature (H_2 5%/Ar 40 mL/min at 100°C for 30 minutes) to avoid a significant deactivation of the H_2 adsorption on the Pd surface by strong metal-support interaction (SMSI) induced by the reduced TiO_2.[149,150] The analyses were carried out at low temperature (around -90°C using a solid/liquid acetone bath) to minimize H spillover to the reducible support.[151] At low H_2 pressure (below 20 nm), H_2 interaction with Pd nanoparticles results only in the adsorption of H atoms on the metal surface. Above this pressure, the migration of H into the bulk of Pd is favored, forming Pd hydride (PdH_X) [99] and resulting in a further contribute to H_2 consumption.

The contribution of H adsorbed on the surface has been calculated by extrapolation of the linear part in the 10-20 mmHg range while the overall hydrogen consumption has been calculated after subtraction of the physisorbed H_2 by linear extrapolation of the isotherms in the range 200–400 mmHg (**Figure 4.11**). The amount of hydrogen involved in PdH_X formation and the stoichiometry of the formed PdH_X have been calculated by difference of the two quantities (**Table 4.2**).

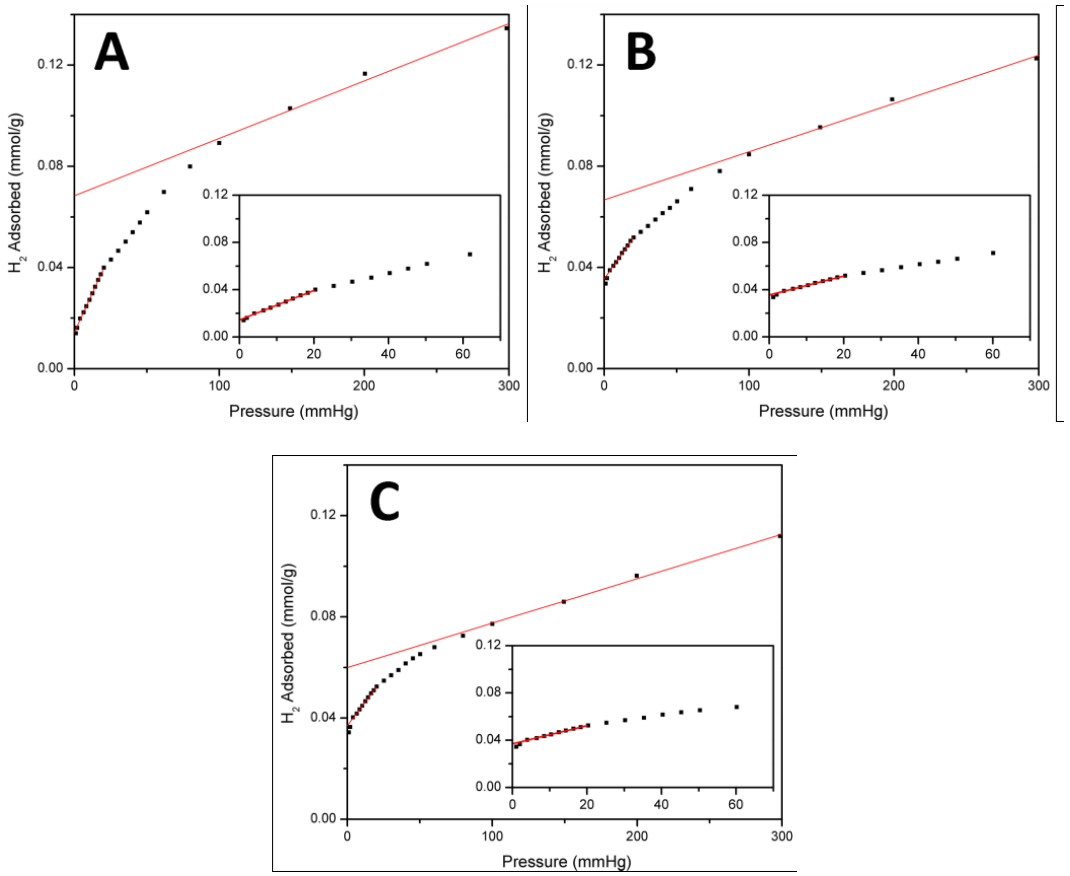

Figure 4.11: H_2 chemisorption isotherms measurements for **Pd@TiO₂-350** (A), **10-CNTs/Pd@TiO₂-350** (B), **20-CNTs/Pd@TiO₂-350** (C). Insets: extrapolation of the linear part in the 10-20 mmHg range to evaluate contribution of H adsorbed on the surface.

The accessibility of the Pd phase is significantly higher in the carbon/inorganic hybrid materials with respect to the **Pd@TiO₂-350** carbon-free material. It is reasonable to hypothesize that the formation of the hybrid structure allows a more efficient encapsulation and stabilization of Pd nanoparticles, and that the monodimensional morphology improves accessibility. Notably, the amount of H absorbed in the formation of PdH_X species is higher for the fully inorganic material. This result is in agreement with the dependence of solubility hydrogen in small Pd nanoparticles reported by Boudart and Hwang:[152] the larger the Pd nanoparticles, the higher the solubility of H forming PdH_X species.

Table 4.2: Summary of the metal textural properties of the investigated materials from H_2 chemisorption measurements.

Sample	H_{surf}/Pd	Metallic surface area ($m^2\ g^{-1}$)	Apparent Particle Size (nm)	X in PdH_X
$Pd@TiO_2$	**0.20**	**1.4**	**5.5**	**0.77**
10-CNT/$Pd@TiO_2$	**0.50**	**3.4**	**2.2**	**0.45**
20-CNT/$Pd@TiO_2$	**0.52**	**3.5**	**2.1**	**0.33**

4.4.6 Catalytic results

UV-vis irradiation:

The activity of the prepared materials was evaluated in terms of hydrogen production rates and overall H_2 amounts per time.

Preliminary tests were performed in aqueous solutions containing methanol 50% *v/v* (**Figure 4.12**). Together with H_2, the production of CO and CO_2 has been observed (data not shown). Despite not being the most sustainable choice in terms of sacrificial agent, the use of methanol allows the direct comparison of the activity of the present materials with literature data (**Table 4.3**) since most of the catalysts were tested this sacrificial agent. It must be underlined that all the other experimental conditions adopted in a photocatalytic experiment (reactor design, power of the light source, geometrical area of the irradiated surface, concentration of photocatalyst and sacrificial agent, temperature, etc.) strongly affect the H_2 productivity, getting more difficult any direct quantitative comparison. Nevertheless, the results obtained with the best performing photocatalysts reported in the literature are summarized for comparison. In our case, the fresh catalysts show a modest activity, due to the amorphous state of the TiO_2 shell. On the other hand, the thermal treatment strongly increases the H_2 production. This behavior can be reasonably related to the nanocrystallization of the TiO_2 shell to form a porous network that enhance the Pd nanoparticles accessibility. The thermal treatment can also be

associated to a tighter contact between the nanocarbon structures and the inorganic matrix causing an increased number of heterojunctions, which has been shown to be an important parameter to improve performance.[153]

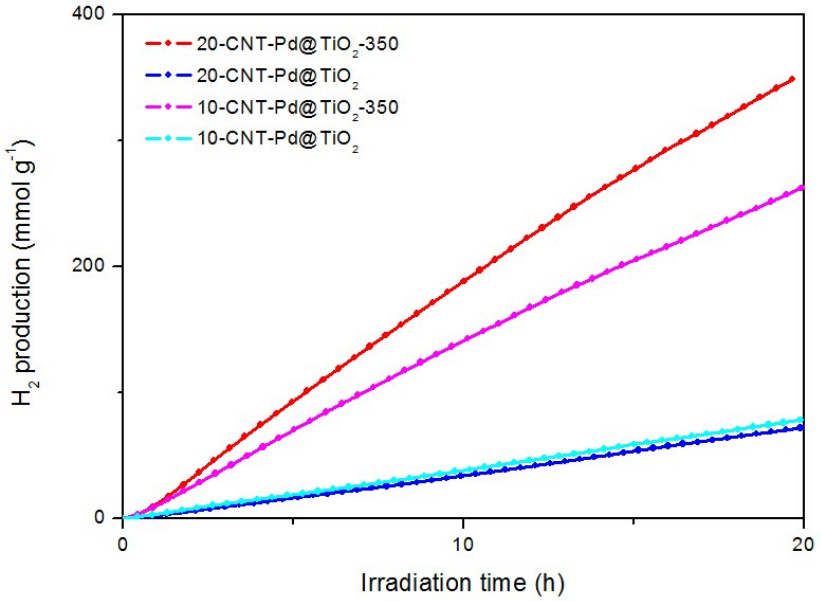

Figure 4.12: Results from photocatalytic hydrogen production from methanol/water solutions under UV irradiation for the fresh and calcined catalysts. Activities are normalized by the grams of catalyst.

Undoubtedly, the thermal treatment has a positive effect on the performance of the present hybrid materials. For this reason, only the calcined samples have been employed in the following photocatalytic studies for H_2 production using more sustainable biomass-derived sacrificial agents, i.e. ethanol and glycerol.

Under UV-vis irradiation, the amount of produced H_2 increases over time with all the investigated catalysts using both ethanol and glycerol aqueous solutions (**Figure 4.13**), as already observed for catalytic systems based on metal modified TiO_2.[154,48,155]

When ethanol is used as sacrificial agent, the H_2 production reaches an outstanding value of 2.4 mmol m_{cat}^{-2} (corresponding at 0.55 moles of H_2 g_{cat}^{-1} in 24 h) for **20-CNTs/Pd@TiO2-350** catalyst after 24 hours under UV-vis illumination, while the photocatalyst with a lower CNTs content exhibit lower activity (2.0 mmol m_{cat}^{-2}).

By comparison, the activity of the reference catalyst **Pd@TiO$_2$-350** was only 0.5 mmol m_{cat}^{-2}. This is a clear indication of the beneficial effect that the MWCNTs scaffold has in the photocatalytic hydrogen evolution, attributed to its electronical properties which provide an extremely proficient electron scavenging that retard charge carrier recombination.

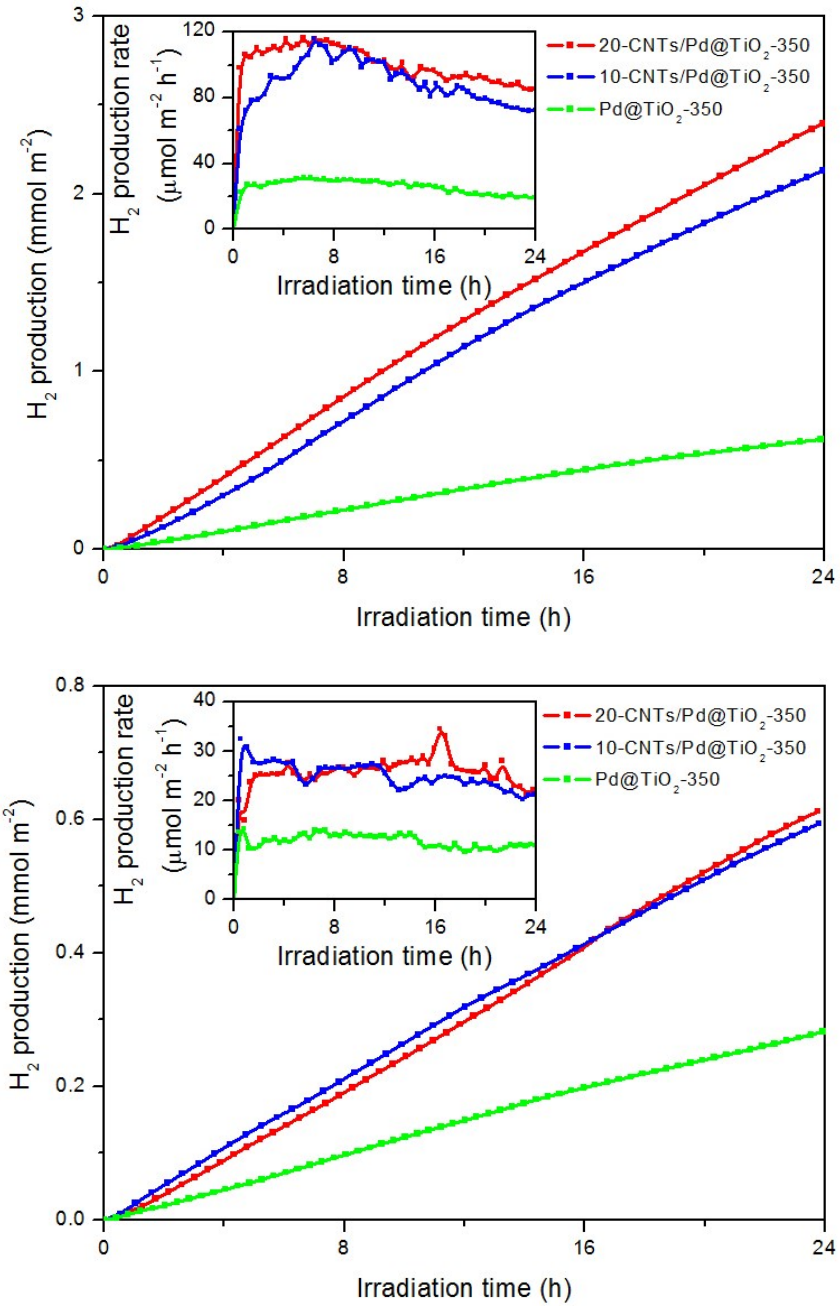

Figure 4.13: H_2 production over time under UV-vis illumination using aqueous solution of ethanol (top) and glycerol (bottom) as sacrificial donor. Activities are normalized by the catalyst surface areas reported in **Table 4.3**.

Table 4.3: Comparison with the performance of some recent catalytic systems containing carbon supports and integrated metal phases.

Carbon Support	Metal phase	Maximum rate of H_2 evolution ($mmol \cdot g^{-1} \cdot h^{-1}$)	Hole scavenger	Power of irradiating lamp and λ range (nm)	Ref.
GO	Pt/CdS	55	Lactic Acid	350W (λ>420)	[156]
Ox-MWCNT	Pt/TiO_2	40	Methanol	200W (240<λ<500)	[157]
ox-CNCs (20%)	Pd/TiO_2	37	Ethanol	125W (λ>365)	*[158]
MWCNTs	Pt/Ta_2O_5	32	Methanol	450W (λ>365)	[159]
f-MWCNTs (20%)	Pd/TiO_2	26	Ethanol	125W (λ>365)	*[160]
f-MWCNTs (20%)	Pd/TiO_2	21	Methanol	125W (λ>365)	*[160]
GO	Cu/TiO_2	19	Methanol	300W (λ>365)	[161]
RGO	Pt/TiO_2	14	Methanol	300W	[162]
Ox-MWCNTs	Pt/TiO_2	10	Methanol	125W (λ>365)	[118]
Ox-MWCNTs	Pt/TiO_2	8	TEA	250W (λ>320)	[163]
f-MWCNTs (20%)	Pd/TiO_2	6	Glycerol	125W (λ>365)	*[160]
C_{60}-SWCNTs	TiO_2	3.2	TEA	300W (λ>320)	[164]
GO	$Pt/Sr_2Ta_2O_{7-x}N_x$	3	Methanol	300W (λ>420)	[165]
Ox-CNTs	TiO_2	2	Glycerol	Not specified	[166]

* = this work
TEA = Triethanolamine

Reporting the H_2 production rates by gram of catalyst (**Figure 4.14**), the activities are among the highest ever reported for catalysts based on titania (**Table 4.3**) and carbonaceous supports with values above 25 mmol g^{-1} h^{-1} for **20-CNTs/Pd@TiO_2-350** sample and 20 mmol g_{cat}^{-1} h^{-1} for the **10-CNTs/Pd@TiO_2-350** sample.[160] Indeed the quantum efficiency (QE) at 365 nm of the materials, respectively 21% and 17%, confirm the promising performance of these hybrid materials.

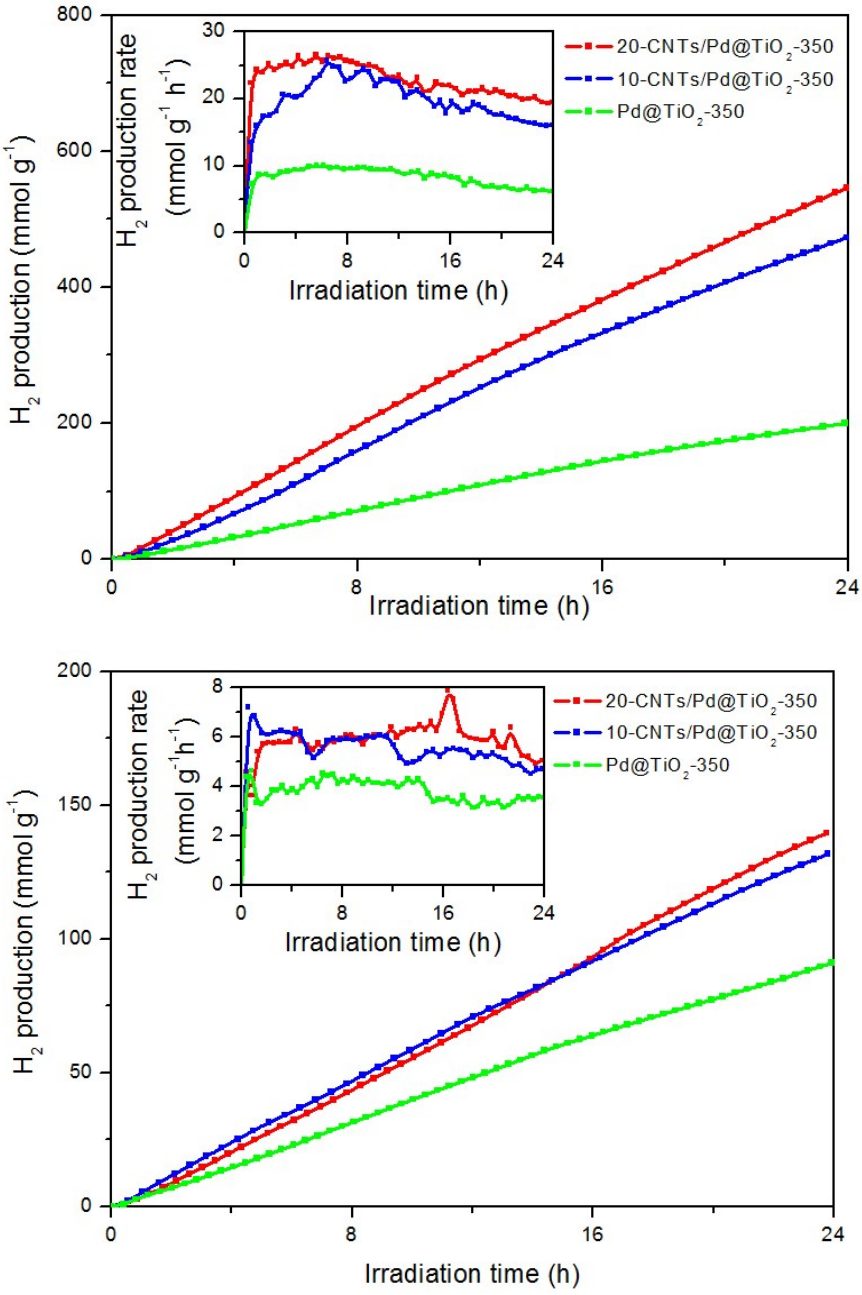

Figure 4.14: H_2 production over time under UV-vis illumination using aqueous solution of ethanol (top) and glycerol (bottom) as sacrificial donor. Activities are normalized by grams of catalyst.

In the case of glycerol as sacrificial agent, a lower H_2 production is reached because of the more challenging dehydrogenation process. Samples **10-** and **20-CNT/Pd@TiO2-350** displayed a very similar activity normalized by the surface area (~ 0.6 mmol m_{cat}^{-2}), while the activity of **Pd@TiO2-350** was significantly lower (0.3 mmol m_{cat}^{-2}).By comparison with literature, the activity results for the present catalysts are among the highest ever reported under these conditions (**Table 4.3**).

Slight deactivation processes in both ethanol and glycerol photoreforming tests are presumably due to partial aggregation or deposition of the solid catalyst on the walls of the reactor and out of the irradiated area.

The investigation of the by-products that evolves together with H_2 reveals the complexity of the mechanism. No O_2 evolution was observed, implying that the water splitting contribution to the photocatalytic H_2 evolution is negligible. Indeed, when pure water was used as photogenerated holes and electrons acceptor, a very small evolution of H_2 (~ 210 μmol g^{-1} h^{-1}) was detected, while the addition of methanol results in a considerable enhancement of the H_2 evolution rates (**Figure 4.15**).

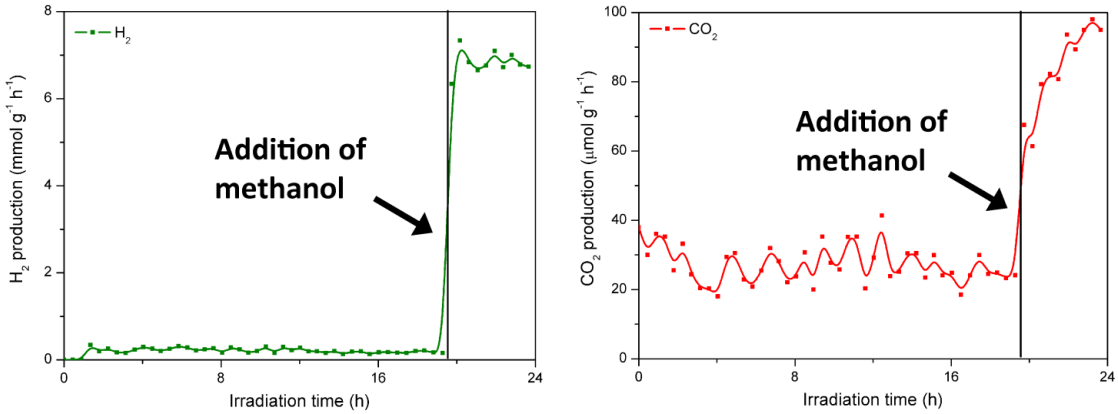

Figure 4.15: Photocatalytic water splitting under UV irradiation. Methanol (10% v/v) was added after 19 h. Activities (H_2 on the left and CO_2 on the right) are normalized by the grams of catalyst (**20-CNTs/Pd@TiO₂-350**).

When ethanol is used as sacrificial agent the analysis of the gas phase evidences the presence of acetaldehyde and 1,1-diethoxyethane (its acetal with ethanol), CH_4 and CO_2 in equimolar amounts, together with ethane and traces of ethylene (**Figure 4.16** and **Figure 4.19**). Noteworthy, CO was observed only in negligible traces.

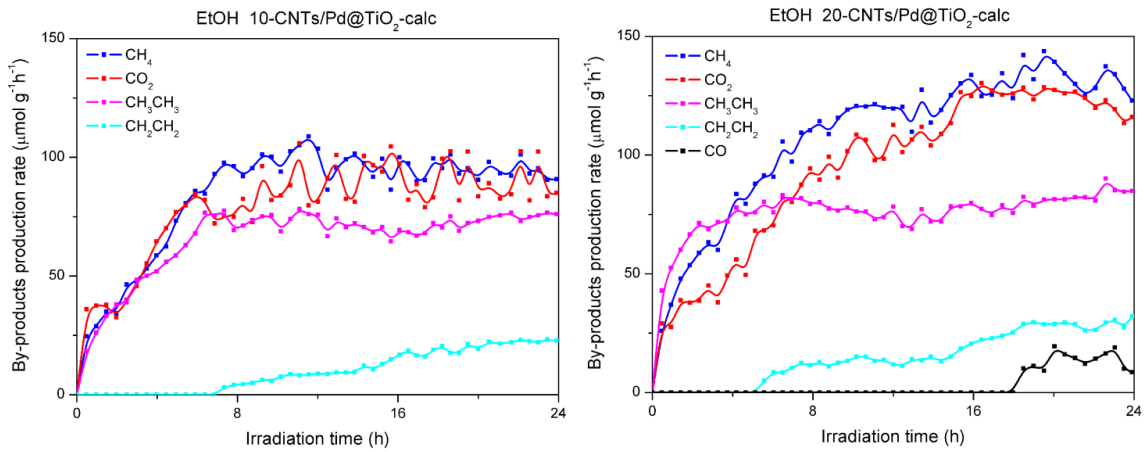

Figure 4.16: Gaseous by-products formation during photocatalytic H_2 production from ethanol/water solutions under UV irradiation with **10-CNT/Pd@TiO$_2$-350** (left) and **20-CNT/Pd@TiO$_2$-350** (right).

Moreover, the analysis of liquid phases recovered after the photocatalytic tests showed that the major part of acetaldehyde and 1,1-diethoxyethane were accumulated in solution, together with other by-products present in minor amount such as acetic acid, 2,4,5-trimethyl-1,3-dioxolane, 3-hydroxy-2-butanone and 2,3-butandiol (**Table 4.4**).

Table 4.4: Results from semi-quantitative analysis (1-butanol was used as internal standard) of liquid solutions collected after photocatalytic H_2 production from ethanol/water solutions under UV irradiation.

	10-CNTs/Pd@TiO$_2$-350	**20-CNTs/Pd@TiO$_2$-350**	**Pd@TiO$_2$-350**
Acetaldehyde	2.235	2.895	1.102
1,1-diethoxyethane	5.424	6.812	2.533
2,4,5-trimethyl-1,3-dioxolane	0.012	0.092	0
Acetic acid	0.026	0.145	0.003
3-hydroxy-2-butanone	0.026	0.045	0.006
2,3-butandiol	1.613	4.297	1.326

The detection of those large amounts of by-products suggest that the reforming process of ethanol is not complete. The photodehydrogenation of ethanol to acetaldehyde

is the major process involved in H_2 evolution and, according to **Figure 4.2**, it is possible to justify the presence of the majors by-products. Regarding the presence of ethane, it could arise through a radical mechanism, namely from the radical coupling of $\cdot CH_3$, or by hydrogenation of ethylene formed from ethanol on the acid sites of the TiO_2.

Furthermore, the contribution of acetaldehyde photodecomposition was confirmed by performing a photocatalytic experiment using acetaldehyde as sacrificial agent, added after 3 h of irradiation of the photocatalysts in pure water (**Figure 4.17**). After acetaldehyde addition, H_2 is produced in major amount, together with CH_4, CO_2 and traces of ethane.

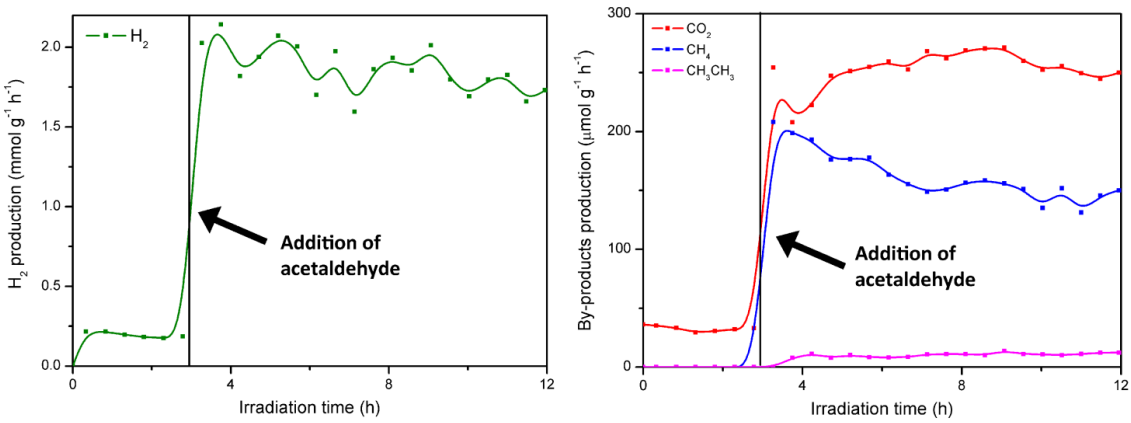

Figure 4.17: Photocatalytic water splitting under UV irradiation. Acetaldehyde (4% v/v) was added after 3 h. Activities (H_2 on the left and byproducts on the right) are normalized by the grams of catalyst (**20-CNTs/Pd@TiO₂-350**).

Among the other by-products accumulated in solution during ethanol photoreforming, 2,3-butandiol is probably formed through radical C-C coupling of two ethanol molecules. From this compound, 3-hydroxy-2-butanone is formed by dehydrogenation from one OH group while 2,4,5-trimethyl-1,3-dioxolane is formed by reaction of 2,3-butandiol with acetaldehyde.

In the case of glycerol, the analysis of the by-products in the gas phase evidences the presence of both CO_2 and CO together with trace amounts of ethane, with their formation rate increasing over time (**Figure 4.18** and **Figure 4.19**).

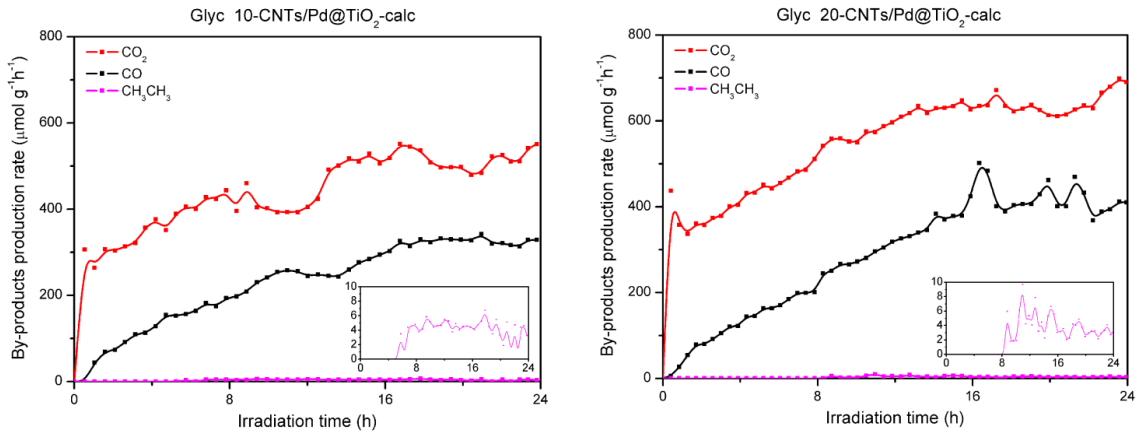

Figure 4.18: Gaseous by-products formation during photocatalytic H_2 production from glycerol/water solutions under UV irradiation with **10-CNT/Pd@TiO$_2$-350** (left) and **20-CNT/Pd@TiO$_2$-350** (right).

Finally, the analysis of liquid phases recovered after the photocatalytic tests showed an accumulation of non-volatile by-products (**Table 4.5**). Hydroxyl acetaldehyde, 1-hydroxy-2-propanone and 1,3-dihydroxy-2-propanone were the most abundant, followed by formic acid and 2,3-dihydroxy-propanal and trace amounts of acetic acid.

Table 4.5: Results from semi-quantitative analysis (1-hexanol was used as internal standard) of liquid solutions collected after photocatalytic H_2 production from glycerol/water solutions under UV irradiation.

	10-CNTs/Pd@TiO$_2$ - 350	**20-CNTs/Pd@TiO$_2$ - 350**	**Pd@TiO$_2$-350**
Hydroxy-acetaldehyde	2.34	3.03	1.65
Formic acid	0.37	0.26	0.22
Acetic acid	0.08	0.07	0.04
1-hydroxy-2-propanone	1.60	1.12	0.75
2,3-dihydroxypropanal	0.22	0.20	0.26
1,3-dihydroxy-2-propanone	1.62	2.05	1.13

The photodehydrogenation of glycerol to 2,3-dihydroxy-propanal and 1,3-dihydroxy-2-propanone and hydroxyl-acetaldehyde are the major processes involved in H_2 evolution and, according to **Figure 4.3**, it is possible to justify the presence of the other by-products. Moreover the results clearly indicate that oxidation/degradation of 2,3-dihydroxy-propanal is much easier than that of 1,3-dihydroxy-2-propanone, which is present in a higher amount in the liquid phase.

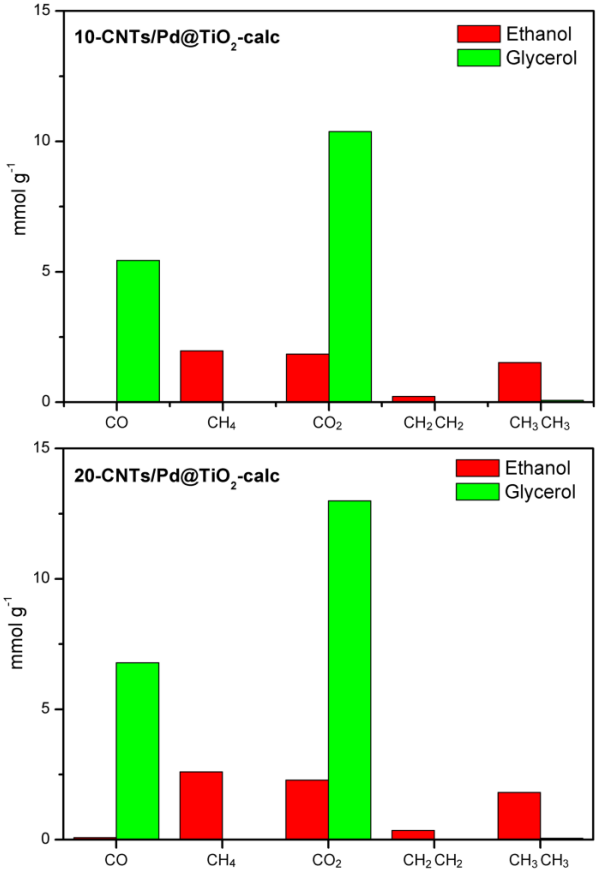

Figure 4.19: Amounts of by-products in the gas phase accumulated in 24 hours with **10-** and **20-CNTs/Pd@TiO₂-350** for the photoreforming of ethanol and glycerol.

Solar Simulated irradiation:

When irradiated with a simulated solar light, both **10-CNTs/Pd@TiO₂-350** and **20-CNTs/Pd@TiO₂-350** display an appreciable activity for the photoreforming of ethanol, although lower than the corresponding UV-irradiated samples (**Figure 4.20**).

When ethanol is used as sacrificial agent, the H_2 production reaches the value of 118 μmol m_{cat}^{-2} for **20-CNTs/Pd@TiO₂-350** catalyst after 24 hours under solar

illumination, while the photocatalyst with a lower CNTs content exhibits higher activity (140 μmol m_{cat}^{-2}). Both hybrid materials display a higher activity than the reference catalyst **Pd@TiO$_2$-350** (87 μmol m_{cat}^{-2}). However, it is worth noting that the CNTs-free material shows stable activity from the beginning of the experiment while the carbon/inorganic hybrids undergo a progressive activation over the initial 4 hours before reaching a constant H_2 evolution rate. By comparison, in the UV experiments this activation process is not observed reasonably because of the larger UV component of the irradiation that allows a faster elimination of residual organics moieties (very small amounts, negligible at TGA analysis) that still cover the Pd and CNT surfaces despite the thermal treatment.

On the other hand, when glycerol is employed as sacrificial donor the production of H_2 is only slightly higher (147 μmol $m_{cat}^{-2}$and 107 μmol m_{cat}^{-2}) for **10-CNTs/Pd@TiO$_2$-350** and **Pd@TiO$_2$-350** than **20-CNTs/Pd@TiO$_2$-350** (94 μmol m_{cat}^{-2}).

This suggests that the rate-determining step does not depend on the sacrificial electron donor or on the diffusion of the adsorbed protons from TiO_2 to the Pd sites. Rather, it must be associated with other factors such as the dispersibility of the catalysts in the different solution. This and other physical parameters can create differences in such small rates found under solar illumination.

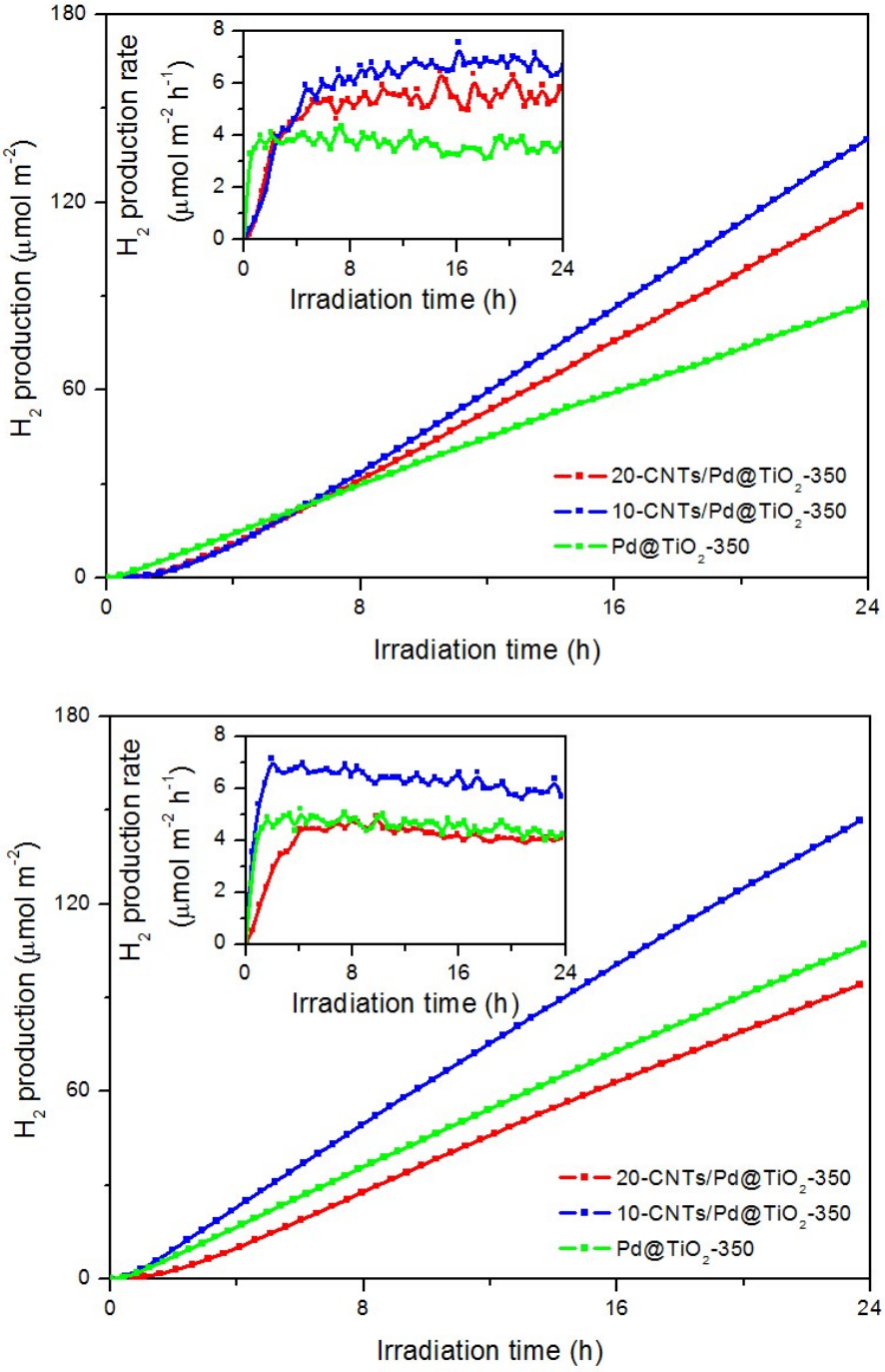

Figure 4.20: H_2 production over time under simulated solar illumination using aqueous solution of ethanol (left) and glycerol (right) as sacrificial donor. Activities are normalized by grams of catalyst.

The much lower productivity as compared to the UV experiments for both ethanol and glycerol sacrificial agents is easily explained in terms of the smaller UV content (4%) in the sun light, which represents the actual absorbed window of the light spectrum.

The analysis of the liquid phases collected after the ethanol photoreforming catalytic tests show, as expected, two main by-products, acetaldehyde and 1,1-

diethoxyethane (**Table 4.6**), which were also detected in the online analysis of the gaseous phases.

Table 4.6: Results from semi-quantitative analysis (1-butanol was used as internal standard) of liquid solutions collected after photocatalytic H_2 production from ethanol/water solutions under simulated solar irradiation.

	10-CNTs/Pd@TiO_2-350	**20-CNTs/Pd@TiO_2-350**	**Pd@TiO_2-350**
Acetaldehyde	0.22	0.18	0.68
1,1-diethoxyethane	0.39	0.23	0.20

On the other hand, when glycerol was employed, the analysis detected the expected first oxidation products (i.e. 1,3-dihydroxy 2-propanone, 1-hydroxy-2-propanone and hydroxyl-acetaldehyde) as main liquid by-products in analogy with the UV experiment (**Table 4.7**).

Table 4.7: Results from semi-quantitative analysis (1-hexanol was used as internal standard) of liquid solutions collected after photocatalytic H_2 production from glycerol/water solutions under simulated solar irradiation.

	10-CNTs/Pd@TiO_2 - 350	**20-CNTs/Pd@TiO_2 - 350**	**Pd@TiO_2-350**
Hydroxy-acetaldehyde	1.04	1.14	1.40
1-hydroxy-2-propanone	0.10	0.15	0.14
2,3-dihydroxypropanal	0.16	0.21	0.18
1,3-dihydroxy-2-propanone	1.18	1.30	1.53

4.5 CONCLUSIONS

In conclusion the TiO_2-based photocatalysts presented in this chapter have shown outstanding activities in H_2 production from photoreforming of alcohols. This must due to the achievement of the designed hierarchical nanostructure and the benefits given by the new synthetic protocol and the specific thermal treatment.

The positive effect of the presence of the carbon scaffold is corroborated by the comparison of the activities of the hybrid catalysts with the reference carbon-free analogue. The higher performance of the former, also normalized by the surface area, suggests an electronic effect of the carbon nanotube, presumably associated with its capability to act as electron scavenging thus retarding charge carrier recombination.

The catalysts also show good activity and stability under solar irradiation.

PART 2: Carbon NanoCones-based materials

4.6 CATALYST DESIGN

Following the knowledge gained during the assembly of the hierarchical materials based on MWCNTs (see Chapter 3 and Chapter 4 Part 1), the attention was extended to another nanocarbon structure, namely carbon nanocones, which has been comparatively much less investigated. The strategy for the final hybrid was similar to that described in the previous part, with the difference that the nanocones were oxidized prior to their hybridization with the Pd@TiO_2. Such oxidized nanocones, which were supplied by the Norwegian company n-Tec, turn out to have a better dispersibility in liquid media than the functionalized nanotubes, giving rise to a maximization of the homogeneity of the coating by the inorganic shell.

4.7 CATALYST PREPARATION

The TiO_2-based materials employed as catalysts for the photoreforming of alcohols were assembled starting from three building blocks: *i*) oxidized carbon nanocones (ox-CNCs); *ii*) palladium nanoparticles protected by mercapto-undecanoic acid (Pd-MUA); *iii*) titanium (IV) *n*-butil alkoxide (Ti(O-*n*-Bu)$_4$). The building blocks were then assembled to obtain the final material. The overall process is schematically illustrated in **Figure 4.21**.

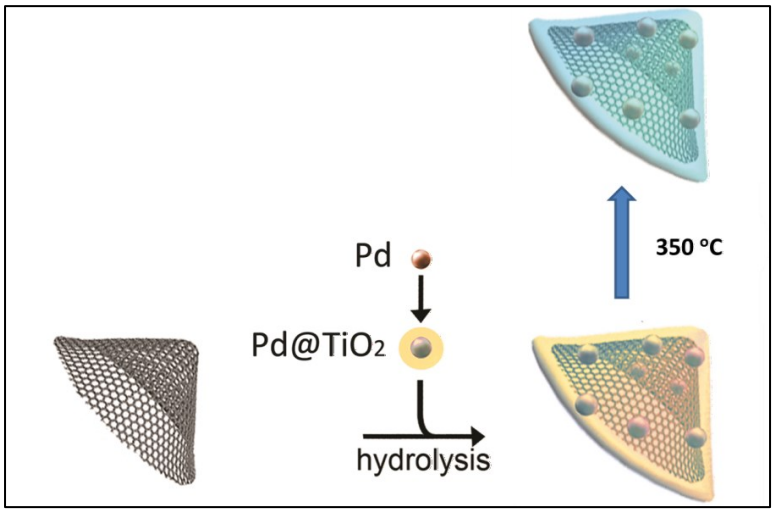

Figure 4.21: General synthetic scheme of hierarchical CNCs/Pd@TiO_2.

The ox-CNCs were supplied by n-Tec Company. For the synthesis of the Pd-MUA see paragraphs 3.3.2. The Ti(O-*n*-Bu)$_4$ was purchased from Sigma-Aldrich.

A material with CNCs 20 % wt and Pd 1 % wt nominal compositions (relative to the nominal final composition) has been prepared and labelled **ox-CNCs/Pd@TiO$_2$.** Part of the material was then subjected to a thermal treatment at 350 °C yielding the calcined sample labelled **ox-CNCs/Pd@TiO$_2$-350**

4.7.1 Hybrid synthesis (CNCs/Pd@TiO$_2$)

A given amount of ox-CNCs (chosen in order to have a 20 wt% relative to the nominal final composition) were dispersed in absolute ethanol (reaching 2 mg/mL concentration) by sonication (30 minutes). Meanwhile, the Pd@TiO$_2$ precursors were assembled by slowly adding a THF solution of previously prepared Pd-MUA to an absolute ethanol solution of Ti(n-OBu)$_4$, as reported in paragraph 3.3. The as-prepared Pd@TiO$_2$ precursors were then added dropwise to the CNCs dispersion and the mixture sonicated for further 30 minutes. After this time, a 10% solution of H_2O in absolute ethanol (Ti(O-*n*-Bu)$_4$/H_2O molar ratio equal to 1/120) was slowly added dropwise, followed by 30 minutes of sonication. The solid was filtered through a 0.45 μm PTFE filter and washed with ethanol. The product was recovered and dried at 85°C overnight (**ox-CNCs/Pd@TiO$_2$**). Part of the product was subjected to calcination at 350°C for 5 hours, and labelled **ox-CNCs/Pd@TiO$_2$-350**. As a comparison, two catalysts not featuring either CNCs, labelled **Pd@TiO$_2$-350**, or Pd, labelled **ox-CNCs/TiO$_2$-350** were also prepared using the same synthetic approach but in absence of the respective component.

4.8 CHARACTERIZATION AND RESULTS

The correct assembly of the hybrid catalyst and the intimate contact between the nanocarbon structures and the inorganic matrix were corroborated through different techniques. It is noteworthy that the Pristine CNCs are not available for characterization since the pristine materials were not supplied by n-Tec.

4.8.1 Thermogravimetric analysis

The thermogravimetric analysis in air was used to determine the final carbon/inorganic weight ratios of the prepared materials (**Figure 4.22**). The **ox-CNCs** presents a first broad weight loss due to the removal of the functional groups (mainly COOH) at 200 – 450 °C and a well define second loss corresponding to the completely burning of the carbon scaffold starting at ~ 600 °C. In contrast, the fresh hybrid **ox-CNCs/Pd@TiO$_2$** exhibits two well defined weight losses, the first at 150 – 350 °C and the second at ~ 500 °C. The former can be attributed again to the combustion and removal of organic ligands residues of the sol-gel synthesis (i.e. MUA and butanol) and H_2O trapped in the inorganic network. The second is due to the completely burning of the carbonaceous scaffold. The decrease in combustion temperature with respect to the **ox-CNCs** must be due to a catalytic effect of the inorganic matrix, implying a tight contact between the components of the hybrid. Finally, in the calcined hybrid **ox-CNCs/Pd@TiO$_2$-350**, the first weight loss is no longer present, as expected given that the COOH functionalities had been removed during calcination, while the residual inorganic matrix accounts for ~ 80%, in good agreement with the nominal composition.

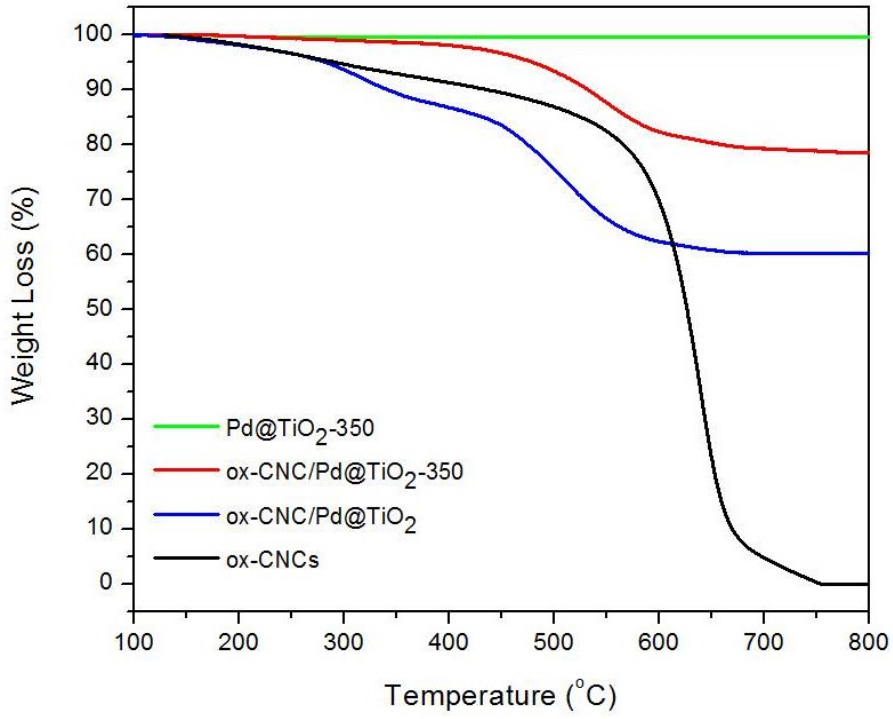

Figure 4.22: Thermogravimetric analysis of the material under air. The red vertical line indicates the calcination temperature (350 °C) of the fresh material.

4.8.2 Structural analysis

The Raman spectra of all the analyzed samples (**Figure 4.23**) shows the characteristic G band at (~ 1590 cm^{-1}), due to the in-plane vibrational mode of the sp^2 graphitic framework, and the defected-induced D band at (~ 1350 cm^{-1}) of the CNCs structure, while its broad second-order harmonic (2D band) at 2500 – 3100 cm^{-1} which can be deconvoluted into two-peaks, suggesting a stacking process of the CNCs, as reported in the literature for graphene.[167] The ratio between the D band and the G band (I_D/I_G), equal to 0.97 in the **ox-CNCs**, decrease to 0.93 in the **ox-CNCs/Pd@TiO₂** after the hybridization with the inorganic shell. This apparent healing of the π framework was exhaustively explained in paragraph 3.4.2 as a perturbation of the D signal of the outer graphitic layer by the inorganic shell, which further confirms the thigh contact between the carbon and the inorganic matrix.[130] The **ox-CNCs/Pd@TiO₂** sample presents no additional peak, suggesting the amorphous nature of the TiO_2 shell. On the other hand, the calcined **ox-CNCs/Pd@TiO₂-350** sample presents the six vibration modes characteristic of the anatase polymorph of the TiO_2,[147] corroborating the crystallization after the thermal treatment.

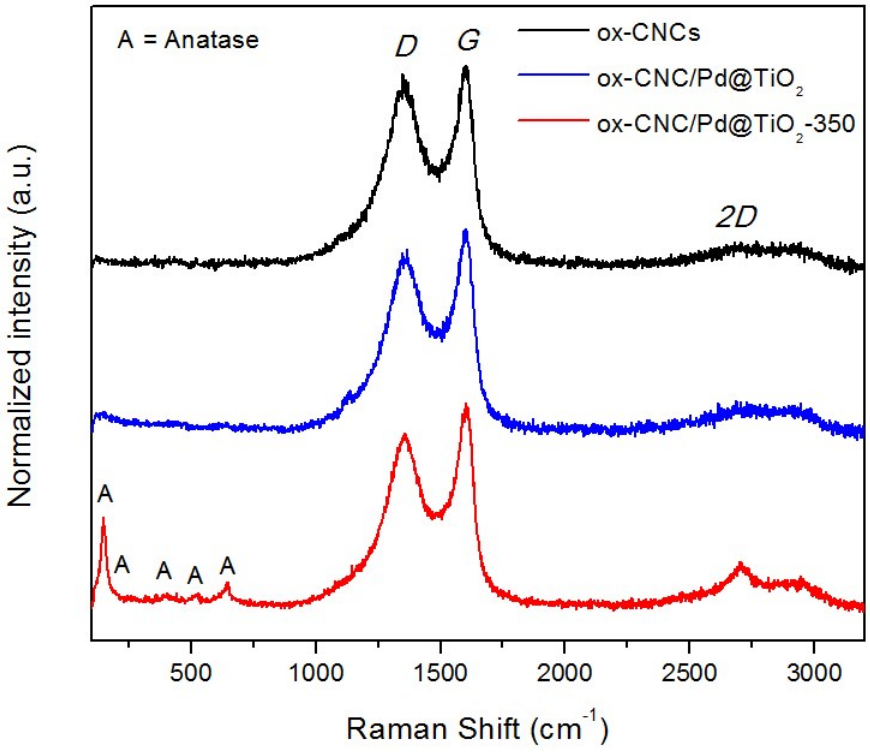

Figure 4.23: Raman spectra of **ox-CNCs/Pd@TiO₂-350**, **ox-CNCs/Pd@TiO₂** and **ox-CNCs**.

The XRD pattern of the calcined hybrid shows the characteristic reflection of the anatase phase of the TiO_2 (**Figure 4.24**) and presents an average crystallite size of 11 nm, calculated by applying the Scherrer's equation (**Eq. 2.7**) to the main reflection (101). Noteworthy the characteristic reflection of the graphitic framework of CNCs (26.6 °) is not distinguishable because of the overlapping high intensity of the main reflection of anatase (25.3 °). Regarding the Pd nanoparticles, a very weak reflection around 33.5° is observed and it can be related to the PdO formed after the thermal treatment.

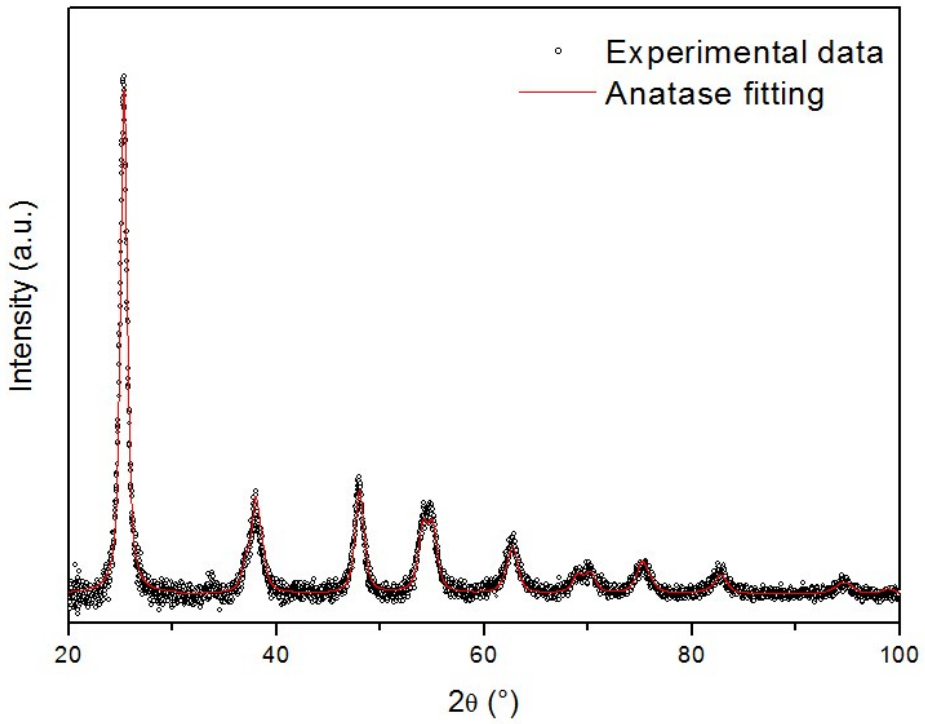

Figure 4.24: Powder XRD pattern of the **ox-CNCs/Pd@TiO₂-350** samples calcined in air at 350 °C.

4.8.3 Morphological analysis

Transmission electron micrographs (TEM analysis) show that the **ox-CNCs** sample is actually composed by a mixture of structures with different geometrical parameters ranging from disks to cones (**Figure 4.25** A and B). This is expected as an approximate composition of 20% cones, 70% disks and 10% amorphous carbon was declared by the supplying company. In particular, it has been shown that the width of the cone angle can assume different distinct values, ranging from ~ 19° to ~150°, with the latter implying a disk-like shape.[86] Regardless of the cone angle and therefore of the

particular morphology, TEM displays a very homogeneous coverage with an inorganic shell. (**Figure 4.25** C and D).

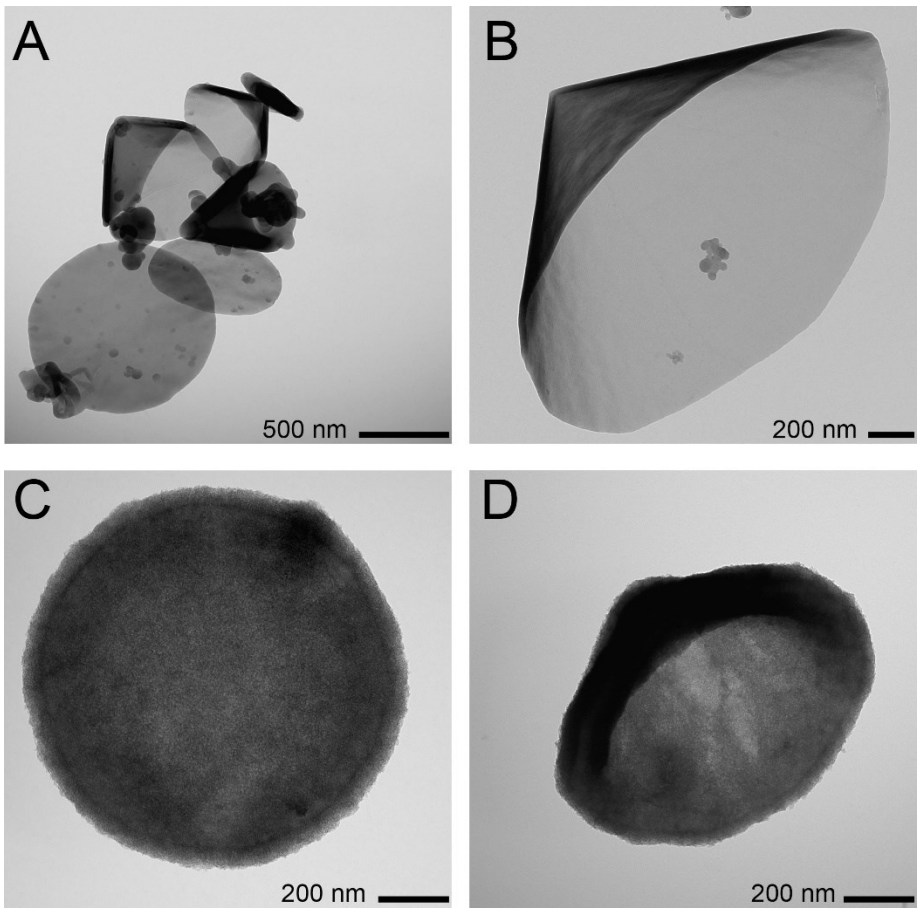

Figure 4.25: Representative HR-TEM of the **ox-CNCs** sample with cone and disk morphology (A and B) and the **ox-CNCs/Pd@TiO₂** sample in both disk (C) and cone morphology (D).

Because of their small size (nominally 2 nm) and the surrounding TiO_2 shell, the Pd nanoparticles are not easily detectable by standard TEM micrographs. However, EDX mapping clearly detects each individual element (C, Ti, O and Pd), confirming the correct assembly of the carbon/inorganic hybrid, the intimate contact between the three components and the presence of Pd nanoparticles into the TiO_2 shell (**Figure 4.26**).

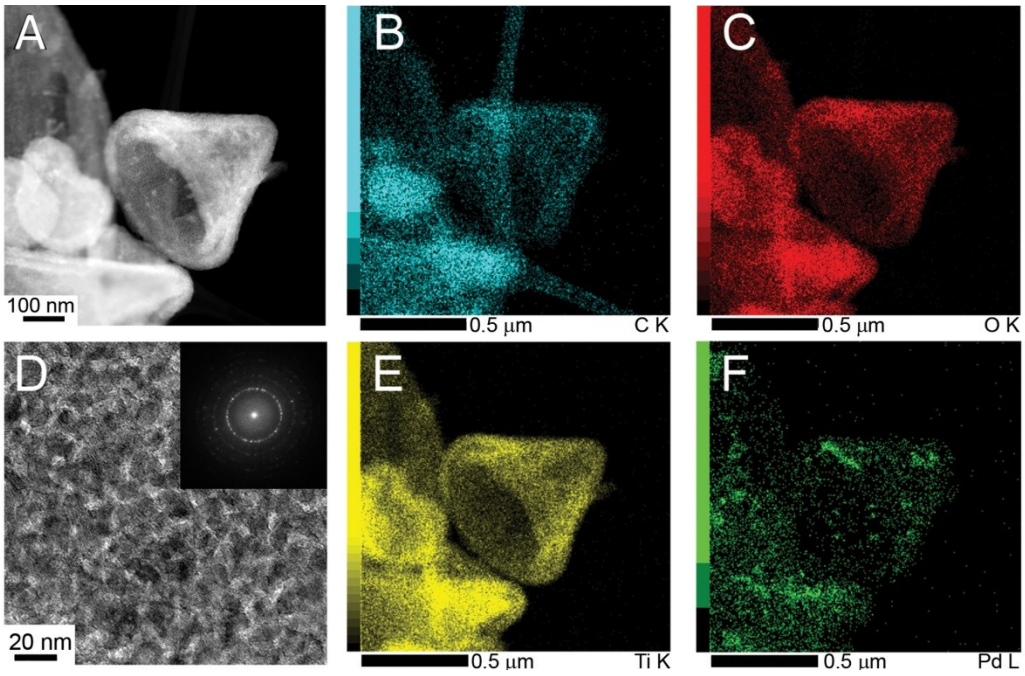

Figure 4.26: Representative HAADF-STEM of **ox-CNCs/Pd@TiO2-350** (A) and HR-TEM area expansion showing anatase phase (D) as confirmed by corresponding Fast Fourier Transform (inset). Representative EDX mapping showing carbon (B), oxygen (C), titanium (E) and palladium (F).

Presence of distinct Pd nanoparticles was also corroborated by HR-TEM and the corresponding Fast Fourier Transform (FFT) of a selected area (SAED) showing spots identified with TiO_2 anatase phase and Pd (**Figure 4.27**) in **ox-CNCs/Pd@TiO$_2$-350**. A carefully analysis of the TiO_2 particles revealed an approximate size range of 6-9 nm.

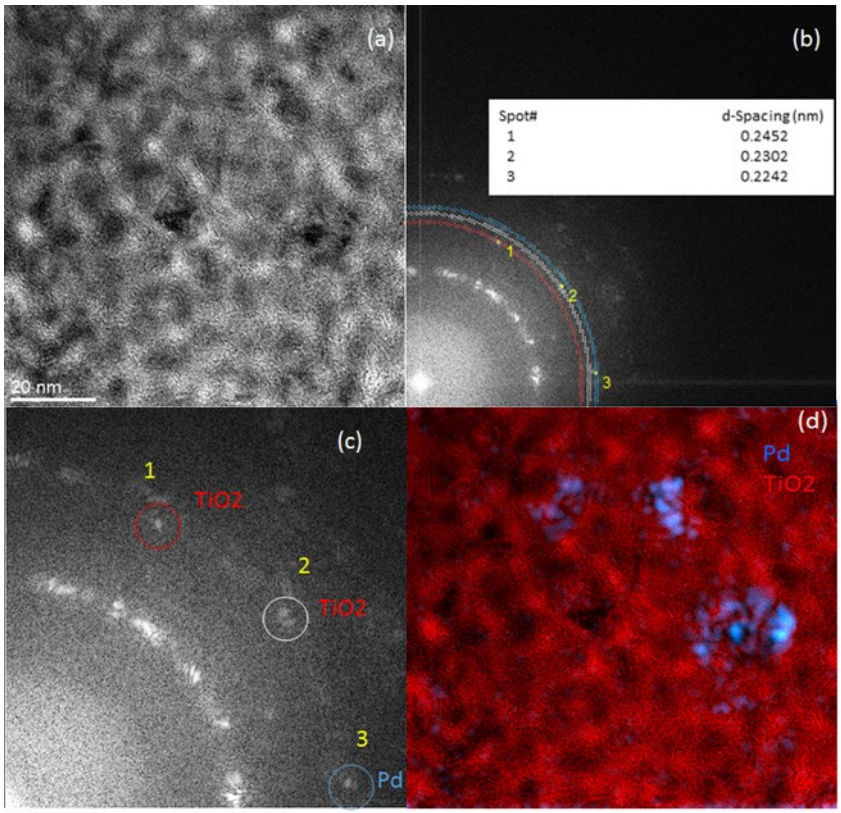

Figure 4.27: a) HRTEM image of **CNCs/Pd@TiO$_2$-350**; b, c) corresponding FFT showing spots corresponding to the TiO_2 anatase phase and Pd; d) color map displaying the inverse FFT generated by selecting the diffraction spots of TiO_2 (red) and Pd (blue).

4.8.4 Textural analysis

The N_2 physisorption isotherms collected at liquid nitrogen temperature and the pore size distribution of the investigated materials show significant differences (**Figure 4.28**), resulting from the different textural properties (**Table 4.8**). According to the IUPAC recommendations,[94] the **ox-CNCs** show Type II isotherm, typical of non-porous/macroporous materials. The surface area, as calculated by the BET model, is relatively low while the pore size distribution analysis reveals macropores around 100 nm. This behavior agrees with packing of the CNCs that mainly causes the diminution of the surface area.

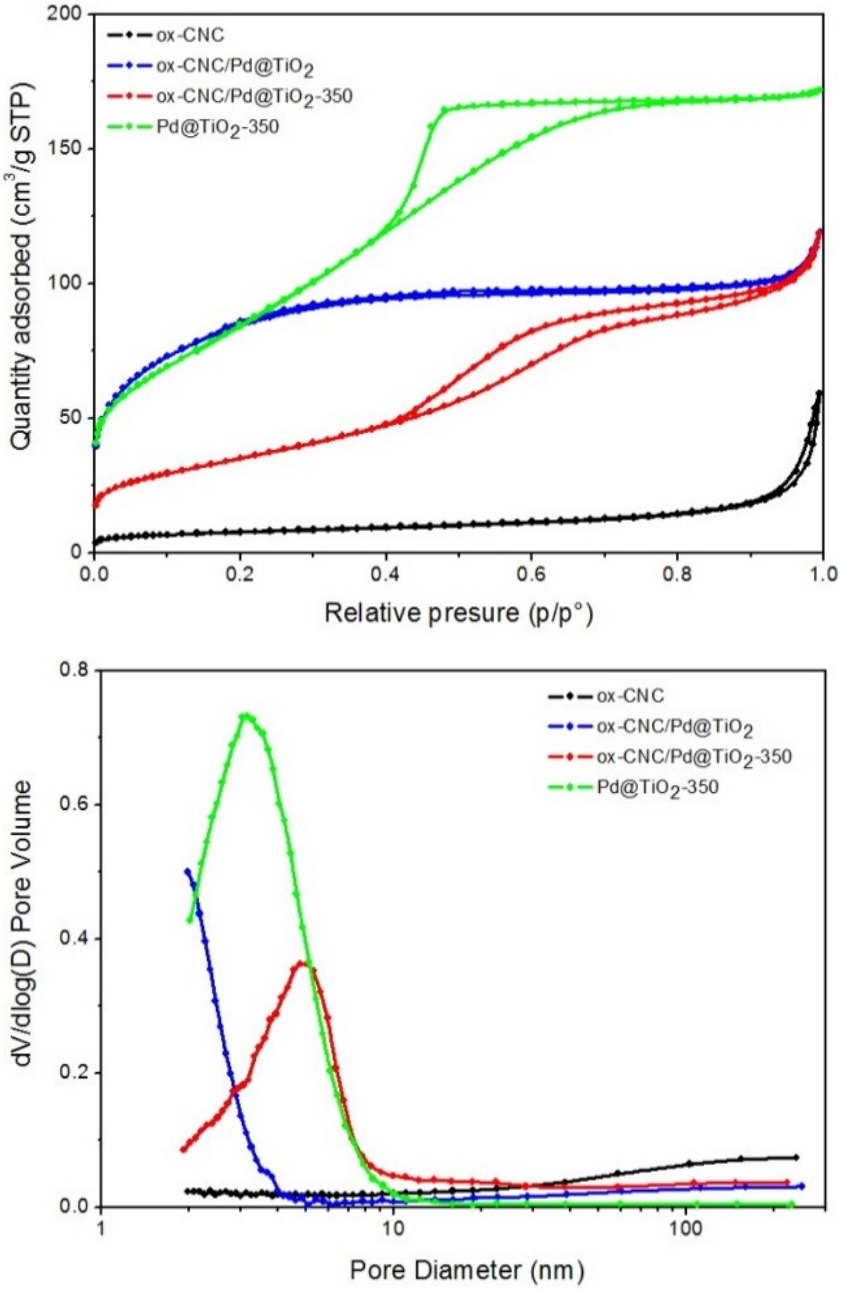

Figure 4.28: N_2 physisorption isotherms (on the top) and BJH pore size distribution calculated on the adsorption branches (on the bottom) of the materials.

The hybridization of the carbonaceous scaffold with Pd@TiO_2 layer completely changes the textural properties: the **ox-CNCs/Pd@TiO_2** sample shows a Type I isotherm, typical of microporous materials and present a pore size distribution extending to the lower part of the mesoporous limit (i.e. 2 nm). As result, an important increase in the surface area can be observed, in spite of the modest cumulative pore volume increase. It is reasonable that the microporous network is due to the Pd@TiO_2 gel covering the

carbon scaffold. On the other hand, the thermal treatment and the subsequent crystallization of the inorganic matrix forms an extended mesoporous network in the **ox-CNCs/Pd@TiO$_2$-350** sample, whose isotherm is of type IV. However, in this case the surface area is much lower than that before calcination but, most importantly, pore size and volume are significantly increased.

Table 4.8: Summary of the textural properties of the investigated materials from N_2 physisorption measurements.

Sample	Pd@TiO$_2$-350	Ox-CNCs	Ox-CNCs/Pd@TiO$_2$	Ox-CNCs/Pd@TiO$_2$-350
Type of isotherm [a]	IV	II	I	IV
Specific Surface Area (m^2/g)	323	25 [b]	248 [c]	126 [b]
Cumulative Pore Volume (mL/g)	0.295	0.089 [d]	0.112 [e]	0.192 [d]
D_{max} (nm) [f]	3.2	> 200	< 2	4.9

[a] accordingly to IUPAC recommendation;[94]
[b] calculated using the BET equation;
[c] calculated using the Langmuir equation;
[d] calculated from the BJH analysis of the adsorption branch of the N_2 physisorption isotherms;
[e] calculated from the adsorbed volume at p/p° = 0.90;
[f] maximum of the pore size distribution obtained applying the BJH analysis to the adsorption branch of the N_2 physisorption isotherms, as reported in **Figure 4.27**.

4.8.5 Catalytic results

The catalytic activity of the two materials **CNCs/Pd@TiO$_2$** and **CNCs/Pd@TiO$_2$-350** was evaluated in the H_2 production from an aqueous solution of ethanol 50% *v/v* under UV-vis irradiation and simulated Sunlight. Their performance was compared to that of the reference **Pd@TiO$_2$-350** catalyst. The reported production of H_2 over time are normalized over the surface area of the specific sample, in order to rule out a mere geometrical effect in favour of an electronic effect brought by the CNCs.

UV-vis irradiation:

The calcined **ox-CNCs/Pd@TiO$_2$-350** sample presents an outstanding H_2 production (**Figure 4.29**) of 5 mmol m_{cat}^{-2} after 20h (corresponding to 600 mmol g_{cat}^{-1}) and a quantum efficiency (QE) of 12.3 %. Indeed, the fresh **ox-CNCs/Pd@TiO$_2$** catalyst shows a much lower activity (~0.5 mmol·m_{cat}^{-2}). An obviously explanation for this stark difference is the crystallization of the TiO_2 shell that is well known to enhance the photoresponse, as also reported for the MWCNTs-based materials (see paragraph 4.4.6). Comparatively, the CNCs-free material **Pd@TiO$_2$-350** has an activity significantly lower than the final nanohybrid. Moreover, the stability **ox-CNCs/Pd@TiO$_2$-350** catalyst is very pronounced, with evolution rates fully retained over the initial 10 hours of irradiation, before undergoing slight deactivation, presumably due to partial aggregation of the material.

The presence of acetaldehyde and 1,1-diethoxyethane was detected as by-products together with H_2 in both the gas and liquid phases while CH_4 and CO_2 are observed only in traces. This behavior suggests that the full mineralization of ethanol is disadvantaged due the stronger adsorption onto the TiO_2 of ethanol respect to acetaldehyde, as previously demonstrated.[155]

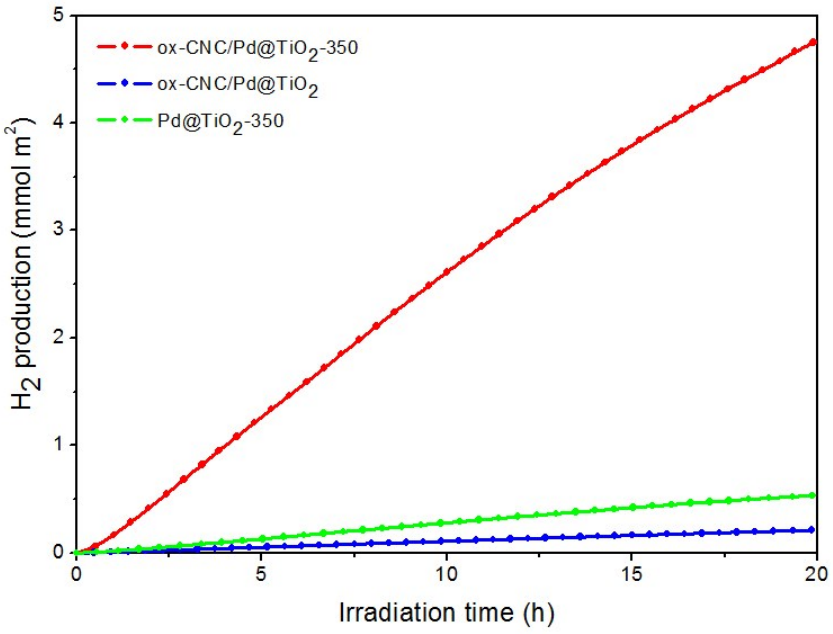

Figure 4.29: H_2 production over time by **ox-CNCs/Pd@TiO₂**, **ox-CNCs/Pd@TiO₂-350** and **Pd@TiO₂-350** normalized by the initial surface area of the catalyst under UV-Vis irradiation.

There is a synergistic positive effect in the catalytic activity of the Pd@TiO_2 inorganic matrix due to the thermal treatment and the hybridization with the CNCs, which provides an extremely proficient electron scavenging thus retarding charge carrier recombination.

Furthermore when the Pd-free catalyst (**ox-CNCs/TiO₂-350**) was employed, only negligible amounts of H_2 were detected, confirming the essential role of Pd as truly catalytic site for the proton reduction to H_2.

The CNC-based catalyst is also comparatively superior to the CNT-based catalysts discussed in Chapter 4 Part 1. This highlights the highly promising use of the CNCs nanostructure, with improved activity attributed to the more efficient and uniform contact between the carbon scaffold and the inorganic matrix, as a result of the better dispersibility during the hybridization of CNCs with the Pd@TiO_2 precursors. This causes an increased number of heterojunctions, which has been shown to be an important parameter to improve performance.[153]

To further corroborate the outstanding performance of the **ox-CNCs/Pd@TiO₂-350** hybrid catalyst, recyclability tests were carried out, recovering the catalyst by filtration after 20 hours under UV-vis irradiation and subsequently re-dispersing it in a

fresh aqueous solution of ethanol 50 % *v/v*. The recyclability was evaluated over three catalytic experiments. After the first cycle, a small deactivation is observed when the H_2 production is calculated per gram of catalyst. On the other hand the second and the third cycles show almost identical activities. It is reasonable to hypothesize that a partial modification of the catalyst occurs during the UV irradiation. Indeed a decrease of ~20% of the surface area was observed by N_2 physisorption measurement of the catalyst collected after the recyclability test and associated to the deactivation process. When normalized by the surface area, the catalytic activity is much more stable through all the three cycles (**Figure 4.30**).

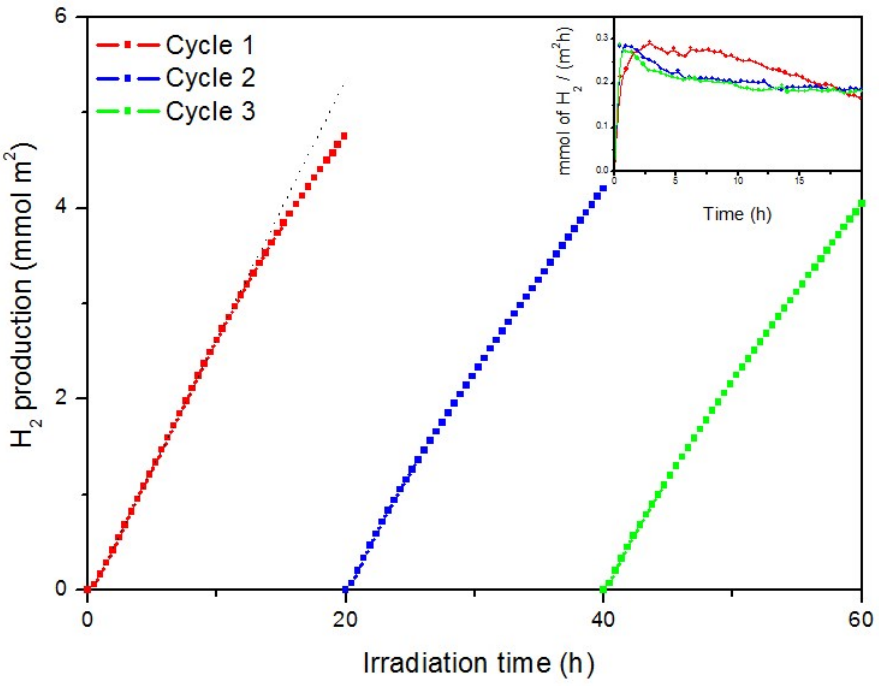

Figure 4.30: Catalytic activity (normalized by the catalysts initial surface area) of **ox-CNCs/Pd@TiO$_2$-350** over three different cycles. The black dotted line represents the theoretical activity if no deactivation processes were in place and it can be used as guide.

Simulated Sunlight irradiation:

Testing the catalysts under simulated solar irradiation also resulted in appreciable H_2 production (**Figure 4.31**). Coherently, the most performant material is **ox-CNCs/Pd@TiO$_2$-350** which shows an activity as high as 0.25 mmol·m_{cat}^{-2} (corresponding to 32 mmol·g_{cat}^{-1}) and a long stability over time. While the fresh catalyst exhibited a non-detectable activity under these conditions.

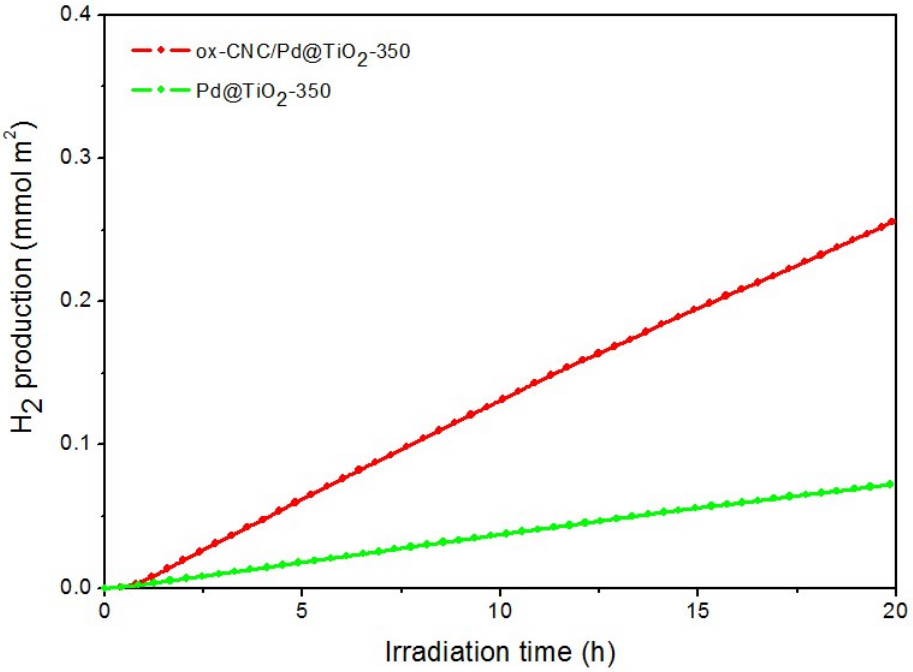

Figure 4.31: H_2 production over time by **ox-CNCs/Pd@TiO₂-350** and **Pd@TiO₂-350** normalised by the initial surface area of the catalysts under Solar Simulated illumination. No activity was detected with **ox-CNCs/Pd@TiO₂** under the catalytic conditions.

Also in this case the activity is comparatively superior to the CNT-based catalysts discussed in Chapter 4 Part 1.

4.9 CONCLUSIONS

In conclusion, this part of the PhD work reports the very first example of hybrid photocatalyst hierarchically based on CNCs and Pd@TiO_2.

The desired design and composition of the materials were obtained and confirmed by several techniques. An outstanding activity in H_2 evolution was achieved by photoreforming of aqueous solution of ethanol, ranking the catalyst amongst the most efficient ever reported with carbon-based supports. The hybrid catalyst also exhibits a good stability under recyclability tests.

The enhancement of activity of the carbon/inorganic hybrid photocatalysts is mainly related to the capability of the carbon framework to act as electron scavenging thus retarding charge carrier recombination. However, because of the lower conductivity of CNCs relative to CNTs, the pronounced activity must be related to other

characteristics, such as the high dispersibility of the CNCs during the assembling of the hybrid catalyst resulting in an optimum homogeneity of the final catalyst structures. The maximized areas of contact of the carbon and inorganic matrix cause an increased number of heterojunctions, responsible for the higher activity.

The catalysts also show good activity and stability under simulated solar irradiation, propelling them as promising candidates for solar devices development.

Chapter 5

CONCLUSIONS

The main aim of this research project is the development of hybrid nanomaterials to improve the performance of two important environmental and energy-involved processes: the Water Gas Shift Reaction and the photocatalytic production of solar fuels such as hydrogen via photoreforming of renewable oxygenated compounds obtained from biomasses (i.e. ethanol and glycerol). In particular, ternary hybrids comprising nanocarbon scaffolds, metal oxide and metal nanoparticles were prepared to achieve these purposes. A hierarchical synthetic approach was chosen to better integrate the properties of each component in the hybrid material. A series of carbon/inorganic hybrids with new properties with respect to the single components were prepared and the effect of their composition and properties has been evaluated with respect to their catalytic performances.

Efforts have focused on the improvement of the activity of the prepared catalyst by seeking, during the assembling of the hybrid catalyst, a high and homogeneous coverage of the nanocarbon structures with the inorganic matrix, an intimate contact between the phases and the preservation of the properties of each component. Tailored post-synthetic thermal treatments were used in order to enhance the catalytic activity. Moreover, the role of the nanocarbon structure was studied correlating the activities of the hybrid catalysts with their composition

The components of the ternary hybrid catalysts were chosen depending on the required properties to accomplish the desired reactions. Regarding the WGSR studies, CeO_2 was chosen as main component of the inorganic matrix. Its role is to act as co-catalyst of the active phase, which consists of Pd nanoparticles. On the other hand, the production of hydrogen was carried out employing TiO_2 as photocatalyst deposited over the carbonaceous scaffold, while Pd nanoparticles were acting as co-catalyst.

Multi-walled carbon nanotubes were the first scaffolds tested in this study. In the envisioned synthetic strategy, the nanocarbon building block must act as a scaffold for

templating 1D growth of the inorganic matrix. In order to secure a firm attachment of Pd@MO_2 units, the MWCNTs were adequately equipped with anchoring groups that can bind to the metal precursors of the oxide shell. Such groups also aid dispersibility (and therefore liquid phase manipulation) of the MWCNTs. The covalent attachment of the functional groups (benzoic acid) has been performed through an optimized reported radical reaction instead of classical oxidation treatment, that notoriously introduce large amounts of defects in the carbon nanostructures, worsening their electronic properties.

CNTs/Pd@CeO_2 and CNTs/Pd@TiO_2 hybrids were successfully assembled and characterized by several structural and morphological techniques. Structural analysis (by powder XRD) evidenced the formation of the desired phase in the oxide shell in the form of nanostructured crystals. Textural analysis (by N_2 physisorption) revealed the formation of extended micro/mesoporous systems within the hybrid materials, with good accessibility of the Pd nanoparticles embedded into the oxide shell (as revealed by chemisorption analysis). Advanced TEM investigations confirmed the nanocrystalline nature of the shell and the intimate contact between the carbon nanostructures and the inorganic matrix, allowing to identify the best composition that minimize the formation of free-standing inorganic matrix.

As far as the WGSR is concerned, the best performance in terms of activity and stability was reached by the hybrid with the optimum coverage of inorganic matrix. The catalytic results, corroborated by the measurements of the textural properties, show that integration of MWCNTs into core-shell Pd@CeO_2 catalysts have a positive impact in terms activity and stability. Due to its electronic properties, the MWCNTs component results to have an important role as stabilizing agent by disfavoring the deactivation mechanism of the inorganic matrix.

Regarding the H_2 production, the prepared hybrid photocatalysts have shown outstanding activities in the photoreforming of biomass derived alcohols (i.e. ethanol and glycerol). The benefits given by the presence of the MWCNTs were associated to its capability to act as electron scavenging, thus retarding charge carrier recombination. Moreover, the materials were found to have a good activity under Solar irradiation.

Once optimized both the synthetic and the post-synthesis treatment protocols, the second step involved the testing of another carbon nanostructure as carbon scaffold, namely carbon nanocones (CNCs), which were coated with Pd@TiO_2 layers. This work

reports the very first example of hybrid photocatalyst hierarchically based on CNCs, which present an outstanding activity in the production of H_2 from ethanol photoreforming an good stability under recycling tests. The pronounced activity was related to the high dispersibility of the CNCs during the assembling of the hybrid catalyst resulting in an optimum homogeneity of the final catalyst structures. Maximizing the contact areas of the nanocarbon structures and the inorganic matrix, an increased number of heterojunctions, responsible for the higher activity, are created. Moreover the CNCs/Pd@TiO_2 catalyst present a good activity under Solar irradiation.

REFERENCES

(1) International Energy Agency. Key World Energy Statistics. **2016**.

(2) Intergovernmental Panel on Climate Change. “Climate Change 2013: The Physical Science Basis.”

(3) World Meteorological Organization. “WMO Statement on the Status of the Global Climate in 2015.”

(4) British Petroleum. Statistical Review of World Energy. **2016**.

(5) Nocera, D. G. Chemistry of Personalized Solar Energy. *Inorg. Chem.* **2009**, *48*, 10001–10017.

(6) Sharaf, O. Z.; Orhan, M. F. An Overview of Fuel Cell Technology: Fundamentals and Applications. *Renew. Sustain. Energy Rev.* **2014**, *32*, 810–853.

(7) Zhang, J.; Xie, Z.; Zhang, J.; Tang, Y.; Song, C.; Navessin, T.; Shi, Z.; Song, D.; Wang, H.; Wilkinson, D. P.; Liu, Z.-S.; Holdcroft, S.. High Temperature PEM Fuel Cells. *J. Power Sources* **2006**, *160*, 872–891.

(8) Giddey, S.; Badwal, S. P. S.; Kulkarni, A.; Munnings, C. A Comprehensive Review of Direct Carbon Fuel Cell Technology. *Prog. Energy Combust. Sci.* **2012**, *38*, 360–399.

(9) Badwal, S. P. S.; Giddey, S.; Kulkarni, A.; Goel, J.; Basu, S. Direct Ethanol Fuel Cells for Transport and Stationary Applications – A Comprehensive Review. *Appl. Energy* **2015**, *145*, 80–103.

(10) Ramachandran, R.; Menon, R. K. An Overview of Industrial Uses of Hydrogen. *Int. J. Hydrogen Energy* **1998**, *23*, 593–598.

(11) Schlapbach, L.; Züttel, A. Hydrogen-Storage Materials for Mobile Applications. *Nature* **2001**, *414*, 353–358.

(12) Carcassi, M. N.; Fineschi, F. Ã. Deflagrations of H_2 – Air and CH_4 – Air Lean Mixtures in a Vented Multi-Compartment Environment. *Energy* **2005**, *30*, 1439–1451.

(13) Tromp, T. K.; Shia, R.; Allen, M.; Eiler, J. M.; Yung, Y. L. Potential Environmental Impact of a Hydrogen Economy on the Stratosphere. *Science* **2003**, *300*, 1740–1743.

(14) IUPAC Gold Book "Composition of Pure Air."

(15) Ogden, J. M. Prospects for Building a Hydrogen Energy Infrastructure. *Proc. 8th Natl. Hydrog. Assoc. Meet. Arlington, VA, March 3-5, 1998; Natl. Hydrog. Assoc. Washington, DC,* **1999**.

(16) Navarro, R.; Pena, M.; Fierro, J. Hydrogen Production Reactions from Carbon Feedstocks: Fossil Fuels and Biomass. *Chem. Rev.* **2007**, *107*, 3952–3991.

(17) Satterfield, C. N. *Heterogeneous Catalysis in Industrial Practice, 2nd Ed.; McGraw-Hill: New York*; 1991.

(18) Acres, G. J. K.; Frost, J. C.; Hards, G. A.; Potter, R. J.; Ralph, T. R.; Thompsett, D.; Burstein, G. T.; Hutchings, G. J. Electrocatalysts for Fuel Cells. *Catal. Today* **1997**, *38*, 393–400.

(19) Takenaka, S.; Shimizu, T.; Otsuka, K. Complete Removal of Carbon Monoxide in Hydrogen-Rich Gas Stream through Methanation over Supported Metal Catalysts. *Int. J. Hydrogen Energy* **2004**, *29*, 1065–1073.

(20) Kulprathipanja, A.; Alptekin, G. O.; Falconer, J. L.; Way, J. D. Effects of Water Gas Shift Gases on Pd-Cu Alloy Membrane Surface Morphology and Separation Properties. *Ind. Eng. Chem. Res.* **2004**, *43*, 4188–4198.

(21) Oh, S. H.; Sinkevitch, R. M. Carbon Monoxide Removal from Hydrogen-Rich Fuel Cell Feedstreams by Selective Catalytic Oxidation. *J. Catal.* **1993**, *142*, 254–262.

(22) Valenti, G.; Boni, A.; Melchionna, M.; Cargnello, M.; Nasi, L.; Bertoni, G.; Gorte, R. J.; Marcaccio, M.; Rapino, S.; Bonchio, M.; Fornasiero, P; Prato, M.; Paolucci, F. Co-Axial Heterostructures Integrating Palladium/titanium Dioxide with Carbon Nanotibes for Efficient Electrocatalytic Hydrogen Evolution. *Nat. Commun.* **2016**, *7*, 1–8.

(23) Donitz, W.; Erdle, E. High-Temperature Electrolysis of Water Vapor - Status of Development and Perspectives for Application. *Int. J. Hydrogen Energy* **1985**, *10*, 291–295.

(24) Arashi, H.; Naito, H.; Miura, H. Hydrogen production from high-temperature steam electrolysis using solar energy. *Int. J. Hydrogen Energy* **1991**, *16*, 603–608.

(25) Chen, Y. X.; Lavacchi, A.; Miller, H. A.; Bevilacqua, M.; Filippi, J.; Innocenti, M.; Marchionni, A.; Oberhauser, W.; Wang, L.; Vizza, F. Nanotechnology Makes Biomass Electrolysis More Energy Efficient than Water Electrolysis. *Nat. Commun.* **2014**, *5:4036*.

(26) Sarkar, N.; Ghosh, S. K.; Bannerjee, S.; Aikat, K. Bioethanol Production from Agricultural Wastes: An Overview. *Renew. Energy* **2012**, *37*, 19–27.

(27) Romaní, A.; Garrote, G.; Ballesteros, I.; Ballesteros, M. Second Generation Bioethanol from Steam Exploded Eucalyptus Globulus Wood. *Fuel* **2013**, *111*, 66–74.

(28) Balat, M. Production of Bioethanol from Lignocellulosic Materials via the Biochemical Pathway: A Review. *Energy Convers. Manag.* **2011**, *52*, 858–875.

(29) Fujishima, A.; Honda, K. Electrochemical Photolysis of Water at a Semiconductor Electrode. *Nature* **1972**, *238*, 37–38.

(30) Hisatomi, T.; Kubota, J.; Domen, K. Recent Advances in Semiconductors for Photocatalytic and Photoelectrochemical Water Splitting. *Chem. Soc. Rev.* **2014**, *43*, 7520–7535.

(31) Reece, S. Y.; Hamel, J. a; Sung, K.; Jarvi, T. D.; Esswein, a J.; Pijpers, J. J. H.; Nocera, D. G. Wireless Solar Water Splitting Using Silicon-Based Semiconductors and Earth-Abundant Catalysts. *Science,* **2011**, *334*, 645–648.

(32) Kudo, A.; Miseki, Y. Heterogeneous Photocatalyst Materials for Water Splitting. *Chem. Soc. Rev.* **2009**, *38*, 253–278.

(33) Kawai, T.; Sakata, T. Photocatalytic Hydrogen Production from Liquid Methanol and Water. *J. Chem. Soc., Chem. Commun.* **1980**.

(34) Patsoura, A.; Kondarides, D. I.; Verykios, X. E. Photocatalytic Degradation of Organic Pollutants with Simultaneous Production of Hydrogen. *Catal. Today* **2007**, *124*, 94–102.

(35) Sivasamy, A.; Cheah, K. Y.; Fornasiero, P.; Kemausuor, F.; Zinoviev, S.; Miertus, S. Catalytic Applications in the Production of Biodiesel from Vegetable Oils.

ChemSusChem **2009**, *2*, 278–300.

(36) Aresta, M.; Dibenedetto, A.; Nocito, F.; Ferragina, C. Valorization of Bio-Glycerol : New Catalytic Materials for the Synthesis of Glycerol Carbonate via Glycerolysis of Urea. *J. Catal.* **2009**, *268*, 106–114.

(37) Behr, A.; Eilting, J.; Irawadi, K.; Leschinski, J.; Lindner, F. Improved Utilisation of Renewable Resources: New Important Derivatives of Glycerol. *Green Chem.* **2008**, *10*, 13–30.

(38) Kondaride, D. I.; Daskalaki, V. M.; Patsoura, A.; Verykios, X. E. Hydrogen Production by Photo-Induced Reforming of Biomass Components and Derivatives at Ambient Conditions. *Catal. Lett.* **2008**, *122*, 26–32.

(39) Montini, T.; Gombac, V.; Sordelli, L.; Delgado, J. J.; Chen, X.; Adami, G.; Fornasiero, P. Nanostructured Cu/TiO_2 Photocatalysts for H_2 Production from Ethanol and Glycerol Aqueous Solutions . *ChemCatChem* **2011**, *3*, 574–577.

(40) Beltram, A.; Romero Ocana, I.; Delgado Jaen, J. J.; Montini, T.; Fornasiero, P. Photocatalytic Valorization of Ethanol and Glycerol over TiO_2 Polymorphs for Sustainable Hydrogen Production. *Appl. Catal. A Gen.* **2016**, *518*, 167–175.

(41) Cargnello, M.; Gasparotto, A.; Gombac, V.; Montini, T.; Barreca, D.; Fornasiero, P. Photocatalytic H_2 and Added-Value By-Products - The Role of Metal Oxide Systems in Their Synthesis from Oxygenates. *Eur. J. Inorg. Chem.* **2011**, 4309–4323.

(42) Asahi, R.; Morikawa, T.; Ohwaki, T.; Aoki, K.; Taga, Y. Visible-Light Photocatalysis in Nitrogen-Doped Titanium Oxides. *Science,* **2001**, *293*, 269–271.

(43) Batzill, M.; Morales, E. H.; Diebold, U. Influence of Nitrogen Doping on the Defect Formation and Surface Properties of TiO_2 Rutile and Anatase. *Phys. Rev. Lett.* **2006**, *96*, 26103.

(44) Chen, X.; Mao, S. S. Titanium Dioxide Nanomaterials: Synthesis, Properties, Modifications, and Applications. *Chem. Rev.* **2007**, *107*, 2891−2959.

(45) In, S.; Orlov, A.; Berg, R.; Garcıa, F.; Pedrosa-jimenez, S.; Tikhov, M. S.; Wright, D. S.; Lambert, R. M. Effective Visible Light-Activated B-Doped and B, N-Codoped TiO_2 Photocatalysts. *J. Am. Chem. Soc.* **2007**, *129*, 13790–13791.

(46) Valentin, C. Di; Pacchioni, G. Trends in Non-Metal Doping of Anatase TiO_2: B, C, N and F. *Catal. Today* **2013**, *206*, 12–18.

(47) Primo, A.; Corma, A.; Garcia, H. Titania Supported Gold Nanoparticles as Photocatalyst Particles Supported in Porous. *Phys. Chem. Chem. Phys.* **2011**, *13*, 886–910.

(48) Montini, T.; Gombac, V.; Sordelli, L.; Delgado, J. J.; Chen, X.; Adami, G.; Fornasiero, P. Nanostructured Cu/TiO_2 Photocatalysts for H_2 Production from Ethanol and Glycerol Aqueous Solutions. *ChemCatChem* **2011**, *3*, 574–577.

(49) Korzhak, A. V; Ermokhina, N. I.; Stroyuk, A. L.; Bukhtiyarov, V. K.; Raevskaya, A. E.; Litvin, V. I.; Kuchmiy, S. Y.; Ilyin, V. G.; Manorik, P. A. Photocatalytic Hydrogen Evolution over Mesoporous TiO_2/metal Nanocomposites. *J. Photochem. Photobiol. A Chem.* **2008**, *198*, 126–134.

(50) Gallo, A.; Montini, T.; Marelli, M.; Minguzzi, A.; Gombac, V.; Psaro, R.; Fornasiero, P.; Dal Santo, V. H_2 Production by Renewables Photoreforming on Pt-Au/TiO_2 Catalysts Activated by Reduction. *ChemSusChem* **2012**, *5*, 1800–1811.

(51) Bowker, M.; Morton, C.; Kennedy, J.; Bahruji, H.; Greves, J.; Jones, W.; Davies, P. R.; Brookes, C.; Wells, P. P.; Dimitratos, N. Hydrogen Production by Photoreforming of Biofuels Using Au , Pd and Au – Pd/TiO_2 Photocatalysts. *J. Catal.* **2014**, *310*, 10–15.

(52) Taylor, S.; Mehta, M.; Samokhvalov, A. Production of Hydrogen by Glycerol Photoreforming Using Binary Nitrogen – Metal-Promoted N-M-TiO_2 Photocatalysts. *ChemPhysChem* **2014**, *15*, 942–949.

(53) Wang, F.; Jiang, Y.; Gautam, A.; Li, Y.; Amal, R. Exploring the Origin of Enhanced Activity and Reaction Pathway for Photocatalytic H_2 Production on Au/B-TiO_2 Catalysts. *ACS Catal.* **2014**, *4*, 1451–1457.

(54) Xing, M.; Fang, W.; Nasir, M.; Ma, Y.; Zhang, J.; Anpo, M. Self-Doped Ti_3^+ - Enhanced TiO_2 Nanoparticles with a High-Performance Photocatalysis. *J. Catal.* **2013**, *297*, 236–243.

(55) Chen, X.; Liu, L.; Yu, P. Y.; Mao, S. S. Increasing Solar Absorption for Photocatalysis with Black Hydrogenated Titanium Dioxide Nanocrystals. *Science* **2009**, *331*, 746–750.

(56) Valentin, C. Di; Pacchioni, G.; Selloni, A. Reduced and N-Type Doped TiO_2: Nature of Ti_3^+ species. *J. Phys. Chem. C* **2009**, *113*, 20543–20552.

(57) Chen, X.; Liu, L.; Liu, Z.; Marcus, M. A.; Wang, W.; Oyler, N. A.; Grass, M. E.; Mao, B.; Glans, P.; Yu, P. Y.; *et al.* Properties of Disorder-Engineered Black Titanium Dioxide Nanoparticles through Hydrogenation. *Sci. Rep.* **2013**, *3*, 1510.

(58) Eder, D. Carbon Nanotube - Inorganic Hybrids. *Chem. Rev.* **2010**, *110*, 1348–1385.

(59) Rhodes, C.; Hutchings, G. J.; Ward, A. M. Water-Gas Shift Reaction: Finding the Mechanistic Boundary. **1995**, *23*, 43–58.

(60) Newsome, D. S. The Water-Gas Shift Reaction. *Catal. Rev. Sci. Eng.* **1980**, *21*, 275–318.

(61) Ovesen, C. V; Clausen, B. S.; Hammershøi, B. S.; Steffensen, G.; Askgaard, T.; Chorkendorff, I.; Nørskov, J. K.; Rasmussen, P. B.; Stoltze, P.; Taylor, P. A Microkinetic Analysis of the Water – Gas Shift Reaction under Industrial Conditions. *J. Catal.* **1996**, *158*, 170–180.

(62) Gorte, R. J.; Zhao, S. Studies of the Water-Gas-Shift Reaction with Ceria-Supported Precious Metals. *Catal. Today* **2005**, *104*, 18–24.

(63) Hilaire, S.; Wang, X.; Luo, T.; Gorte, R. J.; Wagner, J. A Comparative Study of Water-Gas-Shift Reaction over Ceria Supported Metallic Catalysts. *Appl. Catal. A Gen.* **2001**, *215*, 271–278.

(64) Zalc, J. M.; Sokolovskii, V.; Loffle, D. G. Are Noble Metal-Based Water – Gas Shift Catalysts Practical for Automotive Fuel Processing? *J. Catal.* **2002**, *206*, 169–171.

(65) Fu, Q.; Saltsburg, H.; Flytzani-stephanopoulos, M. Active Nonmetallic Au and Pt Species on Ceria-Based Water-Gas Shift Catalysts. *Science,* **2003**, *301*, 935–038.

(66) Bunluesin, T.; Gorte, R. J.; Graham, G. W. Studies of the Water-Gas-Shift Reaction on Ceria-Supported Pt, Pd, and Rh: Implications for Oxygen-Storage Properties. *Appl. Catal. B Environ.* **1998**, *15*, 107–114.

(67) Montini, T.; Melchionna, M.; Monai, M.; Fornasiero, P. Fundamentals and Catalytic Applications of CeO_2-Based Materials. *Chem. Rev.* **2016**, *116*, 5987–6041.

(68) Wang, X.; Gorte, R. J.; Wagner, J. P. Deactivation Mechanisms for Pd/Ceria during the Water–Gas-Shift Reaction. *J. Catal.* **2002**, *212*, 225–230.

(69) Alivisatos, A. P. Perspectives on the Physical Chemistry of Semiconductor Nanocrystals. *J. Phys. Chem.* **1996**, *100*, 13226–13239.

(70) Melchionna, M.; Bonchio, M.; Paolucci, F.; Prato, M.; Fornasiero, P. Catalysis-Material Crosstalk at Tailored Nano-Carbon Interfaces. *Top Curr Chem* **2013**.

(71) Melchionna, M.; Marchesan, S.; Prato, M.; Fornasiero, P. Carbon Nanotubes and Catalysis: The Many Facets of a Successful Marriage. *Catal. Sci. Thechnology* **2015**, *5*, 3859–3875.

(72) Woan, K.; Pyrgiotakis, G.; Sigmund, W. Photocatalytic Carbon-Nanotube – TiO_2 Composites. *Adv. Mater.* **2009**, *21*, 2233–2239.

(73) Yu, Y.; Yu, J. C.; Yu, J.; Kwok, Y.; Che, Y.; Zhao, J.; Ding, L.; Ge, W.; Wong, P. Enhancement of Photocatalytic Activity of Mesoporous TiO_2 by Using Carbon Nanotubes. *Appl. Catal. A Gen.* **2005**, *289*, 186–196.

(74) Wang, W.; Serp, P.; Kalck, P.; Lu, J. Visible Light Photodegradation of Phenol on MWNT-TiO_2 Composite Catalysts Prepared by a Modified Sol – Gel Method. *J. Mater. Chem. A* **2005**, *235*, 194–199.

(75) Zhang, W.; Xu, B.; Jiang, L. Functional Hybrid Materials Based on Carbon Nanotubes and Metal Oxides. *J. Mater. Chem.* **2010**, *20*, 6383–6391.

(76) Sakthivel, S.; Kisch, H. Daylight Photocatalysis by Carbon-Modified Titanium Dioxide. *Angew. Chemie (International ed)* **2003**, *42*, 4908–4911.

(77) Chen, L.; Ho, Y.; Guo, W.; Huang, C.; Pan, T. Enhanced Visible Light-Induced Photoelectrocatalytic Degradation of Phenol by Carbon Nanotube-Doped TiO_2 Electrodes. *Electrochim. Acta* **2009**, *54*, 3884–3891.

(78) Shenderova, O. A.; Lawson, B. L.; Arenshkin, D.; Brenner, D. W. Predicted Structure and Electronic Properties of Individual Carbon Nanocones and Nanostructures Assembled from Nanocones. *Nanotechnology* **2001**, *12*, 191–197.

(79) Charlier, J.-C.; Rignanese, G. M. Electronic Structure of Carbon Nanocones. *Phys. Rev. Lett.* **2001**, *86*, 5970–5973.

(80) Oberlin, A.; Endo, M.; Koyama, T. FILAMENTOUS GROWTH OF CARBON

THROUGH BENZENE DECOMPOSITION. *J. Cryst. Growth* **1976**, *32*, 335–349.

(81) IIjima, S. Helical Microtubules of Graphitic Carbon. *Nature* **1991**, *354*, 56–58.

(82) Hamada, N.; Sawada, S.; Oshiyama, A. New One-Dimensional Conductors: Graphitic Microtubules. *Phys. Rev. Lett.* **1992**, *68*, 1579–1581.

(83) Mintmire, J. W.; Dunlap, B. I.; White, C. T. Are Fullereue Tubules Metallic? *Phys. Rev. Lett.* **1992**, *68*, 631–634.

(84) Fuhrer, M. S.; Adam, S. Carbon Conductor Corrupted. *Nature* **2009**, *458*, 38–39.

(85) Krishnan, A.; Dujardin, E.; Treacy, M. M.; Hugdahl, J.; Lynum, S.; Ebbesen, T. W. Graphitic Cones and the Nucleation of Curved Carbon Surfaces. *Nature* **1997**, *388*, 451–454.

(86) Naess, S. N.; Elgsaeter, A.; Helgesen, G.; Knudsen, K. D. Carbon Nanocones : Wall Structure and Morphology. *Sci. Technol. Adv. Mater.* **2009**, *10*, 65002.

(87) Lin, C.; Lee, C.; Chiu, H.; Chin, T. Graphene Structure in Carbon Nanocones and Nanodiscs. *Langmuir* **2007**, *23*, 12806–12810.

(88) Shalabi, A. S.; Soliman, K. A.; Taha, H. O. A Comparative Theoretical Study of Metal Functionalized Carbon Nanocones and Carbon Nanocone Sheets as Potential Hydrogen Storage Materials. *Phys. Chem. Chem. Phys.* **2014**, *16*, 19333–19339.

(89) *Thomas, J. M. and Thomas W. J. Principle and Practice of Heterogeneous Catalysis; VCH Publisher: Weinheim (Germany)*; 1997.

(90) Browne, W. R.; McGarvey, J. J. The Raman Effect and Its Application to Electronic Spectroscopies in Metal-Centered Species: Techniques and Investigations in Ground and Excited States. *Coord. Chem. Rev.* **2007**, *251*, 454–473.

(91) Saghi, Z.; Midgley, P. A. Electron Tomography in the (S)TEM: From Nanoscale Morphological Analysis to 3D Atomic Imaging. *Annu. Rev. Mater. Res.* **2012**, *42*, 59–79.

(92) *Goodhew, P. J.; Humphreys, J.; Beanland, R. Electron Microscopy and Analysis; Taylor & Francis*; 2001.

(93) Yang, J. C.; Small, M. W.; Grieshaber, V.; Nuzzo, R. G. Recent Developments and Applications of Electron Microscopy to Heterogeneous Catalysis. *Chem. Soc. Rev.* **2012**, *41*, 8179–8194.

(94) Sing, K. S. W.; Everett, D. H.; Haul, R. A. W.; Moscou, L.; Pierotti, R. A.; Rouquerol, J.; Siemieniewska, T. Reporting Physisorption Data for Gas/solid Systems with Special Reference to the Determination of Surface Area and Porosity. *Pure Appl. Chem.* **1985**, *57*, 603–619.

(95) Rouquerol, J.; Avnir, D.; Fairbrige, C. W.; Everett, D. H.; Haynes, J. H.; Pernicone, N.; Ramsay, J. D.; Sing, K. S. W.; Unger, K. K. RECOMMENDATIONS FOR THE CHARACTERIZATION OF POROUS SOLIDS. *Pure Appl. Chem.* **1994**, *66*, 1739–1758.

(96) Barrett, E.; Joyner, L.; Halenda, P. The Determination of Pore Volume and Area Distributions in Porous Substances. I. Computations from Nitrogen Isotherms. *J. Am. Chem. Soc.* **1951**, *73*, 373–380.

(97) Lippens, B. C. Studies on Pore Systems in Catalysts: V. The T Method. *J. Catal.* **1965**, *4*, 319–323.

(98) Dulaurent, O.; Bianchi, D. Adsorption Isobars for CO on a Pt/Al_2O_3 Catalyst at High Temperatures Using FTIR Spectroscopy : Isosteric Heat of Adsorption and Adsorption Model. *Appl. Catal. A Gen.* **2000**, *196*, 271–280.

(99) Gatica, J. M.; Baker, R. T.; Fornasiero, P.; Bernal, S.; Kaspar, J. Characterization of the Metal Phase in $NM/Ce_{0.68}Zr_{0.32}O_2$ (NM: Pt and Pd) Catalysts by Hydrogen Chemisorption and HRTEM Microscopy : A Comparative Study. *J. Phys. Chem. B* **2001**, *105*, 1191–1199.

(100) Zhang, J.; Wnag, Z.; Wnag, Z. X. Adsorption of Carbon Monoxide on Pd Low-Index Surfaces and (110) Reconstructed Surface. *Surf. Interface Anal.* **2011**, *43*, 1038–1045.

(101) Carbajal Ramos, I. A.; Montini, T.; Lorenzut, B.; Troiani, H.; Gennari, F. C.; Graziani, M.; Fornasiero, P. Hydrogen Production from Ethanol Steam Reforming on $M/CeO_2/YSZ$ (M = Ru, Pd, Ag) Nanocomposites. *Catal. Today* **2012**, *180*, 96–104.

(102) Anderson, J. R. S. *Structure of Metallic Catalysts; Academic Press: London*; 1975.

(103) Ratnasamy, C.; Wagner, J. P. Water Gas Shift Catalysis. *Catal. Rev.* **2009**, *51*, 325–440.

(104) Shido, T.; Iwasawa, Y. Reactant-Promoted Reaction Mechanism for Water-Gas Shift Reaction on Rh-Doped CeO_2. *J. Catal. Cat* **1993**, *141*, 71–81.

(105) Jacobs, G.; Williams, L.; Graham, U.; Thomas, G. A.; Sparks, D. E.; Davis, B. H. Low Temperature Water – Gas Shift : In Situ DRIFTS-Reaction Study of Ceria Surface Area on the Evolution of Formates on Pt/CeO_2 Fuel Processing Catalysts for Fuel Cell Applications. *Appl. Catal. A Gen.* **2003**, *252*, 107–118.

(106) Li, Y.; Fu, Q.; Flytzani-stephanopoulos, M. Low-Temperature Water-Gas Shift Reaction over Cu- and Ni-Loaded Cerium Oxide Catalysts. *Appl. Catal. B Environ.* **2000**, *27*, 179–191.

(107) Zafiris, G. S.; Gorte, R. J. Evidence for Low-Temperature Oxygen Migration from Ceria to Rh. *J. Catal.* **1993**, *139*, 561–567.

(108) Sharma, S.; Hilaire, S.; Vohs, J. M.; Gorte, R. J.; Jen, H. Evidence for Oxidation of Ceria by CO_2. *J. Catal.* **2000**, *190*, 199–204.

(109) Meunier, F. C.; Goguet, A.; Hardacre, C.; Burch, R.; Thompsett, D. Quantitative DRIFTS Investigation of Possible Reaction Mechanisms for the Water–Gas Shift Reaction on High-Activity Pt- and Au-Based Catalysts. *J. Catal.* **2007**, *252*, 18–22.

(110) Meunier, F. C.; Reid, D.; Goguet, A.; Shekhtman, S.; Hardacre, C.; Burch, R.; Deng, W. Quantitative Analysis of the Reactivity of Formate Species Seen by DRIFTS over a $Au/Ce(La)O_2$ Water – Gas Shift Catalyst : First Unambiguous Evidence of the Minority Role of Formates as Reaction Intermediates. *J. Catal.* **2007**, *247*, 277–287.

(111) Bernal, S.; Calvino, J. J.; Cauqui, M. A.; Gatica, J. M.; Larese, C.; Perez Omil, Â.; Pintado, J. M. Some Recent Results on Metal/support Interaction Effects in NM/CeO_2 (NM: Noble Metal) Catalysts. *Catal. Today* **1999**, *50*, 175–206.

(112) Sa, J.; Bernardi, J.; Anderson, J. A. Imaging of Low Temperature Induced SMSI on Pd/TiO_2 Catalysts. *Catal. Letters* **2007**, *114*, 91–95.

(113) Feio, L. S. F.; Hori, C. E.; Damyanova, S.; Noronha, F. B.; Cassinelli, W. H.; Marques, C. M. P.; Bueno, J. M. C. The Effect of Ceria Content on the Properties

of $Pd/CeO_2/Al_2O_3$ Catalysts for Steam Reforming of Methane. *Appl. Catal. A Gen.* **2007**, *316*, 107–116.

(114) Tauster, S. J.; Fung, S. C.; Baker, R. T. K.; Horsley, J. A. Strong Interactions in Supported-Metal Catalysts. *Science* **2016**, *211*, 1121–1125.

(115) Roberts, S.; Gorte, R. J. A Study of the Migration and Stability of Titania on a Model Rh Catalyst. *J. Catal.* **1990**, *124*, 553–556.

(116) Sun, H. P.; Pan, X. P.; Graham, G. W.; Jen, H.; Mccabe, R. W.; Thevuthasan, S.; Peden, C. H. F. Partial Encapsulation of Pd Particles by Reduced Ceria-Zirconia. *Appl. Phys. lLtters* **2005**, *87*, 201915-.

(117) Wieder, N. L.; Cargnello, M.; Bakhmutsky, K.; Montini, T.; Fornasiero, P.; Gorte, R. J. Study of the Water-Gas-Shift Reaction on $Pd@CeO_2/Al_2O_3$ Core - Shell Catalysts. *J. Phys. Chem. C* **2011**, *115*, 915–919.

(118) Cargnello, M.; Grzelczak, M.; Rodr, B.; Syrgiannis, Z.; Bakhmutsky, K.; Parola, V. La; Liz-Marzan, L. M.; Gorte, R. J.; Prato, M.; Fornasiero, P. Multiwalled Carbon Nanotubes Drive the Activity of Metal@oxide Core−Shell Catalysts in Modular Nanocomposites. *J. Am. Chem. Soc.* **2012**, *134*, 11760–11766.

(119) Bahr, J. L.; Tour, J. M. Using in Situ Generated Diazonium Compounds. **2001**, *13*, 3823–3824.

(120) Dyke, C. A.; Tour, J. M. Covalent Functionalization of Single-Walled Carbon Nanotubes for Materials Applications. **2004**, *108*, 11151–11159.

(121) Price, B. K.; Tour, J. M. Functionalization of Single-Walled Carbon Nanotubes "On Water". *J. Am. Chem. Soc.* **2006**, *128*, 12899–12904.

(122) Salice, P.; Fabris, E.; Sartorio, C.; Fenaroli, D.; Figà, V.; Casaletto, M. P.; Cataldo, S.; Pignataro, B.; Menna, E. An Insight into the Functionalisation of Carbon Nanotubes by Diazonium Chemistry : Towards a Controlled Decoration. *Carbon N. Y.* **2014**, *74*, 73–82.

(123) Cargnello, M.; Wieder, N. L.; Montini, T.; Gorte, R. J.; Fornasiero, P. Synthesis of Dispersible $Pd@CeO_2$ Core - Shell Nanostructures by Self-Assembly. *J. Am. Ceram. Soc.* **2010**, *132*, 1402–1409.

(124) Cargnello, M.; Wieder, N. L.; Canton, P.; Montini, T.; Giambastiani, G.; Benedetti,

A.; Gorte, R. J.; Fornasiero, P. A Versatile Approach to the Synthesis of Functionalized Thiol-Protected Palladium Nanoparticles. *Chem. Mater.* **2011**, *23*, 3961–3969.

(125) Bom, D.; Andrews, R.; Jacques, D.; Anthony, J.; Chen, B.; Meier, M. S.; Selegue, J. P. Thermogravimetric Analysis of the Oxidation of Multiwalled Carbon Nanotubes: Evidence for the Role of Defect Sites in Carbon Nanotube Chemistry. *Nano Lett.* **2002**, *2*, 615–619.

(126) Maultzsch, J.; Reich, S.; Thomsen, C.; Webster, S.; Czerw, R.; Al., E. Raman Characterization of Boron-Doped Multiwalled Carbon Nanotubes. *Appl. Phys. Lett.* **2002**, *81*, 2647–2649.

(127) Ran, M.; Sun, W.; Liu, Y.; Chu, W.; Jiang, C. Functionalization of Multi-Walled Carbon Nanotubes Using Water-Assisted Chemical Vapor Deposition. *J. Solid State Chem.* **2013**, *197*, 517–522.

(128) Datsyuk, V.; Kalyva, M.; Papagelis, K.; Parthenios, J.; Tasis, D.; Siokou, A.; Kallitsis, I.; Galiotis, C. Chemical Oxidation of Multiwalled Carbon Nanotubes. *Carbon N. Y.* **2008**, *46*, 833–840.

(129) Müller, M.; Maultzsch, J.; Wunderlich, D.; Hirsch, A.; Thomsen, C. Raman Spectroscopy on Chemically Functionalized Carbon Nanotubes. *Phys. Status Solidi* **2007**, *244*, 4056–4059.

(130) Inoue, F.; Ando, A.; Corio, P.; Wiley, J. Raman Evidence of the Interaction between Multiwalled Carbon Nanotubes and Nanostructured TiO_2. *Raman Spectrosc.* **2011**, *42*, 1379–1383.

(131) Spanier, J. E.; Robinson, R. D.; Zhang, F.; Chan, S.; Herman, I. P. Size-Dependent Properties of CeO_{2-Y} Nanoparticles as Studied by Raman Scattering. *Phys. Rev. B* **2001**, *64*, 245407.

(132) Weber, W. H.; Hass, K. C.; McBride, J. R. Raman Study of CeO_2: Second-Order Scattering, Lattice, Dynamics and Particle-Size Effects. *Phys. Rev. B* **1993**, *48*, 178–185.

(133) Endo, M.; Takeuchi, K.; Hiroaka, T.; Furuta, T.; Kasai, T.; Sun, X.; Kiang, C.-H.; Dresselhaus, M. S. Stacking Nature of Graphene Layers in Carbon Nanotubes and Nanofibres. *J. Phys. Chem. Solids* **1997**, *58*, 1707–1712.

(134) Bradley, R. H.; Cassity, K.; Andrews, R.; Meier, M.; Osbeck, S.; Andreu, A.; Johnston, C.; Crossley, A. Surface Studies of Hydroxylated Multi-Wall Carbon Nanotubes. *Appl. Surf. Sci.* **2012**, *258*, 4835–4843.

(135) Melchionna, M.; Prato, M. Functionalizing Carbon Nanotubes: An Indispensible Step towards Applications. *ECS J. Solid State Sci. Technol.* **2013**, *2*, M3040–M3045.

(136) Cargnello, M.; Delgado Jaén, J. J.; Hernández Garrido, J. C.; Bakhmutsky, K.; Montini, T.; Calvino Gámez, J. J.; Gorte, R. J.; Fornasiero, P. Exceptional Activity for Methane Combustion over Modular Pd@CeO_2 Subunits on Functionalized Al2O3. *Science* **2012**, *337*, 713–717.

(137) Monai, M.; Montini, T.; Chen, C.; Fonda, E.; Gorte, R. J.; Fornasiero, P. Methane Catalytic Combustion over Hierarchical Pd@CeO_2/Si-Al_2O_3: Effect of the Presence of Water. *ChemCatChem* **2014**, *7*, 2038–2046.

(138) Puga, A. V. Photocatalytic Production of Hydrogen from Biomass-Derived Feedstocks. *Coord. Chem. Rev.* **2016**, *315*, 1–66.

(139) Bahnemann, D. W.; Hilgendorff, M.; Memming, R. Charge Carrier Dynamics at TiO_2 Particles : Reactivity of Free and Trapped Holes. *J. Phys. Chem. B* **1997**, *101*, 4265–4275.

(140) Fujishima, A.; Rao, T. N.; Tryk, D. A. Titanium Dioxide Photocatalysis. *J. Photochem. Photobiol. C Photochem. Rev.* **2000**, *1*, 1–21.

(141) Bowker, M.; Davies, P. R.; Al-mazroai, L. S. Photocatalytic Reforming of Glycerol over Gold and Palladium as an Alternative Fuel Source. *Catal. Lett.* **2009**, *128*, 253–255.

(142) Bahruji, H.; Bowker, M.; Davies, P. R.; Al-mazroai, L. S.; Dickinson, A.; Greaves, J.; James, D.; Millard, L.; Pedrono, F. Sustainable H_2 Gas Production by Photocatalysis. *J. Photochem. Photobiol. A Chem.* **2010**, *216*, 115–118.

(143) Kesselman, J. M.; Weres, O.; Lewis, N. S.; Hoffmann, M. R. Electrochemical Production of Hydroxyl Radical at Polycrystalline Nb-Doped TiO_2 Electrodes and Estimation of the Partitioning between Hydroxyl Radical and Direct Hole Oxidation Pathways. *J. Phys. Chem. B* **1997**, *101*, 2637–2643.

(144) Yang, Y. Z.; Chang, C.-H.; Idriss, H. Photo-Catalytic Production of Hydrogen

Form Ethanol over M/TiO_2 Catalysts (M= Pd, Pt or Rh). *Appl. Catal. B Environ.* **2006**, *67*, 217–222.

(145) Mattsson, A.; Osterlund, L. Adsorption and Photoinduced Decomposition of Acetone and Acetic Acid on Anatase, Brookite, and Rutile TiO_2 Nanoparticles. *J. Phys. Chem. C* **2010**, *114*, 14121–14132.

(146) Millard, L.; Bowker, M. Photocatalytic Water-Gas Shift Reaction at Ambient Temperature. *J. Photochem. Photobiol. A Chem.* **2002**, *148*, 91–95.

(147) Ohsaka, T.; Izumi, F.; Fujiki, Y. Raman Spectrum of Anatase, TiO_2. *J. Raman Spectrosc.* **1978**, *7*, 321–324.

(148) Frank, O.; Zukalova, M.; Laskova, B.; Kurti, J.; Koltai, J.; Kavan, L. Raman Spectra of Titanium Dioxide (Anatase, Rutile) with Identified Oxygen Isotopes (16, 17, 18). *Phys. Chem. Chem. Phys.* **2012**, *14*, 14567–14572.

(149) Li, Y.; Xu, B.; Fan, Y.; Feng, N.; Qiu, A.; He, J. M. J.; Yang, H.; Chen, Y. The Effect of Titania Polymorph on the Strong Metal-Support Interaction of Pd/TiO_2 Catalysts and Their Application in the Liquid Phase Selective Hydrogenation of Long Chain Alkadienes. *J. Mol. Catal. A Chem* **2004**, *216*, 107–114.

(150) Kang, J. H.; Shin, E. W.; Kim, W. J.; Park, J. D.; Moon, S. H. Selective Hydrogenation of Acetylene on TiO_2-Added Pd Catalysts. *J. Catal.* **2002**, *208*, 310–320.

(151) Gatica, J. M.; Baker, R. T.; Fornasiero, P.; Bernal, S.; Blanco, G.; Kaspar, J. Rhodium Dispersion in a Rh/$Ce_{0.68}Zr_{0.32}O_2$ Catalyst Investigated by HRTEM and H_2 Chemisorption. *J. Phys. Chem. B* **2000**, *104*, 4667–4672.

(152) Boudart, M.; Hwang, H. S. Solubility of Hydrogen in Small Particles of Palladium. *J. Catal.* **1975**, *39*, 44–52.

(153) Yu, H.; Quan, X.; Chen, S.; Zhao, H. TiO_2-Multiwalled Carbon Nanotube Heterojunction Arrays and Their Charge Separation Capability. *J. Phys. Chem. C* **2007**, *111*, 12987–12991.

(154) Ampelli, C.; Passalacqua, R.; Genovese, C.; Perathoner, S.; Centi, G.; Montini, T.; Gombac, V.; Delgado Jaén, J. J.; Fornasiero, P. H_2 Production by Selective Photo-Dehydrogenation of Ethanol in Gas and Liquid Phase on CuO_x/TiO_2 Nanocomposites. *RSC Adv.* **2013**, *3*, 21776–21788.

(155) Chiarello, G. L.; Aguirre, M. H.; Selli, E. Hydrogen Production by Photocatalytic Steam Reforming of Methanol on Noble Metal-Modified TiO_2. *J. Catal.* **2010**, *273*, 182–190.

(156) Li, Q.; Guo, B.; Yu, J.; Ran, J.; Zhang, B.; Yan, H.; Gong, J. R. Highly Efficient Visible-Light-Driven Photocatalytic Hydrogen Production of CdS-Cluster-Decorated Graphene Nanosheets. *J. Am. Chem. Soc.* **2011**, *113*, 10878–10884.

(157) Moya, A.; Cherevan, A.; Marchesan, S.; Gebhardt, P.; Prato, M.; Eder, D.; Vilatela, J. J. Oxygen Vacancies and Interfaces Enhancing Photocatalytic Hydrogen Production in Mesoporous CNT/TiO_2 Hybrids. *Appl. Catal. B Environ.* **2015**, *179*, 574–582.

(158) Melchionna, M.; Beltram, A.; Montini, T.; Monai, M.; Nasi, L.; Fornasiero, P.; Prato, M. Highly Efficient Hydrogen Production through Ethanol Photoreforming by a Carbon Nanocone /. *Chem. Commun.* **2015**, *52*, 764–767.

(159) Chevran, A. S.; Gebhardt, P.; Shearer, C. J.; Matsukawa, M.; Domen, K.; Eder, D. Interface Engineering In Nanocarbon-Ta_2O_5 Hybrid Photocatalysts. *Energy Environ. Sci.* **2014**, *7*, 791.

(160) Beltram, A.; Melchionna, M.; Montini, T.; Nasi, L.; Fornasiero, P.; Prato, M. Making H_2 from Light and Biomass-Derived Alcohols: The Outstanding Activity of Newly Designed Hierarchical MWCNTs/Pd@TiO_2 Hybrid Catalysts. *Green Chem.* **2017**, *accepted*, DOI: 10.1039/C6GC01979J.

(161) Lv, X.-J.; Zhou, S.-X.; Chang, H.-X.; Chen, H.-X.; Fu, W.-F. Synergetic Effect of Cu and Graphene as Cocatalyst on TiO_2 for Enhanced Photocatalytic Hydrogen Evolution from Solar Water Splitting. *J. Mater. Chem.* **2012**, *22*, 18542–18549.

(162) Chen, D.; Zou, L.; Li, S.; Zheng, F. Nanospherical like Reduced Graphene Oxide Decorated TiO_2 Nanoparticles : An Advanced Catalyst for the Hydrogen Evolution Reaction. *Sci. Rep.* **2016**, *6*, 20335.

(163) Dai, K.; Peng, T.; Ke, D.; Wei, B. Photocatalytic Hydrogen Generation Using a Nanocomposite of Multi-Walled Carbon Nanotubes and TiO_2 Nanoparticles under Visible Light Irradiation. *Nanotechnology* **2009**, *20*, 125603.

(164) Chai, B.; Peng, T.; Zhang, X.; Mao, J.; Li, K.; Zhang, X. Synthesis of C_{60}-Decorated SWCNTs (C_{60}-D-CNTs) and Its TiO_2-Based Nanocomposite with

Enhanced Photocatalytic Activity for Hydrogen Production. *Dalt. Trans.* **2013**, *42*, 3402–3409.

(165) Mukherji, A.; Serger, B.; Lu, G. Q. M.; Wamg, L. Nitrogen Doped $Sr_2Ta_2O_7$ Coupled with Graphene Sheets as Photocatalysts for Increased Photocatalytic Hydrogen Production. *ACS Nano* **2011**, *5*, 3483–3492.

(166) Mamathakumari, M.; Kumar, D. P.; Haridoss, P.; DurgaKumari, V.; Shankar, M. V. Nanohybrid of Titania/carbon Nanotubes E Nanohorns : A Promising Photocatalyst for Enhanced Hydrogen Production under Solar Irradiation. *Int. J. Hydrogen Energy* **2015**, *40*, 1665–1674.

(167) Ferrari, A. C.; Meyer, J. C.; Scardaci, V.; Casiraghi, C.; Lazzeri, M.; Mauri, F.; Piscanec, S.; Jiang, D.; Novoselov, K. S.; Roth, S.; Geim, A. K. Raman Spectrum of Graphene and Graphene Layers. *Phys. Rev. Lett.* **2006**, *97*, 187401.

RINGRAZIAMENTI

Ringrazio innanzitutto il Professor Paolo Fornasiero ed il Professor Maurizio Prato per avermi dato l'opportunità di svolgere questo progetto di tesi nei loro gruppi di ricerca. In particolar modo Paolo per aver creduto in me dopo la tesi magistrale dandomi la possibilità di iniziare un cammino nel mondo della ricerca.

Ringrazio inoltre tutti i membri di entrambi i gruppi di ricerca: Valentina Gombac, Matteo Monai, Kostas, Angela, Dani e Anna. Grazie a tutti voi per il sostegno, per le chiacchierate ma soprattutto per i bei momenti passati insieme.

Un ringraziamento particolare al Dr. Tiziano Montini e al Dr. Michele Melchionna per essermi stati affianco in questi tre anni supportandomi e sopportandomi, spronandomi a dare sempre il meglio e per la grande pazienza che hanno avuto durante la stesura della tesi.

Infine un ringraziamento speciale alla mia cara Lea….. per essermi stata sempre affianco.